



저작자표시-비영리-변경금지 2.0 대한민국

이용자는 아래의 조건을 따르는 경우에 한하여 자유롭게

- 이 저작물을 복제, 배포, 전송, 전시, 공연 및 방송할 수 있습니다.

다음과 같은 조건을 따라야 합니다:



저작자표시. 귀하는 원저작자를 표시하여야 합니다.



비영리. 귀하는 이 저작물을 영리 목적으로 이용할 수 없습니다.



변경금지. 귀하는 이 저작물을 개작, 변형 또는 가공할 수 없습니다.

- 귀하는, 이 저작물의 재이용이나 배포의 경우, 이 저작물에 적용된 이용허락조건을 명확하게 나타내어야 합니다.
- 저작권자로부터 별도의 허가를 받으면 이러한 조건들은 적용되지 않습니다.

저작권법에 따른 이용자의 권리는 위의 내용에 의하여 영향을 받지 않습니다.

이것은 [이용허락규약\(Legal Code\)](#)을 이해하기 쉽게 요약한 것입니다.

[Disclaimer](#)

Doctoral Thesis

Controllable Synthesis of Multifunctional, Two-
Dimensional Carbon Sheets at Low Temperatures

Jae Hwan Chu

Department of Materials Science and Engineering

Graduate School of UNIST

2016

Controllable Synthesis of Multifunctional, Two-Dimensional Carbon Sheets at Low Temperatures

Jae Hwan Chu

Department of Materials Science and Engineering

Graduate School of UNIST

Controllable Synthesis of Multifunctional, Two- Dimensional Carbon Sheets at Low Temperatures

A thesis/dissertation
submitted to the Graduate School of UNIST
in partial fulfillment of the
requirements for the degree of
Doctor of Philosophy

Jae Hwan Chu

1. 13. 2016 of submission

Approved by



Advisor

Soon-Yong Kwon

Controllable Synthesis of Multifunctional, Two-Dimensional Carbon Sheets at Low Temperatures

Jae Hwan Chu

This certifies that the thesis/dissertation of Jae Hwan Chu is
approved.

1. 13. 2016 Month/Day/Year of submission

signature



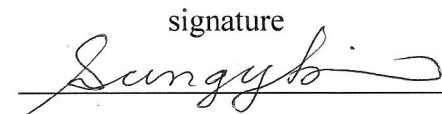
Advisor: Soon-Yong Kwon

signature



Kibog Park

signature



Sung Youb Kim

signature



Jung-Woo Yoo

signature



Sung Dae Kim

Abstract

Controllable Synthesis of Multifunctional, Two-Dimensional Carbon Sheets at Low Temperatures

Jae Hwan Chu

School of Materials Science and Engineering

Ulsan National Institute of Science and Technology (UNIST)

As an ultimate objective to apply for two-dimensional (2D) materials electronics, the 2D material, graphene synthesis has become an important challenge for large area and high-quality growth. Consequently, several approach to produce single and few-layer graphene or graphene oxide (GO) have been reported to date, such as chemical vapor deposition (CVD) method and chemically derived GO sheet by the modified hummer method etc. However, CVD method pay close attention to be taken to precisely control the resulting graphene layer owing to its sensitivity to various process parameters. Besides, it must accompany a transfer method from metal substrate used to grow graphene to desired substrate for applications. For meanwhile, GO sheets were not considered to use 2D electronics because chemically decorated oxygen groups with combination of sp^2 - and sp^3 - hybridized carbon sheets were attributed to electrically insulating and must be occupied to reduction process using chemical and/or thermal treatment to activate electrical well organized sp^2 -graphene structure.

This study intends to introduce controllable synthesis of multifunctional, 2D carbon sheet at low temperature. Our group demonstrated transfer-free, large-area growth of graphene films via Diffusion Assisted Synthesis (DAS) method at close to room temperature. In DAS method, it took notice of the mathematical analysis of the grain boundary diffusion process began with Fisher model. They studied that tracer atoms on the surface diffuse into a solid either by direct volume diffusion or by diffusion through the grain boundary followed by lateral volume diffusion from the boundary to the lattice. It turns out that lower temperatures greatly favor grain boundary diffusion relative to volume diffusion. For this reason, we suggested that carbon atoms for solid carbon-source can primarily diffuse Ni film through grain boundary diffusion relative to lattice diffusion at low temperature (25 ~ 160 °C) since previous experimental and theoretical studies indicated that Ni surface can catalyze the dissociation of C-C bonds and promote diffusion even at room temperature. Eventually, in the DAS method, in contrast to other approaches, our method demonstrated that diffusion of carbon atoms through a diffusion couple made up of carbon-nickel/substrate synthesized graphene film underneath the Ni film at the nickel-substrate interface. Moreover, large area of graphene film can be directly grown

at desired substrate without transfer process whatever it is inorganic (SiO_2/Si , Sapphire etc.), polymer (PMMA, PDMS), and glass substrate. Considering our approach, it could be applicable to graphene electronics.

As a modified DAS method using Cu foil, in this dissertation, we demonstrate that a monolithic graphene oxide (GO) sheets can be physically synthesized on a copper foil using solid carbon sources at low temperature ($\leq 260^\circ\text{C}$), with controllable oxygen to carbon (O/C) composition. Actually, modified DAS method initially expected that much larger grain size of grain boundary using foils can overcome limit of evaporated nickel film, where grain boundary engineering of foils is much easier than to films. Unexpectedly, in contrast to chemically synthesized GO sheets, an another types graphene film was synthesized with atomically decorated oxygen containing functional groups. For this reason, manufactured Cu foils with quite uniform oxygen distribution were clearly observed in grain boundary of Cu foil whatever before and after annealing process. As a result, the diffused carbon atoms through Cu foil can be combined with dissolved oxygen atom at the grain boundaries of Cu foil followed with the diffusion of C-O dimers over Cu as well as grain boundaries during DAS process and enabling the formation of monolithic GO sheets on reverse side of Cu foil. Similarly, our density functional theory (DFT) calculation results also demonstrate that the lowest energy barriers for the diffusion C- and O-adatoms were achieved when C-O dimers diffusion of over Cu, regardless of the orientation of the crystallographic plane (Cu (111), 0.105 eV, Cu (100), 0.188 eV). Moreover, physically synthesized GO sheets can be surprisingly tuned oxygen to carbon composition by modifying the residual oxygen concentration in Cu, which directly correlated with the heating profile of Cu foil during annealing step. Accordingly, the tunable resulting GO sheets have showed the most interesting feature of that modulating band gap energy, by varying the O/C composition. Therefore, in our approach, we have successfully demonstrated a new physical synthesis method for GO sheets and tunable O/C composition offers a more promising opportunity to the precision assembly of graphene-based electronics because of its property of the modulation of band gap.

Keywords: Two-Dimensional materials, Graphene, Graphene Oxide (GO), Diffusion-Assisted Synthesis (DAS) method, Tunable band gap and chemical composition.

Contents

Abstract	I
Contents	III
List of Figures	V
List of Tables	XI
Chapter 1. Introduction	1
1.1 History of Two-Dimensional (2D) Materials.....	2
1.2 Materials Overview.....	4
1.2.1 Graphene.....	4
1.2.2 Graphene Oxide (GO).....	7
1.2.3 Reduced Graphene Oxide (RGO).....	9
1.3 Synthesis of 2D Materials.....	10
1.3.1 Mechanical Exfoliation.....	10
1.3.2 Epitaxy Growth.....	10
1.3.3 Chemical Vapor Deposition.....	10
1.3.4 Rapid Thermal Annealing.....	11
1.3.5 Hummer Method.....	11
Chapter 2. Methodology Review	16
2.1 Low-Temperature Synthesis of Transfer-Free Graphene Films.....	16
2.1.1 Diffusion Assisted Synthesis (DAS) Method.....	16
2.1.2 Grain Boundary Theory.....	17
2.1.3 Fisher Model in DAS Process.....	19
2.1.4 Density Functional Theory (DFT) Calculation on Single Carbon Atom Diffusion.....	20

Chapter 3. Experimental Preparation	28
3.1 Materials Preparation.....	28
3.2 Experimental Procedure.....	29
3.3 Characterization.....	34
Chapter 4. Physically Synthesized GO Sheets	37
4.1 Introduction.....	37
4.2 Synthesis of Monolithic GO Sheet via DAS.....	38
4.3 Formation of a Graphene Framework on Cu Foil.....	41
4.4 Presence of Oxygen Groups on The Graphene Framework.....	42
4.5 Atomic Structure of The GO Sheets.....	48
Chapter 5. Growth Mechanism	50
5.1 Existence of Incubation Time in GO Synthesis.....	50
5.2 DFT Calculation of Transition State Energy of Carbon and Oxygen adatoms on Cu Foils.....	51
5.3 Mechanism for The Formation of GO Sheets.....	56
Chapter 6. Tunable Chemical Compositions and Electrical Properties	60
6.1 Control of O/C Composition and Tunable Bandgap Energy.....	60
6.2 Tunable Electrical Properties of The GO Sheets.....	64
Chapter 7. Conclusion	71
Reference	72
Curriculum Vitae	81

List of figures

Figure 1.1. Different allotropes of carbon.

Figure 1.2. (a) Crystal structure of graphene consisting of sublattice A (blue) and B (red). The lattice vectors a_1 and a_2 as well as The vectors δ_1 , δ_2 , and δ_3 connect carbon atoms separated by a distance $a = 0.142$ nm. (b) The first Brillouin zone. Γ is the center of the cell. K and K' are the corners of the first Brillouin zone (Dirac points), and M is the center of the edge.³⁵

Figure 1.3. Band structure of graphene and zoom of the dispersion relation close to the K-point for small energies.³⁵

Figure 1.4. Electric field effect of a graphene based device. (a) band structure of graphene. (b) Modulating Fermi energy level of graphene by using a gate field. The Minimum conduction point is observed when the Fermi level coincides with the Dirac point.³⁵

Figure 1.5. Proposed structure of GO sheet.³⁹

Figure 1.6. As-prepared graphite oxide dispersed in water and various organic solvents.⁴⁰

Figure 1.7. (a) Schematic illustration of disordered RGO basal plane consisting of holes, topological defects and remnants of oxygen groups.⁵⁴ (b) Atomic resolution, aberration-corrected high-resolution transmission electron micrograph of a single-layer RGO membrane⁵⁵.

Figure 1.8. (a) Schematic illustration of the exfoliation process. (b) Optical microscope images of graphene flakes (single-, bi- and tri- layer samples). (adapted from GLAB)

Figure 1.9. Schematic illustration of epitaxial graphene growth on a silicon carbide (SiC) substrate. (adapted from Bart J. van wees Lab)

Figure 1.10. Schematic illustration of growth kinetics in CVD graphene on different catalyst on Ni (right) and Cu (left) substrate.

Figure 1.11. Schematic illustration for nickel-assisted facile synthesis method of few-layer graphene by RTA method⁵⁶.

Figure 2.1. The schematic diagram of graphene growth mechanism in DAS process represents the elementary steps of the process including dissociation of C-C bonds at C/Ni interface, diffusion of carbon atoms, followed by nucleation and growth of graphene. Graphene growth mechanism in case (a) $460\text{ }^{\circ}\text{C} \leq T \leq 600\text{ }^{\circ}\text{C}$; bulk diffusion through Ni crystallites, leading to homogeneous nucleation and multiple sites resulting in the formation of nanocrystalline graphene film by precipitation and (b) $T \leq 260\text{ }^{\circ}\text{C}$; preferential diffusion of C atoms via lateral diffusion of C atoms along Ni/substrate interface.⁶⁶

Figure 2.2. Large size grain of graphene grown at $T = 160\text{ }^{\circ}\text{C}$ on SiO_2 using dark-field TEM. a, Selective area diffraction pattern taken from graphene using 300 nm diameter aperture, showing a single hexagonal diffraction pattern. This reveals that the grain size is larger than 300 nm. Scale bar is 10 $1/\text{nm}$. b, a dark-field image obtained using a $g(1\bar{2}10)$ spot (blue circle in a) shows the real-space shape of these grains. c, Low magnification plan-view TEM image of nanocrystalline graphene films grown at $T \geq 460\text{ }^{\circ}\text{C}$ for 5min on SiO_2/Si substrates. d, selected area diffraction from red circle in c, which displays continuous ring patterns. The two diffraction rings correspond to graphene crystal plane $(0\bar{1}10)$ and $(1\bar{2}10)$. Scale bar is 5 $1/\text{nm}$.⁶⁶

Figure 2.3. Schematic geometry in the Fisher model of GB diffusion.⁶⁷

Figure 2.4. Schematic illustration of type A, B and C diffusion kinetics according to Harrison's classification.⁶⁹

Figure 3.1. Annealing of Cu foils. (a) The 1- μm -thick Cu foils immersed in acetic acid using a Teflon zig, (b) the Cu foils on a 2-inch SiO_2/Si substrate, (c) annealing process of Cu/ SiO_2/Si on a susceptor at about $790\text{ }^{\circ}\text{C}$ in an UHV chamber.

Figure 3.2. Schematic illustration of DAS process.⁶⁶

Figure 3.3. Preparation of C-Cu- SiO_2/Si substrate diffusion couple with a Mo holding stage. (a) The annealed Cu foil was prepared on a SiO_2/Si substrate ($\sim 1\text{ cm}^2$). (b) The annealed Cu foil was covered with graphite powder to fully cover the foil surface. (c) The C-Cu- SiO_2/Si substrate diffusion couple was clamped at a pressure of $\sim 1\text{MPa}$ in a molybdenum holding stage to uniformly apply the pressure. The inset in (b) shows the product information of the graphite powder used in the DAS process.

Figure 3.4. Photographs of the furnace-based DAS process of graphene frameworks. (a-b) The images show the stage in which the completed diffusion couple is loaded in a quartz tube. (c) The completed

diffusion couple was rapidly cooled to room temperature with an N₂ gun.

Figure 3.5. Removal of graphite powder from the Cu-SiO₂/Si substrate. (a) After the cooling process, the Mo holding stage was separated and (b) graphite powder was almost removed from the Cu foil surface by carefully shaking out the assembled Cu-SiO₂/Si couple with a tweezer. The inset shows the photograph of the cleaned Cu surface.

Figure 3.6. Photographs of the cleaning process of the Cu foil surface in D.I water after DAS process. (a) Removal of residual graphite powder by shaking out the assembled Cu-SiO₂/Si couple with a tweezer in D.I. water. The red dotted rectangle indicates the removed graphite powder from the Cu surface, (b) the cleaning process of the Cu foil is shown step by step and the D.I. water was put in separated petri-dishes, (c) introduction of a new a SiO₂/Si substrate in D.I. water to scoop up the cleaned Cu foil from the D.I. water.

Figure 3.7. (a-d), The new design was devised for transferring DAS-graphene framework grown on the Cu foil onto other substrates. The 1- μ m-thick Cu foil can be supported against vacuum pressure without crumbling or wrinkling. The PMMA/graphene/Cu assembly was made for transfer. (e-h), The process of etching DAS-graphene framework grown on a Cu foil is shown step by step. (NH₃)₃S₂O₈ (0.1M) solution was put in separated petri-dishes. The Cu foils were moved to other etchant by glass and etched away for (e) 2, (f) 5, (g) 10 and (h) 30 min. After etching the Cu foils over 60 min, we obtained Cu-free graphene framework.

Figure 4.1. Schematic illustration of the modified DAS process for synthesizing monolithic GO sheets on the reverse side of a Cu foil. This process includes the elementary step in the DAS process: the annealing of the Cu foil; the physical attachment of the Cu foil onto the substrate and preparation of the C-Cu-substrate diffusion couple; heating of the assembly in ambient argon (below 260 °C) and the formation of monolithic GO sheets at the Cu/substrate interface, and the detachment of the Cu foils after removal of the solid C sources from the foil surface.

Figure 4.2. Cross-sectional STEM images and corresponding energy-dispersive spectroscopy (EDS) line profiles of (a) an as-received and (b) an annealed 1- μ m-thick Cu foil at about 790°C in ambient hydrogen, respectively. Note that the O distribution within an annealed Cu foil is quite uniform from EDS after the annealing process. (c) XRD patterns of 1- μ m-thick Cu foil before and after the annealing process.

Figure 4.3. Optical images of annealed Cu foils (a,c) and GO-covered Cu foils (b,d) before (a,c) and

after (b,e) oxidation in air at 200 °C for 120 min (scale bars, 150 μm). (e,f) A bright-field TEM image of the GO sheet (scale bar, 1 μm) (e) and its corresponding selected area electron diffraction pattern (scale bar, 5 nm⁻¹). (f) Most micro-crystallites were polycrystalline.

Figure 4.4. (a) Representative Raman spectra of GO that was grown on a Cu surface at 240 °C for 60 min (bottom) and 120 min (top), and then transferred onto SiO₂ (300 nm)/Si. (b) Raman map of the G/2D bands (top) and the FWHM of the 2D band (bottom) of GO that was grown on Cu at 240 °C for 60 min and then transferred onto SiO₂ (300 nm)/Si (scale bars, 10 μm).

Figure 4.5. (a) Optical transmittance of GO that was grown on Cu at 240 °C for 60 min and then transferred onto SiO₂ (300 nm)/Si (scale bars, 10 μm). (b) a plot of $\sqrt{\epsilon} / \lambda$ versus $1/\lambda$ to determine the optical bandgap of the GO sheet.

Figure 4.6. The thickness of GO framework according to growth time from atomic force microscopy (AFM) measurements.

Figure 4.7. XPS wide-scan survey spectrum of the GO sample grown at T = 240 °C for t = 120 min. XPS spectra show the presence of significant numbers of oxygens in the resulting graphene framework.

Figure 4.8. High resolution XPS C 1s (a) and O 1s (b) line scans of GO that was grown on Cu at 240 °C for 120 min. (c) Grazing-angle FT-IR spectrum of a six-layer-stacked GO that was grown on Cu at 240 °C for 120 min and then transferred onto an atomically flat, clean surface of Au film deposited on SiO₂/Si substrate.

Figure 4.9. Investigation of atomic structure of a GO sheet. (a) Atomic resolution, plan-view TEM image of a GO sheet that was grown on a Cu surface at 240 °C for 120 min and then transferred onto a TEM grid. The colour scheme in discrete grains in TEM images represent the different crystalline structures of the GO grains. Holes are observed after the transfer process of the GO sheet onto a TEM grid (scale bar, 2 nm). (b) FFT patterns of the regions specified in (a). (c) electron energy loss spectroscopy of the GO sample grown at T = 240 °C for t = 120 min, showing the presence of significant number of oxygens in the resulting graphene framework.

Figure 5.1. Growth tendency of a monolithic GO sheet on a Cu surface with various incubation times. (a) Plot of GO coverage (black squares) and C-segment coverage (blue circles) on a Cu surface as a function of growth time at 240 °C based on the Raman structure. (b) Comparison of the Raman spectra of GO sheets that were grown on Cu at 240 °C for 5 min (blue), 15 min (green) and 120 min (black),

and then transferred onto a SiO₂ (300 nm)/Si substrate.

Figure 5.2. Illustration of typical atomic structure model for dimer molecule diffusion on Cu (111) in this study. (a) top view and (b) bird-eye view (all spheres in brown color indicate Cu atoms except two spheres in gray color which indicate the dimer of C or O).

Figure 5.3. Diagram of calculated transitional state energy of atomic or molecular diffusion on Cu (111) surface. (a) C monomer and dimer, (b) O monomer and dimer, (c) C-O and C₂O molecules.

Figure 5.4. Diagram of calculated transitional state energy of atomic or molecular diffusion on Cu (100) surface. (a) C monomer and dimer, (b) O monomer and dimer, (c) C-O and C₂O molecules.

Figure 5.5. Growth mechanism of GO sheets and origin of The C and O atoms in the GO sheets. (a) Zero-loss filtered bright-field cross-sectional TEM image of the Cu foil after DAS at 240 °C for 120 min (using an energy slit width of 10 eV to select the zero-loss peak) and (b) the corresponding C map. The yellow rectangles denote the same location in the TEM images (scale bars, 0.2 μm).

Figure 5.6. Origin of the C and O atoms and growth mechanism in the GO sheets. (a) Changes in the elemental composition of C⁻ and O⁻ containing species, based on TOF-SIMS analysis of the surfaces of an as-received Cu foil, an annealed Cu foil at 790 °C in ambient hydrogen, and a GO-covered Cu foil that was grown at 240 °C for 120 min. (b) Schematic diagram of GO growth mechanism during DAS process using soild C; C atoms began to diffuse through the Cu along the GBs of the foil while trapping the O species dissolved in the Cu, leading to the predominant diffusion of C-O molecules over Cu as well as through GBs.

Figure 6.1. (a) The heating profile of the Cu foil during annealing step. Modifying the heating profile method enable the residual O concentration in Cu. (b) Changes in the O/C composition and the calculated bandgap energy in the GO sheets that were formed on a Cu surface under three conditions. Error bars are the standard deviation of the band gap energy measured in five different samples grown under the same condition.

Figure 6.2. High resolution XPS C 1s and O 1s line scans of the GO sheets that were formed on a Cu surface under three different conditions. The GO sheets were synthesized at 240 °C for 60 minutes with the Cu foil annealed at 790 °C for 20 minutes (type I); at 240 °C for 120 minutes with the Cu foil

annealed at 790 °C for 20 minutes (type II); and at 240 °C for 120 minutes with the Cu foil annealed at 790 °C for 260 minutes (type III).

Figure 6.3. XPS depth profiles of C and O atoms in the Cu foils used after the DAS was accomplished at three different conditions. The etching processes were conducted from the GO-covered Cu surfaces and the average etch rate was about 1.9 Å/s.

Figure. 6.4. Optical microscope image of back-gated GO based FET devices. FET devices with a channel length of 5 μm and channel widths of 200 μm (O/C~0.8) and 20 μm (O/C~0.3) atop 300 nm SiO₂ with a p-Si back gate were fabricated by the conventional photolithography.

Figure 6.5. Controllable electrical properties of the GO sheets with varying the O/C composition. (a) Transfer characteristics of the GO sheets of 0.80 (type II, (a)) and 0.32 (type III, (b)) with different O/C compositions measured at temperatures ranging from 20 K to 300 K ($V_{ds} = 0.01$ V). (c,d) Minimum conductivity σ_{min} of the GO sheets with different O/C compositions of 0.80 (type II, (c)) and 0.32 (type III, (d)) at three different values of bias voltage (V_{ds}) ranging from 0.01 to 1 V as a function of $T^{-1/3}$.

Figure 6.6. Tunable electrical properties of the GO sheets with varying the O/C composition of 0.80 (type II) from 20 K to 220 K. (a,b) Transfer characteristics of the GO sheets $V_{ds} = 0.1$ V and $V_{ds} = 1$ V. (c,d) Minimum conductivity σ_{min} as a Dirac point of the GO sheets with different O/C composition of 0.80 (type II) at bias voltage (V_{ds}) ranging from 0.1 to 1 V and gate voltage ($V_g = 20$ V and $V_g = 70$ V) as a function of $T^{-1/3}$.

Figure 6.7. Tunable electrical properties of the GO sheets with varying the O/C composition of 0.32 (type III) from 20 K to 220 K. (a,b) Transfer characteristics of the GO sheets $V_{ds} = 0.1$ V and $V_{ds} = 1$ V. (c,d) Minimum conductivity σ_{min} as a Dirac point of the GO sheets with different O/C composition of 0.32 (type III) at bias voltage (V_{ds}) ranging from 0.1 to 1 V and gate voltage ($V_g = 20$ V and $V_g = 70$ V) as a function of $T^{-1/3}$.

List of figures

Table. 1.1. The comparison of key parameters of different dimensionalities in carbon allotropes.⁵

Table. 2.1. DFT calculation of activation energy barrier for single carbon atom diffusion on each configuration according to the reaction pathway.⁶⁶

Table 5.1. Calculated activation energy barriers (in eV) of the correlated diffusion of monomers, dimers, and trimmers, including C and O atoms on Cu (111) and Cu (100) surfaces.

Chapter 1. Introduction

1.1 History of Two-Dimensional (2D) Materials

One of the greatest concerns on Two-Dimensional (2D) materials research since 1930s had been believed that a strictly 2D materials could not exist in the free state, and some studies from Landau¹ and Peierls² had concluded that these crystals were thermodynamically unstable and thermal fluctuations could be able to destroy long-range order crystal structure, resulting in melting of a 2D lattice in the standard harmonic approximation³. It was presumed that any graphene nucleation sites will have large perimeter to surface ratios, favoring the formation of other carbon allotropes instead of 2D lattice structure. Despite the odds, in 2004, a group of physicists from Manchester University, UK, led by Andre Geim experimentally discovered high quality 2D crystal- graphene sheets, through a simple method by using the scotch tape.⁴

Graphene sheet is consisted of an atomic thick layer and sp^2 -hybridized carbon structure. It is surprising that carbon with sp^2 hybridization is able to form the two-dimensional graphene, the planar local structure in the closed polyhedral of the fullerene family and the cylindrical shaped carbon nanotubes, all with different physical properties as shown in Table 1.1⁵. Then, keeping the sp^2 hybridization, the 2D carbon lattice structure can be wrapped up into 0D fullerenes, rolled into 1D nanotubes, or stacked into 3D graphite (see Figure 1.1)⁶.

A buckyball as a fullerene (0D)⁷⁻⁹ is created by collapsing yet another dimension. Conceptually, it is a small segment of a carbon nanotube that has been pinched together at both ends to form a hollow sphere of carbon atoms. Named after Buckminster Fuller, an architectural engineer and science-fiction writer who designed domes with a similar shape, the 60-carbon buckyball was the first carbon nanomaterial to gain widespread attention.

1D carbon nanotubes (CNT)¹⁰⁻¹² are another nanoscale allotrope of carbon. They can be considered of as ribbons of graphene that have been into a tube. Due to the strength of the bonds in a hexagonal carbon lattice, nanotubes are one of the strongest fibers ever discovered. Additionally, due to the extra quantum confinement imposed on electrons along the circumferential axis, carbon nanotubes can display both metallic and semiconducting electric properties. The electrical nature of a nanotube stems from its physical shape, making CNTs intriguing materials for pure research and numerous electromechanical applications.

Graphene (2D) is actually the most recent carbon nanomaterial to be widely studied, but its basic structure is simple.¹³⁻¹⁴ The bonds in carbon atoms in graphene posed an alternate double arrangement that makes it perfectly conjugated in sp^2 hybridization. p_x and p_y orbitals contain one electron each, and the remaining p_z has only one electron. This p_z orbital overlaps with the p_z orbital of a neighbor carbon

atom to form a π -bond, while the remaining orbitals form σ -bonds with other neighboring carbons. The sp^2 -orbitals form the three strong covalent bonds to the nearest neighbors. These strong bonds give graphene its extraordinary mechanical strength, making it possible to have stable free-standing graphene sheets, being only one atom thick layer. The remaining p-electron per atom is delocalized over the whole graphene molecule, and responsible for the electric conductivity.

Hence, for the past few years, graphene has been attracted to their peculiar properties with high carrier mobility ($2.0 \times 10^5 \text{ cm}^2\text{V}^{-1}\text{s}^{-1}$)¹⁵, high thermal conductivity ($\sim 5000 \text{ Wm}^{-1}\text{K}^{-1}$), high Young's modulus ($\sim 1.0 \text{ TPa}$)¹⁶, intrinsic strength of 130 GPa ¹⁷, complete impermeability to any gases¹⁸, high optical transmittance ($\sim 97.7 \%$)¹⁹, and ability to sustain extremely high densities of electric current.²⁰ The extraordinary properties have motivated the development of graphene electronics such as high-frequency transistors²¹, photodetectors²², optical modulator²³, energy generation and storage²⁴, and sensors²⁵. In particular, its combination of ultimate thinness, excellent transmittance, strength, and stretchability makes graphene potentially promising for advanced flexible and/or foldable transparent devices.

As an ultimate objective to apply for electronics, the graphene synthesis methods have become an important challenge for large area and high-quality growth. Consequently, several approach to produce single or few- layer graphene have been reported to date, such as mechanical cleavage²⁶, epitaxy growth of graphene from SiC substrate²⁷, solid-carbon sources derived growth²⁸, and chemical vapor deposition (CVD)²⁹. Among them, CVD method is thoughts as one of the most promising for graphene electronics, thanks to its flexibility; it can produce not only large-area graphene sheet, but also various chemically tuned two-dimensional materials³⁰⁻³¹.

Possibilities of applications of graphene grown by CVD method have been largely demonstrated by many groups, however, closer attention should be taken to precisely control the resulting graphene layer in CVD method due to its sensitivity to various process parameters. For instance, conventional CVD based-graphene synthesis method needs high temperature more than $1000 \text{ }^\circ\text{C}$ for the efficient decomposition of carbon sources, and requires a very special care for gas flow. Furthermore, it must accompany a transfer method from metal substrate used to grow graphene to desired substrate for applications. This study intends not only to have original technology of growth, but also to functionalize controllable graphene properties and composition for graphene electronics.

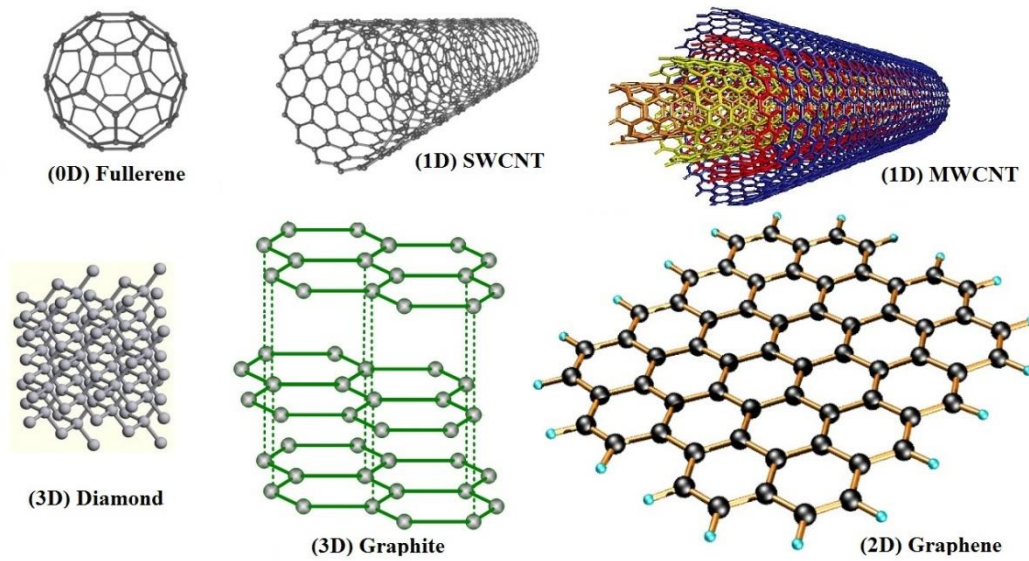


Figure 1.1. Different carbon allotropes.

Table 1.1. The comparison of key parameters of different dimensionalities in carbon allotropes⁵

Dimension	0-D	1-D	2-D	3-D
Isomer	Fullerene	Nanotube	Graphene	Graphite
Hybridization	sp^2	sp^2	sp^2	Sp^3
Density (g/cm^3)	1.72	1.2-2.0	2.26	3.515
Bond length (\AA)	1.40 (C=C) 1.46 (C-C)	1.44 (C=C)	1.42 (C=C)	1.54 (C-C)
Electronic properties	Semiconductor $E_g = 1.9 \text{ eV}$	Metal/semiconductor $E_g = \sim 0.3 - 1.1 \text{ eV}$	Zero-gap Semiconductor	Insulator

1.2 Materials Overview

1.2.1 Graphene

The unique properties of graphene stems from its sp^2 hybridization and its electronic structure of graphene follows from a simple nearest neighbor, tight-binding approximation³². Graphene crystallized in a triangular lattice with two atoms per unit cell, A and B, with

$$\vec{a}_1 = \left(\frac{\sqrt{3}}{2}a, \frac{1}{2}a\right) \text{ and } \vec{a}_2 = \left(\frac{\sqrt{3}}{2}a, \frac{1}{2}a\right) \quad (1.1)$$

Where a is the lattice parameters $\sim 2.46\text{\AA}$. Within the tight-binding method 2D energy dispersion relations of graphene can be calculated by solving the eigen-value problem for a Hamiltonian H_{g-2D} associated with the two carbon atoms in the graphene unit cell³³ in Figure 1.2. The two p_z electrons per unit cell in graphene lattice give rise to two π and π^* . For low energies, a tight-binding approach is well consisted to calculate the dispersion relation of the π -bands. A tight-binding calculation including up to second-nearest neighbor hopping yields the following equation³⁴:

$$E_{\pm}(\vec{k}) = \pm t \sqrt{3 + f(\vec{k})} - t' f(\vec{k}) \quad (1.2)$$

The solution yields the following with:

$$E_{g-2D}^{\pm} = \pm t \sqrt{1 + 4 \cos\left(\frac{\sqrt{3}k_x a}{2}\right) \cos\frac{k_y a}{2} + \cos^2\left(\frac{k_y a}{2}\right)} \quad (1.3)$$

Where the E_{g-2D}^+ and E_{g-2D}^- correspond to the π^* and the π energy bands, respectively and t is the nearest-neighbor hopping energy (hopping between different sublattice), t' the next-nearest-neighbor hopping (hopping in the same sublattice), and a_0 the distance between neighboring carbon atoms.

Figure 1.3 shows the electronic energy dispersion relations for graphene as a function of the two-dimensional wave-vector k in the hexagonal Brillouin zone, where The π and π^* bands touch exactly at the Dirac points at the corners of the Brillouin zone, at the K and K' points. For $t' \neq 0$, the electron-hole symmetry is broken, and the π and π^* become asymmetric.

The charge carriers in graphene are described by a Dirac-like spectrum, rather than the usual Schrödinger equation for nonrelativistic quantum particles. Quantum-mechanical hopping between the sublattice lead to the formation of two energy bands, and their intersection near the edges of the

Brillouin zone yields the conical energy spectrum. Figure 1.3 shows a band structure of graphene and zoom of the around the Dirac point. This shows a linear dispersion relation, $E = \hbar kv_F$, as if they were massless relativistic particles by $v_F = C/300$.³²

Therefore, in pristine graphene film, the Fermi energy lies exactly at the Dirac point: the π band is completely filled, while the π^* band is empty, where the Fermi level is located. This linear dispersion relation close to the K and K' points, the absence of a band gap and the electron-hole symmetry are the main difference from those in conventional metals and semiconductors, and it is the origin for many of the interesting properties of graphene. Controlling the position of the Fermi level with corresponding to the Dirac point by applying an electric field results in the modulate of the carrier resistance as show in Figure 1.4. A conductivity minimum is observed when the Fermi level is aligned with the Dirac point. These properties of graphene make it very attractive for application in electronics.

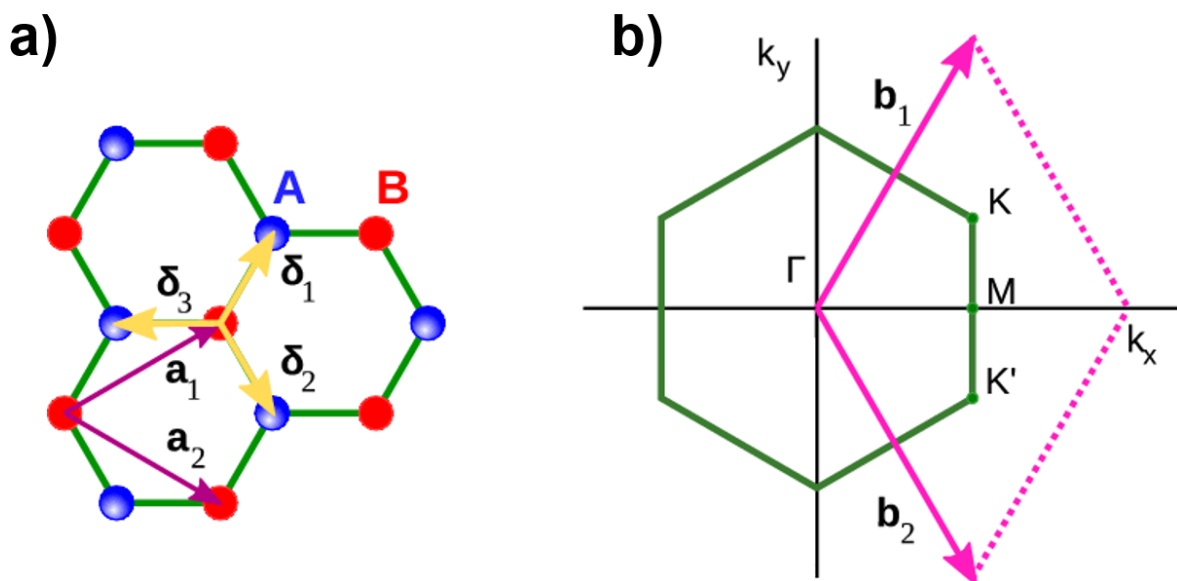


Figure 1.2. (a) Crystal structure of graphene consisting of sublattice A (blue) and B (red). The lattice vectors a_1 and a_2 as well as The vectors δ_1 , δ_2 , and δ_3 connect carbon atoms separated by a distance $a = 0.142$ nm. (b) The first Brillouin zone. Γ is the center of the cell. K and K' are the corners of the first Brillouin zone (Dirac points), and M is the center of the edge.³⁵

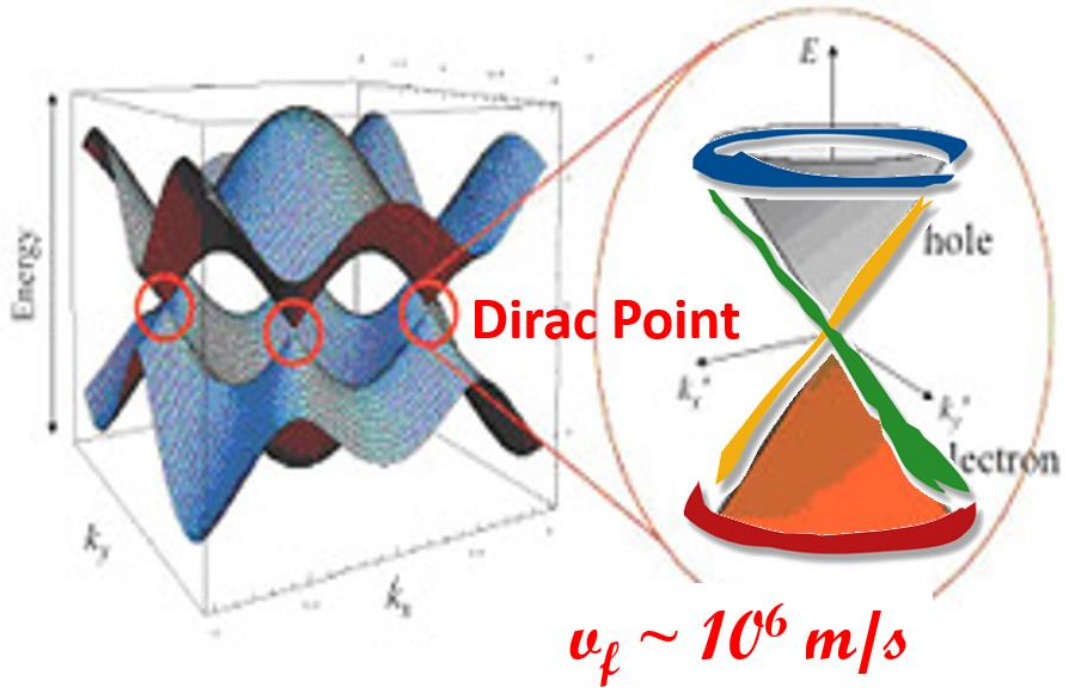


Figure 1.3. Band structure of graphene and zoom of the dispersion relation close to the K-point for small energies.³⁵

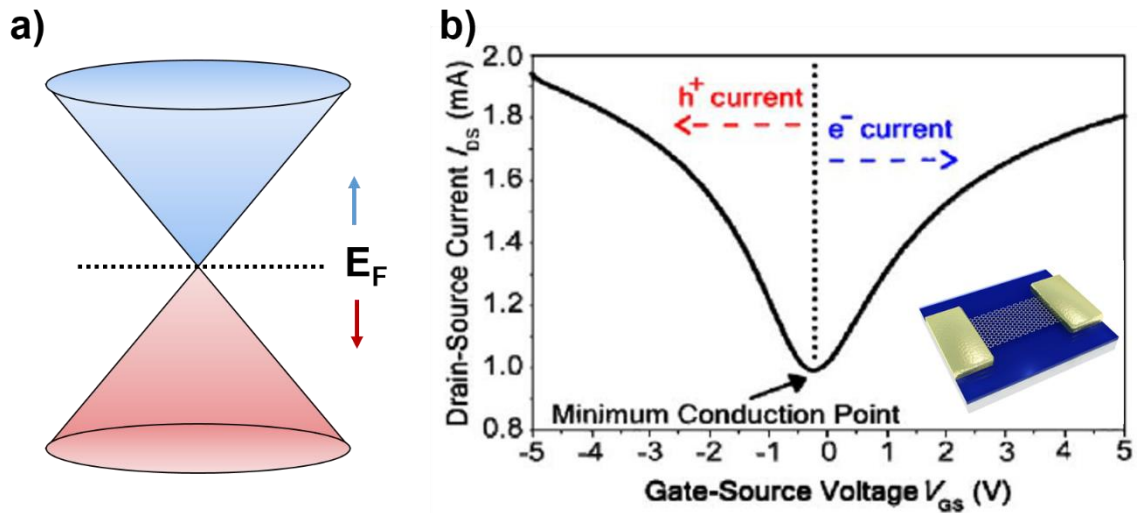


Figure 1.4. Electric field effect of a graphene based device. (a) band structure of graphene. (b) Modulating Fermi energy level of graphene by using a gate field. The Minimum conduction point is observed when the Fermi level coincides with the Dirac point.³⁵

1.2.2 Graphene Oxide (GO)

The history of graphene oxide (GO), like many other novel materials, begins with its unintended discovery. Though there is a gap of about 150 years between its creation and its renewed interest. Since it was first prepared in the nineteenth century, graphite oxide has been mainly produced by the Brodies³⁶, Staudenmaier³⁷ and Hummers methods³⁸.

As a first synthesis of GO, B.C Brodie who was a professor at the University of Oxford in 1859 was trying to find the molecular weight of graphite. Having noticed that graphite had very different properties than other forms of carbon such as diamond or charcoal, Brodie had hypothesized that graphite was a unique element and he investigated the graphite to oxidize with potassium chlorate and fuming nitric acid. Then, he observed the first ever reduction of GO sheet. However, this method was time consuming and hazardous to produce.³⁷

Hummers and Offeman also used a method that involved extremely strong oxidizers: potassium permanganate, sodium nitrate, and sulfuric acid. However, their method used fewer reagents and had no water, allowing for both a speedier and safer synthesis, as well as producing a product with a slightly higher ratio of oxidation at 2:1 carbon atoms with every 1 oxygen atoms. Thus the GO sheet was prepared using the well established hummers method. By the oxidation of graphite using strong oxidizing agents, oxygenated functionalities were introduced in the graphite structure which not only expand the layer separation from 6 to 12 Å, but also makes the material hydrophilic. This property enables the graphite oxide to be exfoliated in water using sonication or stirring, ultimately producing single or few layer GO sheets.

Figure 1.5 shows GO sheet that a layered material produced by the oxidation of graphite. In contrast to pristine graphite, GO sheets are heavily oxygenated, bearing with epoxide and hydroxyl functional groups on their basal planes, in addition to carbonyl and carboxyl groups bonded at the sheet edges. The presence of these functional groups makes GO sheets strongly hydrophilic, which is one of the advantages to be allowed GO sheet to readily swell and disperse in water (Figure 1.6). Thus, this property can be attributed to improving their electrical and mechanical properties when mixing the materials with ceramic or polymer matrixes. Therefore it can be used in various materials forms.

Otherwise, in terms of electrical conductivity, GO sheets were described as an electrical insulator, due to the disruption of its sp^2 bonding networks. In order to recover the honeycomb hexagonal lattice, and with it the electrical conductivity, the reduction of GO had been challenged.

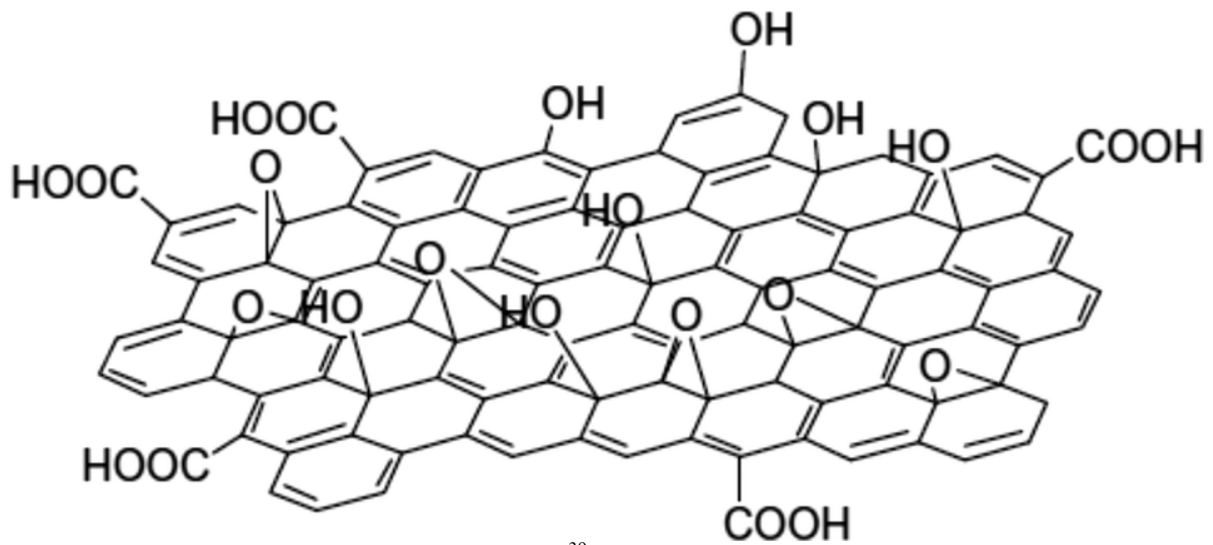


Figure 1.5. Proposed structure of the GO sheet.³⁹

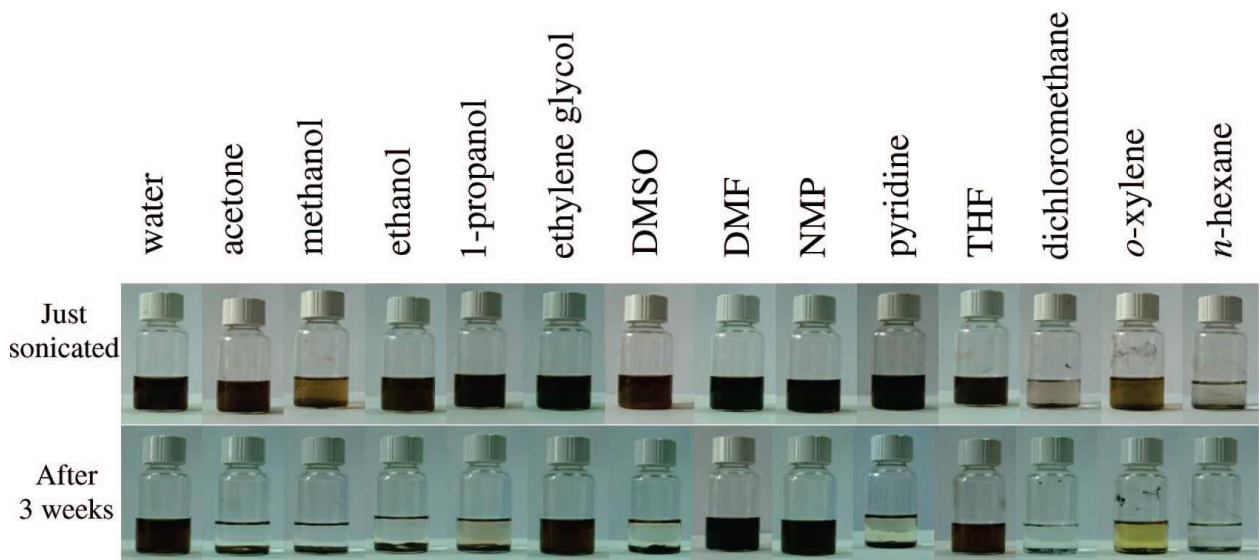


Figure 1.6. As-prepared graphite oxide dispersed in water and various organic solvents.⁴⁰

1.2.3 Reduced Graphene Oxide (RGO)

Although functionalized GO sheets can be dispersed in variety of colloidal suspensions⁴⁰, the resulting GO sheets are electrically insulating due to disruption of the sp^2 hybridized-graphitic networks. In addition, the Insulating property of GO, unlike graphite, limits its usefulness for the synthesis of conductive nanocomposites. However, many research groups have demonstrated that the electrical conductivity of GO can be significantly increased by chemical reduction, probably due to the restoration of a graphitic network of sp^2 bonds.⁴¹⁻⁴⁴ The reduction chemical methods: hydrazine⁴⁵, dimethylhydrazine⁴⁶, hydroquinone⁴⁷ and $NaBH_4$, thermal methods⁴⁸ and ultraviolet-assisted method have been used for electrically conducting GO sheets. However, elemental analysis of RGO sheets by other group⁴⁹⁻⁵⁰ exhibited the existence of a significant amount of oxygen, indicating that RGO sheet is not the same as pristine graphene. Theoretical calculations of the RGO indicated that reduction below 6.25% of the area of the GO sheet (Carbon to Oxygen (C/O) ratio = 16 in atomic ratio) may be difficult in terms of removing the remaining hydroxyl groups.⁵¹ However, one of the interesting features of RGO is the bandgap opening, relying on converting the insulating GO into more conductive form by reduction methods⁴⁵⁻⁴⁸. Some researchers reported tunable band gap properties that Few-layer RGO sheets can be controlled with banding energy range from 2.2 eV to 0.5 eV via a low temperature approach⁵² and GO sheet using hydrazine vapors improved evidences of controlled removal of chemical functionalized oxygen groups corresponding increase in the C/O ratios with decrease in its optical energy gap from 3.5 eV down to 1 eV.⁵³ As a result, even though RGO films are not perfect as much as pristine graphene films, it can be open possibilities for tuning its optical and electronic properties for applying to a broad range of applications.

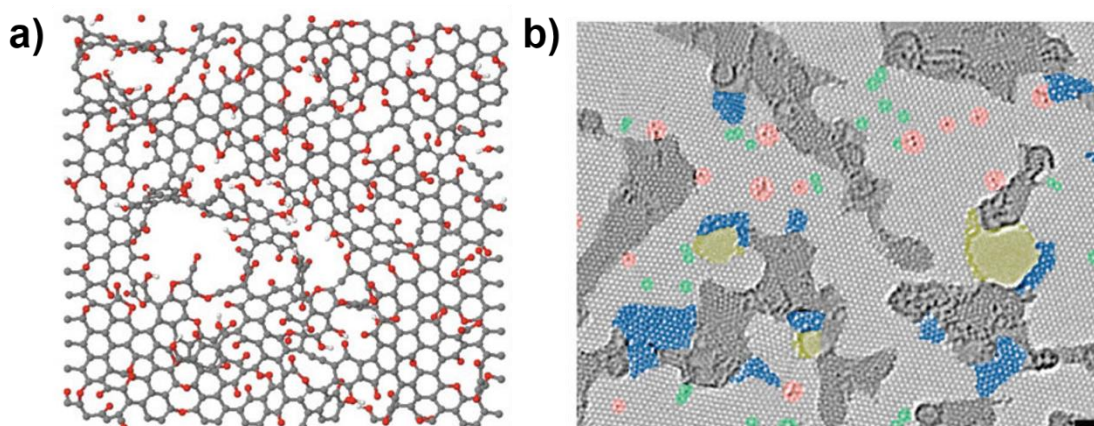


Figure 1.7. (a) Schematic illustration of disordered RGO basal plane consisting of holes, topological defects and remnants of oxygen groups.⁵⁴ (b) Atomic resolution, aberration-corrected high-resolution transmission electron micrograph of a single-layer RGO membrane⁵⁵.

1.3 Synthesis of 2D Materials

1.3.1 Mechanical Exfoliation

Most of this work used graphene created by a process of mechanical exfoliation called the “scotch tape method”. In this procedure, pure samples of bulk graphite as well as other 2D crystals are placed on the sticky side of commercial adhesive tape. The tape is pressed on a desired substrate and then peeled away. Flakes of graphene up to 50 microns wide are left on the substrate. The flakes can be discerned under an optical microscope due to thin-film interference, appearing as a region of slight discoloration.⁵⁶ The graphene left by the scotch tape method is pure and clean, which enables researchers to measure its electrical and mechanical properties. For similarly, Transition Metal Dichalcogenides (TMDs) have been founded in individual sheets from their parent crystals by mechanical exfoliation. Under normal circumstances, this method can be useful for top-down techniques.

1.3.2 Epitaxy Growth

Epitaxial growth method is the one of the interesting technique for creating high quality monolayer graphene. Originally, epitaxial graphene was grown from silicon carbide (SiC) substrate. When bulk SiC is heated to around 1500 °C, some of the silicon sublimates, leaving a layer of graphene sheet behind on the surface.⁵⁷⁻⁵⁸ Another method of creating epitaxial graphene from SiC is that of molecular beam epitaxy. A graphite filament is loaded into an ultra-high vacuum. As the filament is heated, carbon atoms sublime off of the graphite. These carbons form sp^2 atomic structure by a molecular beam in the vacuum, traveling through free space without interacting until they land on a metallic substrate and form a graphene layer.⁵³ while molecular beam epitaxy could produce high-quality uniform films over a large surface, it requires an ultra-high vacuum which makes the process tedious and inaccessible to smaller groups.

1.3.3 Chemical Vapor Deposition (CVD)

The representative graphene growth method is considered as the CVD method. CVD synthesis method using on transition metal substrate such as nickel and copper etc. to growth graphene have been immensely successful over the years in producing high quality and large area synthesis.⁵⁹⁻⁶⁰ Figure 1.10 shows growth kinetics in CVD process on Ni and Cu substrate. The process begins with an atomically flat surface and a carbon precursor in methane or ethylene. The transition metal substrates play the role of catalyst for dissociation carbon containing molecules. The substrate is placed in a furnace equipped with gas delivery system. The precursor molecules will be brought into contact with the substrate

surface from the gas phase at low pressure and the flow of hydrogen atoms can catalyze a reaction between methane and the surface of the metal substrate, causing carbon atoms from the methane to be deposited onto the surface of the metal through chemical adsorption. Upon reach onto the surface, the precursor molecules are cracked to form carbon atoms, leaving carbon adatoms attached to the surface as a free state of carbon atoms and then graphene is formed when carbon atoms after diffusion on the metal surface, encounter other carbon atoms and form bonds. In order to obtain the lowest energy single layer, the conditions have to be carefully controlled. The described CVD method provides access to large area graphene, but the challenge remains to obtain fine control over film thickness and crystallinity. In addition, graphene grown using CVD method on metal substrate is always polycrystalline consisting of many grain boundaries.⁶¹

1.3.4 Rapid Thermal Annealing

Large-area graphene films can be grown on a nickel surface by rapid thermal annealing (RTA) in vacuum as shown in Figure 1.11.⁶² The instability of nickel films in air owing to high solubility of carbon atoms facilitates the spontaneous formation of ultrathin (< 2-3 nm) carbon- and oxygen-containing compounds on a nickel surface. The high-temperature annealing of the nickel films deposited on SiO₂/Si substrate without the introduction of intentional carbon-containing precursors results in the formation of few-layer graphene films with high crystallinity. From annealing temperature and ambient studies during RTA, growth mechanism of RTA method was found that the evaporation of oxygen atoms from the surface is the dominant factor affecting the formation of graphene films. The thickness of the graphene layers is strongly dependent on the RTA temperature and time and the resulting films have a limited thickness less than 2 nm even for an extended RTA time.

As a modified RTA method, a single-layer graphene has been uniformly grown on a Cu surface at elevated temperature by thermally decomposition of a poly(methyl methacrylate) (PMMA) film.⁵⁷ The closer examination of chemistry transition from solid-carbon source to graphene on the catalytic Cu surface was investigated by *in-situ* residual gas analysis during PMMA/Cu foil samples being heated, in combination with interrupted growth studies to reconstruct *ex-situ* the heating process. The results of the experiments clearly show that the formation of graphene occurs with hydrocarbon molecules vaporized from PMMA, such as methane and/or methyl radicals, as precursors rather than by the direct graphitization of solid-state carbon. both the heating temperature profile and the amount of a solid carbon feedstock are the dominant factors to determine the crystalline quality of the resulting graphene film.⁶³ (see Figure 1.12)

1.3.5 Hummer Method

In 1957 Hummer and Offeman have developed a safer, quicker and more efficient process called the Hummer's method, using a mixture of sulfuric acid (H_2SO_4), sodium nitrate (NaNO_3), and potassium permanganate (KMnO_4), which is still widely used, often with some modifications.^{38,64} Graphite chemical oxidation involves interaction of oxygen-containing groups in interlayer space. Embedded oxygen breaks van der Waals forces that hold layers together and the interlayer distance is increased. The maximally oxidized bulk product is C:O ration between 2.1 and 2.9 with a much larger and irregular spacing. Carbon-oxygen bonds cause partial change of carbon atoms hybridization from sp^2 to sp^3 and change in graphene layers arrangement into turbostatic structure.

One of the modified Hummer's method for synthesizing GO sheet from graphene powder introduce as shown in Figure 1.13.⁶⁵ In brief, 1 g of graphite and 0.5 g of sodium nitrate were mixed together followed by the addition of 23 ml of concentration sulphuric acid under constant stirring. After 1 h, 3 g of KMnO_4 was added gradually to the above solution while keeping the temperature less than $20\text{ }^\circ\text{C}$ to prevent overheating and explosion. The mixture was stirred at $35\text{ }^\circ\text{C}$ for 12 h and the resulting solution was diluted by adding 500 ml of water under vigorous stirring. To ensure the completion of reaction with KMnO_4 , the suspension was further treated with 30% H_2O_2 solution (5 ml). The resulting mixture by filtration and drying, GO sheets were thus obtained.⁵⁹

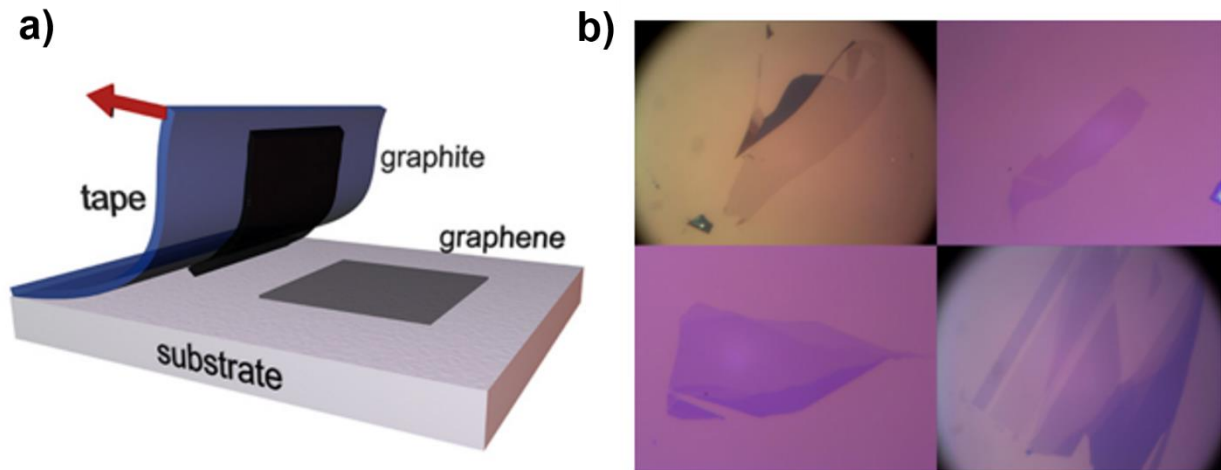


Figure 1.8. (a) Schematic illustration of the exfoliation process. (b) Optical microscope images of graphene flakes (single-, bi- and tri- layer samples). (adapted from GLAB)

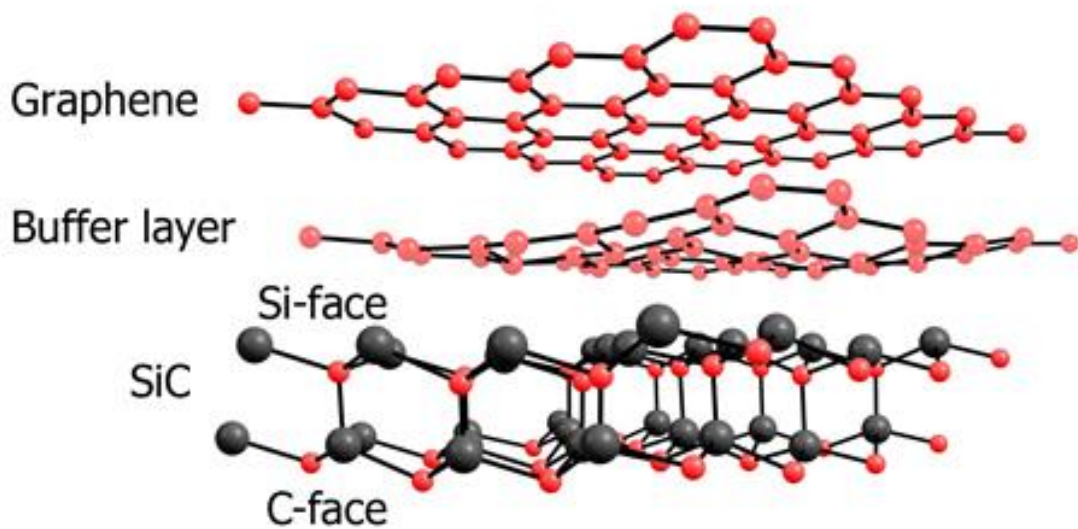


Figure 1.9. Schematic illustration of epitaxial graphene growth on a silicon carbide (SiC) substrate. (adapted from Bart J. van wees Lab)

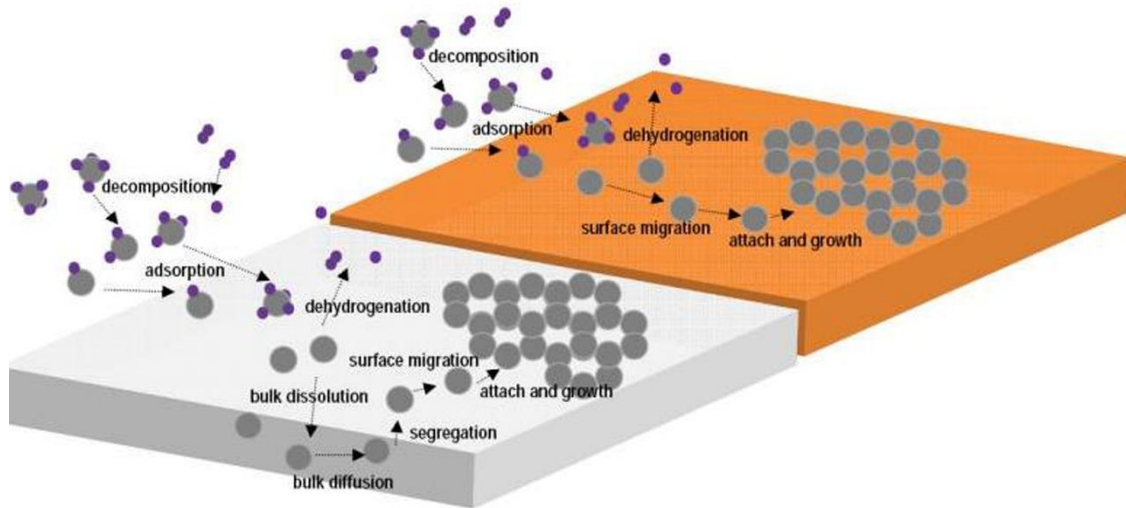


Figure 1.10. Schematic illustration of growth kinetics in CVD graphene on different catalyst on Ni (right) and Cu (left) substrate.

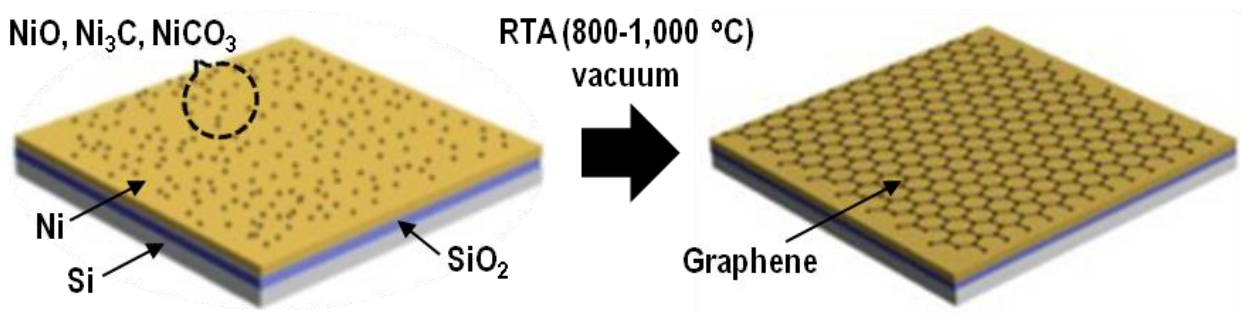


Figure 1.11. Schematic illustration for nickel-assisted facile synthesis method of few-layer graphene by RTA method⁵⁶.

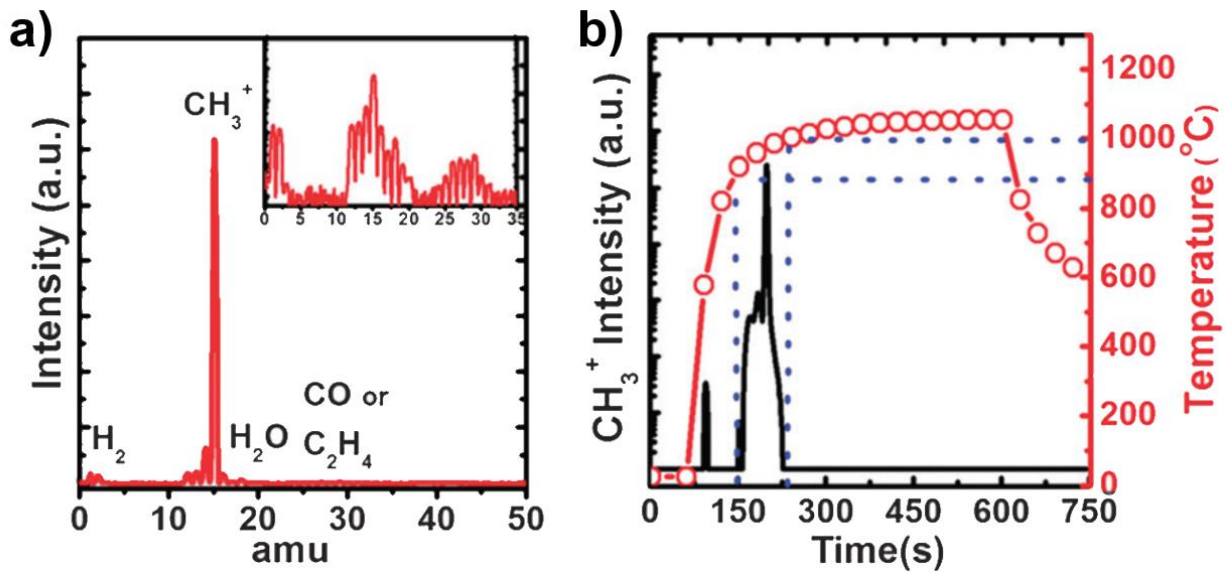


Figure 1.12. (a) *In situ* quadrupole mass spectrum while ramping temperature from 25 $^\circ\text{C}$ to 1000 $^\circ\text{C}$ under vacuum ($\sim 10^{-9}$ torr) of a 10 wt% of PMMA-coated Cu foil. Inset shows the logarithm of partial pressure. (b) CH_3^+ partial pressure versus heating time.⁵⁷

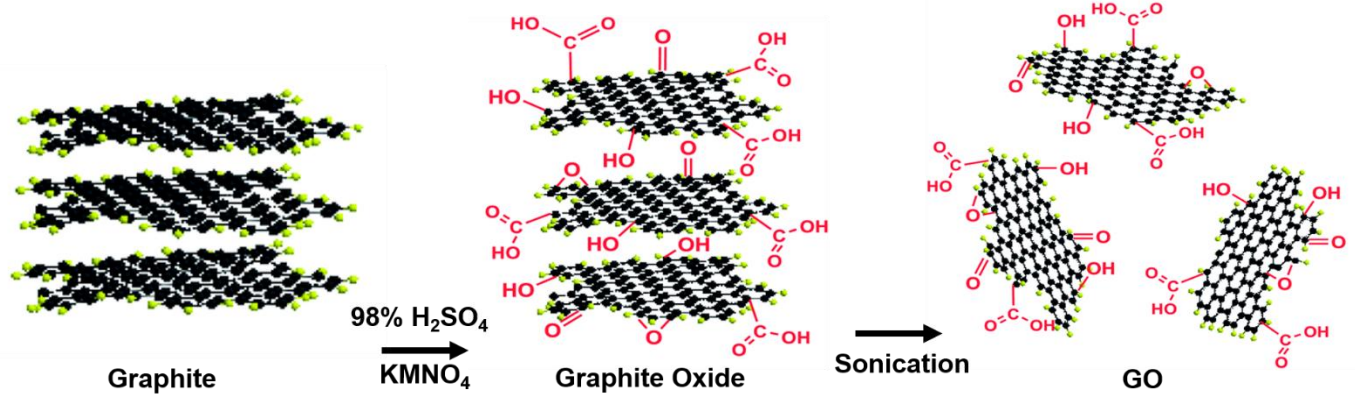


Figure 1.13. Schematic representation of GO synthesis by modified hummer method. Graphite oxide consists of a layered structure of GO sheets that are strongly hydrophilic bearing with oxygen functional groups. Increase interlayer distance between GO sheets from 6 to 12 \AA with increasing relative humidity. Consequently, graphite oxide can be completely exfoliated to produce aqueous suspension of GO sheets by simple sonication method.

Chapter 2. Methodology Review

2.1 Low-Temperature Synthesis of Transfer-Free Graphene Films

2.1.1 Diffusion Assisted Synthesis (DAS) Method

Our group reported near room-temperature synthesis of transfer-free graphene synthesis method in 2012, which is refer to Diffusion Assisted Synthesis (DAS) method.⁶⁶ In contrast to other graphene growth method⁵⁶⁻⁶⁵, we devised a new method for the synthesis of graphene films directly on SiO₂/Si substrates, even plastics and non-conducting substrate near room temperature (25-160 °C). DAS method showed an ability to controllably synthesize graphene films onto desired substrates at low temperature and opened up new possibilities for fabrication of graphene electronics. It was very important because high temperature (~1,000 °C) growth process like CVD method and transfer process after a growth tends to restrict use of graphene films in nano-electronic applications.

The key idea in synthesis methodology was diffusion of carbon through a diffusion couple made up of carbon-nickel/substrate to form graphene underneath the nickel film at the nickel-substrate interface. The resulting graphene layers indicate controllable crystalline structural and optical properties by nickel grain boundary engineering. It is worth noticing that DAS method allows for uniform and controllable deposition of wrinkle-free graphene films with micrometer-sized grains on SiO₂ surfaces, and with nanometer-sized grains on plastic and glass. How does graphene form at such low temperatures? Graphene growth mechanism of DAS Process was proposed as follows 4 elementary step of the process; 1) Dissociation of C-C bonds on nickel film, 2) Diffusion of carbon atoms, 3) Nucleation, and 4) Growth at the Ni-SiO₂ interface as shown in Figure 2.1. First, previous experimental and theoretical studies showed that catalytic metal such as nickel, copper etc. can catalyze the dissociation of C-C bonds and promote diffusion even at room temperature. Second dissociated carbon atoms from solid source is supposed to diffuse through Ni film along the grain boundary depending on growth temperature and crystallize as graphene at the Ni-SiO₂ interface. Eventually, a continuous polycrystalline graphene films were directly grown with tunable crystalline structure of graphene.

In case of 460 °C < T < 600 °C, we observed the formation of nanocrystalline graphene layers. Otherwise, in T < 260 °C, graphene films covered mostly with monolayer and bi-layer graphene were growth over large area with micrometer- sized crystalline structure as shown in Figure 2.2. Interestingly, we found the morphologies of a few regions with multilayer graphene resemble those of the grains, and grain boundaries in the nickel thin films, which is referred as graphene ridges. We verified the ridge composition to be graphene and not amorphous carbon. These observation suggests grain boundary diffusion can serve as nucleation sites during growth and is typically faster than bulk diffusion.

Following Fisher⁶⁷ and balluffi and Blakely⁶⁸, we estimated the ratio of two transport fluxes of carbon atoms through the Ni lattice (\dot{n}_L) and along the GBs (\dot{n}_{GB}) in (111) textured Ni films and it is indicated that lower temperature greatly favour grain boundary diffusion relative to lattice diffusion ($\dot{n}_{GB} \gg \dot{n}_L$). This is consistent with the fact that graphene growth mechanisms in DAS process was well explained with diffusion flux ratios between GBs and lattice depending on growth temperature. Eventually, a continuous but polycrystalline graphene film form at the Ni-SiO₂ interface at even near room temperature and grain sizes in graphene layers can be controlled from a few hundred nanometers to a few micrometres by Ni GB engineering.

2.1.2 Grain boundary theory

Grain boundary (GB) diffusion engineering is able to controls the evolution of structure and properties of engineering materials at elevated temperatures. A knowledge of diffusion characteristics of GBs and fundamental understanding of this phenomenon are a key role for satisfactory interpretation of engineering crystalline structure depending on growth temperature in DAS process.

There are three types of paths along which diffusion can occur in crystalline solids: volume diffusion through the interiors of crystals, grain boundary diffusion along the disordered internal interfaces of polycrystalline, and surface diffusion over single crystals or polycrystalline. At low temperature, the high rate of penetration into grain boundary diffusion in polycrystalline takes place much more rapidly than does penetration into volume diffusion. At higher temperature, the rates of penetration approach one another and very nearly become equal.

In order to facilitate quantitative investigation of grain boundary and surface diffusion, most mathematical explanation of GB diffusion is based on Fisher's model⁶⁷, which consider diffusion along a single GB. According to Fisher's model, the GB is represented by a high-diffusivity, uniform, and isotropic slab embedded in a low-diffusivity isotropic crystal perpendicular to its surface as shown in Figure 2.3 for the sake of explanation let it consider rectangular grains of width d and grain boundary of width δ .

Volume diffusion follows flux

$$J_l = - D_v \frac{dc}{dx} \quad (2.1)$$

Grain boundary diffusion follows flux

$$J_{gb} = - D_{gb} \frac{dc}{dx} \quad (2.2)$$

The effective flux can be written as ($\delta \ll d$)

$$J_{eff} = \frac{dJ_v + \delta J_{gb}}{d + \delta} \approx \frac{dJ_v + \delta J_{gb}}{d} = - \left(D_v + \frac{\delta}{d} D_{gb} \right) \frac{dc}{dx} = - D_{eff} \frac{dc}{dx} \quad (2.3)$$

It can be written as

$$D_{eff} = (1 - g)D_v + gD_{gb} \quad (2.4)$$

g is the fraction of grain boundary area

Since activation energy for GB diffusion is always less than the activation energy for volume diffusion, $D_{gb} > D_v$ (Diffusion rate through grain boundary is always higher). Contribution from grain boundary is actually the diffusion rate multiplied by fraction of grain boundary area. There will be a sharp change in the slope when diffusion process transforms from mainly volume diffusion controlled to the diffusion process mainly controlled by grain boundary diffusion. I note that in practical experiments, materials are generally polycrystalline and we always measure effective diffusion coefficient only, not separately, volume or grain boundary diffusion coefficients.

A GB diffusion for applying to experiment is a complicated process that involves several elementary processes, such as diffusion along the GBs, direct volume diffusion from the surface, partial leakage from the GBs to the volume, and the consequent volume diffusion near the GBs. In fine-grained polycrystalline materials, diffusion transport between individual GBs can also play an important role and selectively design diffusion procedures. Depending on the relative importance of such elementary processes, one can observe essentially regimes of kinetics, or different situations. In each regime there are one or two elementary processes that essentially control the overall kinetics. Each regime prevails in a certain domain of diffusion-anneal temperatures, grain sizes, times, and/or other relevant parameters. The knowledge of all possible regimes is extremely important for both designing diffusion experiments and interpreting their results. This is because the diffusion phenomenon that can be extracted from the penetration profile depend on the kinetic regime and should therefore be identified a priori. We shall consider Harrison's classification of diffusion kinetics⁶⁹, which introduces three regimes called type A, B and C as show in Figure 2.4.

In type A kinetics, as a lower temperature than others and/or shorter anneal times, it arrives at the situation when volume diffusion is almost 'frozen out', and diffusion takes place only along the GBs,

without any essential leakage to the volume. In this type A,

$$\text{it have} \quad (Dt)^{1/2} \ll \delta \quad (2.5)$$

If the temperature is higher, and/or the diffusion anneal is longer, diffusion process is dominated by the B regime. The condition of this regime is

$$\delta \ll (Dt)^{1/2} \ll d \quad (2.6)$$

Here, GB diffusion takes place simultaneously with volume around the GBs, but in contrast to the A regime the volume diffusion fields of neighbouring GBs overlap each other, which means that the tracer penetrates along the GBs much wider than in type A.

The C regime is observed in the limiting case of high temperatures, and/or very long anneals, and/or small grain sizes. In such condition the volume diffusion length, $(Dt)^{1/2}$, is greater than the spacing d between the GBs and the volume diffusion fields around neighbouring GBs overlap each other extensively. Thus, the condition of type A kinetics is:

$$(Dt)^{1/2} \gg d \quad (2.7)$$

Under this condition an average tracer atom visits many grains and GBs during the t_{anneal} time t . On a macroscopic scale the whole system appears to obey Fick's law for a homogeneous medium with some effective diffusion coefficient D_{eff} (2.4).

In type C the overall flux is mainly because of the volume diffusion, since the GBs will be much smaller than the lattice. Similarly in the type A, the diffusion is mainly from GBs diffusion. However, in type B, both volume and GBs diffusion can have reasonable contribution and we need to develop the treatment to determine the diffusion rates from different contributions.

2.1.3 Fisher model in DAS process

In order to facilitate quantitative investigation of grain boundary diffusion in DAS process, we mathematically calculated grain boundary diffusion at low temperature through Fisher model. Highly idealized polycrystalline nickel film matrix figure it out with square-shaped grains of side l , grain boundary slabs of width δ , and film thickness d as shown in Figure 2.3. As for calculation of diffusion mechanism, we consider only the lattice and GBs diffusion quantities in the face-centered cubic (FCC)

in Ni (111) film (dislocation quantity is not considered here).

Under these conditions, the number of atoms (\check{n}_i) that flow per unit time is essentially equal to the product of the appropriate diffusivity (D_i), concentration gradient (dc/dx), and transport area involved and ratio of two fluxes can be estimated for FCC metals as

$$\frac{\check{n}_{GB}}{\check{n}_L} = \frac{\delta \cdot D_{GB}}{l \cdot D_L} \quad (2.8)$$

$$\frac{\check{n}_{GB}}{\check{n}_L} = \left[\frac{(3 \times 10^{-8})}{l(cm)} \right] \exp\left(\frac{8.1 \cdot T_m}{T}\right) \quad (2.9)$$

Where L and GB are lattice (volume) and grain boundary quantities, T_m is the melting temperature. Assuming $l = 10 \text{ mm} = 10^{-3} \text{ cm}$ and using T_m of Ni = 1726 K.

We have

$$\frac{\check{n}_{GB}}{\check{n}_L} = \frac{\delta \cdot D_{GB}}{l \cdot D_L} = 2.06 \times 10^8 \text{ (473 k), Growth regime (Type A)} \quad (2.10)$$

$$\frac{\check{n}_{GB}}{\check{n}_L} = \frac{\delta \cdot D_{GB}}{l \cdot D_L} = 2.15 \times 10^3 \text{ (773 k), Growth regime (Type C)} \quad (2.11)$$

Even if we consider the facts that real polycrystalline films contain various types and orientations of grain boundaries and the lattice diffusion of carbon atoms in nickel film would occur by interstitial diffusion rather than substitutional diffusion used in the model, it is evident that lower temperatures greatly favor grain boundary diffusion relative to lattice diffusion.

2.1.4 Density functional theory calculation of a single carbon atom diffusion on a graphene sheet, on a free Ni (111) surface, and along the graphene-Ni (111) interface.

Density functional theory calculation estimated activation energy barrier of a single carbon atom diffusion on a graphene sheet, on a free Ni(111) surface, and along the graphene-Ni(111) interface. All calculations were applied to using the Vienna Ab-initio Simulation Package (VASP) based on the spin-polarized density functional theory⁷⁰⁻⁷¹. A projector augmented wave potential and the generalized gradient approximation of Perdew and Wang were used here. All configurations were fully relaxed until the maximum residual forces were less than 0.01 eV/Å. The kinetic energy cutoff was 400 eV and the

Monkhorst-Pack k-point grid was 5 x 5x 1.

First, we investigated the stable adsorption site of a single carbon atoms on a free-standing graphene sheet. The graphene model consisted of 32 carbon atoms with periodic boundary conditions along the in-plane directions. We found that a bridge-like site, where the added carbon atom sits on the center of the bond between two neighboring carbon atoms of graphene, is most favorable. To obtain the pre-factor for the Arrhenius equation, the vibrational frequency of the added carbon atom on the adsorption site was calculated. The adsorption energy and the vibrational frequency of the added carbon atom on the site were found to be 1.65 eV and 22.8 THz, respectively. In addition, the minimum energy pathway for the adatom diffusion was calculated by the nudged elastic band (NEB) method. The additional carbon atoms in both initial and final configurations were located at the most energetically favorable sites which were neighboring each other. The minimum energy barrier was determined to be 0.24 eV, which was optimized along the diffusion pathway through nine intermediate images initially constructed by a linear interpolation between the initial and final configurations.

Second, an activation energy barrier of a single carbon atom diffusion on a free Ni(111) surface was calculated with Ni thin film model consisted of 6 Ni(111) layers with 15 Ni atoms in each layer for a total of 96 Ni atoms. Periodic boundary conditions were applied along the in-plane directions, while the three bottom layers of the Ni film were held fixed during the diffusion process. We found that the carbon atom is most stable on the HCP site, for which the adsorption energy is 7.01 eV, just 0.06 eV higher than on FCC site. The resulting energy barrier for the carbon atom diffusion on the Ni(111) surface is 0.49 eV.

Third, in order to investigate the diffusion of a single carbon atom along the graphene-Ni(111) interface, 8 carbon atoms for a graphene sheet and 24 nickel atoms for the Ni(111) surface were used. The graphene sheet was bi-axially stretched using 1.22% tensile strain to remove the lattice mismatch between graphene and the Ni(111) surface. The equilibrium distance between the graphene sheet and the Ni(111) surface is 3.286 Å, and the interaction energy is 0.02 eV per each carbon atom. When we introduce an additional carbon atom at the interface between graphene and the Ni(111) surface, the energetically preferred position for the carbon atom is in the HCP site on the Ni(111) surface. The distance between the carbon atom and the Ni surface is 1.03 Å and the distance between the carbon atom and the graphene sheet is 2.62 Å, which indicates that the diffusion of a carbon atom along the interface will be more strongly influenced by the Ni surface than the graphene monolayer. The calculated diffusion barrier from the HCP site to the FCC site on the Ni(111) surface along the interface is found to be ~0.51 eV, which is slightly higher than that on a free Ni(111) surface. During the diffusion, there is no significant change in the distance between the carbon atom and the Ni surface. Table 2.1

summarize DFT calculation of activation energy barrier for single carbon atom diffusion on each configuration according to the reaction pathway.

Meanwhile, the hopping rate of a carbon atom can be found by the Arrhenius equation

$$\Gamma = \Gamma_0 \exp\left(\frac{-E_b}{KT}\right) \quad (2.12)$$

Which results in a room temperature hopping rate of about 20,000/s with an attempt frequency of $\Gamma_0 = 1.0 \times 10^{13}$ Hz. In addition, the tracer diffusion coefficient can be expressed in terms of the hopping rate Γ and the mean square jump length $\langle l^2 \rangle$: $D_t = \Gamma \langle l^2 \rangle / (2d)$, and is found to be $\sim 200 \text{ nm}^2 \text{ s}^{-1}$ using the lattice constant of Ni 3.52 Å. If the chemical diffusion or the presence of graphene edges were considered, the diffusion coefficient would be higher than the calculated value of D_t .

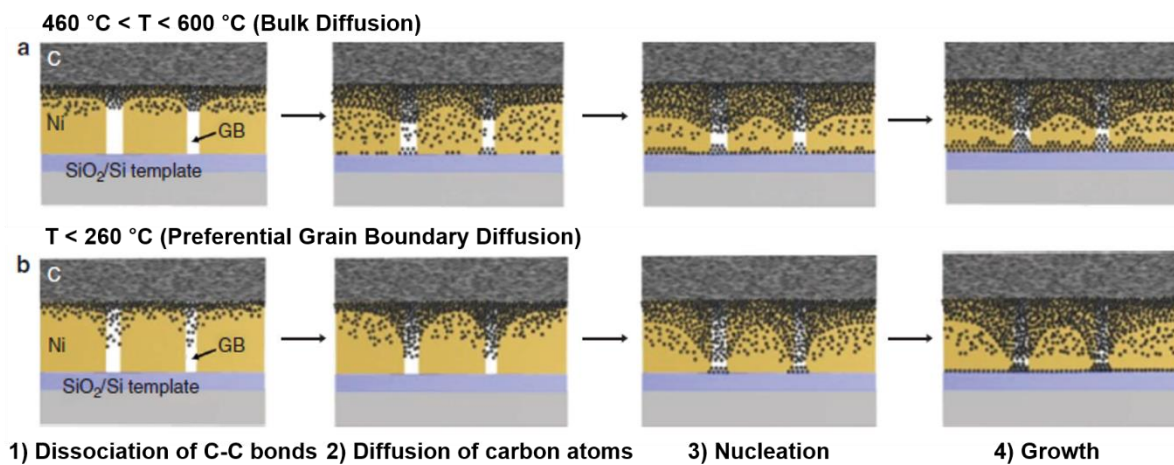


Figure 2.1. The schematic diagram of graphene growth mechanism in DAS process. The elementary steps of the process exhibit dissociation of C-C bonds at C/Ni interface, diffusion of carbon atoms, followed by nucleation and growth of graphene. (a) $460\text{ }^{\circ}\text{C} \leq T \leq 600\text{ }^{\circ}\text{C}$; bulk diffusion through Ni crystallites, leading to homogeneous nucleation and multiple sites resulting in the formation of nanocrystalline graphene film by precipitation and (b) $T \leq 260\text{ }^{\circ}\text{C}$; preferential diffusion of C atoms via lateral diffusion of C atoms along Ni/substrate interface.⁶⁶

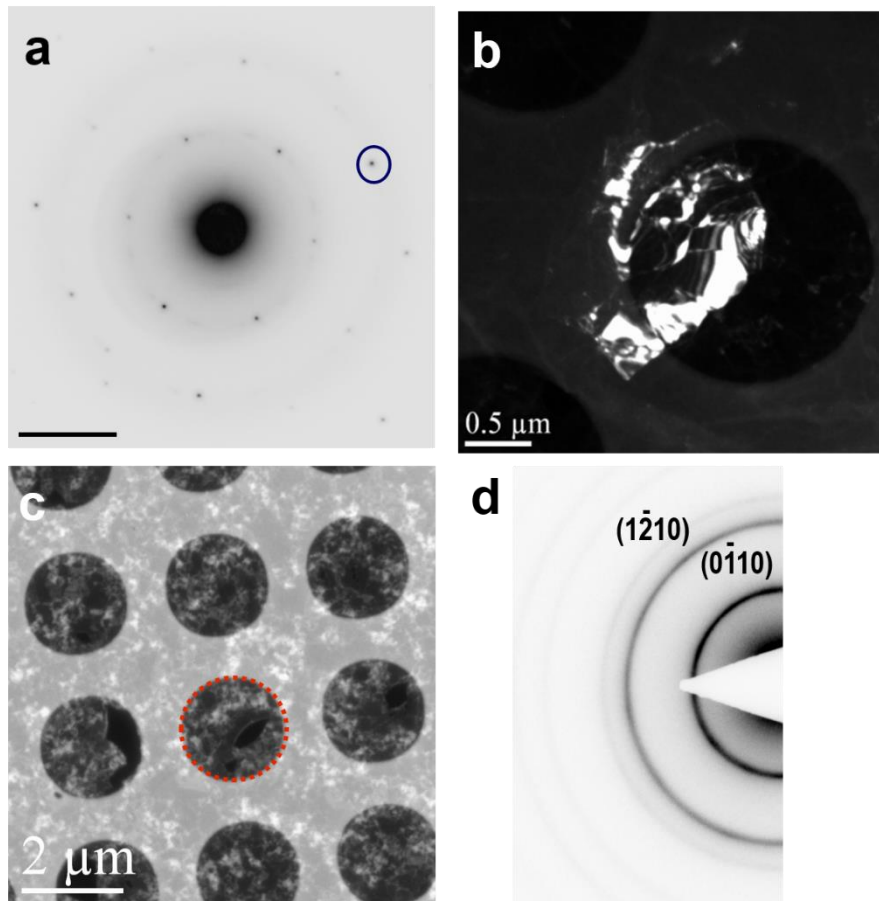


Figure 2.2. Large size grain of graphene grown at $T = 160\text{ }^{\circ}\text{C}$ on SiO_2 using dark-field TEM. a, Selective area diffraction pattern taken from graphene using 300 nm diameter aperture, showing a single hexagonal diffraction pattern. This reveals that the grain size is larger than 300 nm. Scale bar is 10 $1/\text{nm}$. b, a dark-field image obtained using a $g(1\bar{2}10)$ spot (blue circle in a) shows the real-space shape of these grains. c, Low magnification plan-view TEM image of nanocrystalline graphene films grown at $T \geq 460\text{ }^{\circ}\text{C}$ for 5min on SiO_2/Si substrates. d, selected area diffraction from red circle in c, which displays continuous ring patterns. The two diffraction rings correspond to graphene crystal plane $(0\bar{1}10)$ and $(1\bar{2}10)$. Scale bar is 5 $1/\text{nm}$.⁶⁶

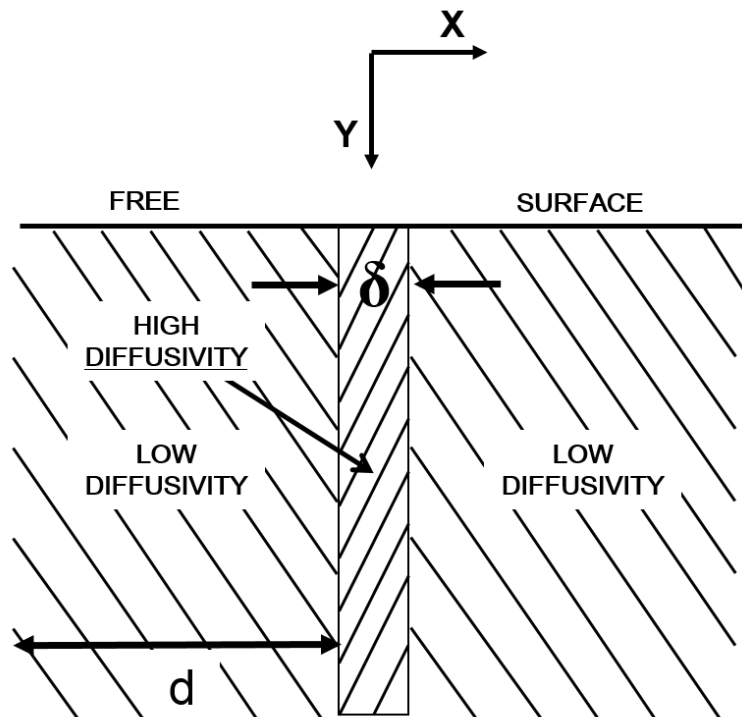


Figure 2.3. Schematic geometry in the Fisher model of GB diffusion.⁶⁷

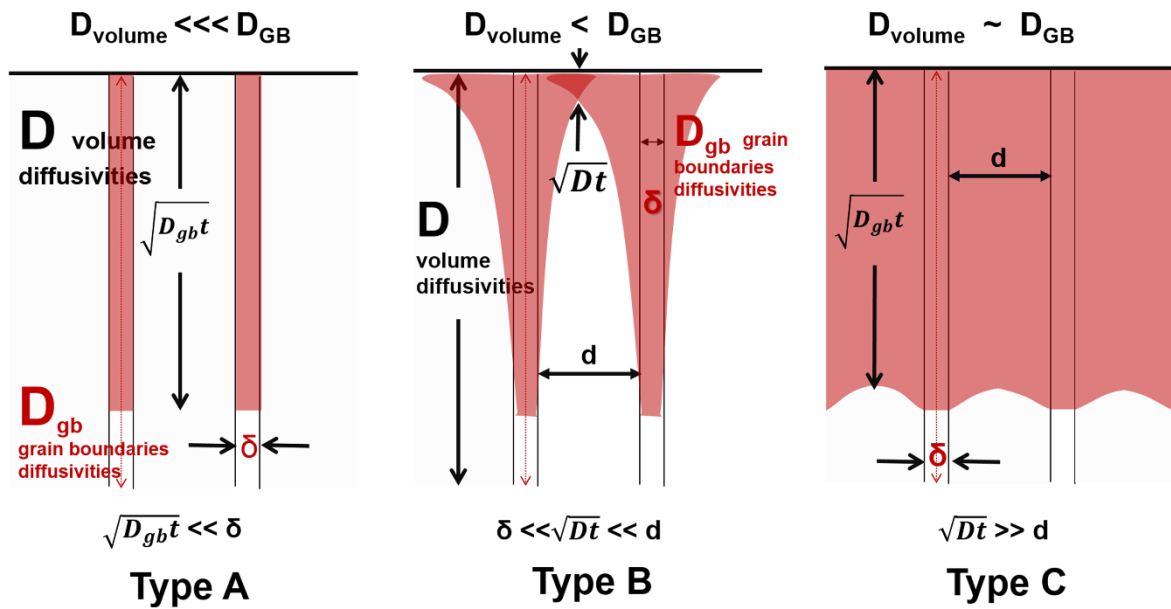
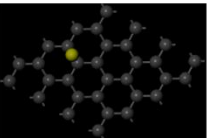
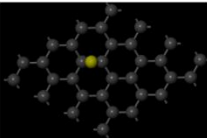
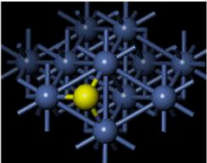
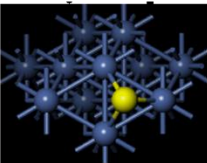
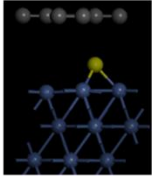
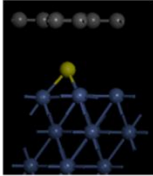


Figure 2.4. Schematic illustration of type A, B and C diffusion kinetic processes according to Harrison's classification.⁶⁹

Table. 2.1. DFT calculation of activation energy barrier for single carbon atom diffusion on each configuration according to the reaction pathway.⁶⁶

	Reaction pathway		Activation energy barrier
graphene sheet			0.239 eV
Ni (111) surface			0.492 eV
The interface between a graphene sheet and Ni (111) surface			0.514 eV

Chapter 3. Experimental Preparation

3.1 Materials preparation

Annealing of Cu foils, 1- μm -thick polycrystalline copper foils (99.97%, Good Fellow) cut to 1cm \times 1cm size. The Cu foils were immersed in acetic acid (99.5%, glacial, SAMCHUN chemical) at 50 $^{\circ}\text{C}$ for 20 min using the teflon zig, which was manufactured for treating 1- μm -thick Cu foils. Immediately after acetic acid treatment, the Cu foils were blown with an N₂ gun very carefully. We note that 1- μm -thick Cu foils can be easily bent, so special care was taken throughout the process. The prepared Cu foils were placed into an Ultra High Vacuum (UHV) chamber ($\sim 1 \times 10^{-10}$ Torr) and annealed at temperatures as high as 790 $^{\circ}\text{C}$ for between 20 and 260 minutes in ambient hydrogen (99.9999% purity) at a pressure of $\sim 10^{-6}$ Torr. Figure 3.1 shows that the annealing process was conducted on a SiO₂/Si substrate in an UHV chamber. In the UHV system, the substrate temperature was measured using a k-type thermocouple that was directly connected to the substrate susceptor before annealing experiments. After the annealing process, we obtained the Cu foils with a predominantly (111)-texture and $\sim 30\text{-}50$ μm sized grains with smooth surfaces.

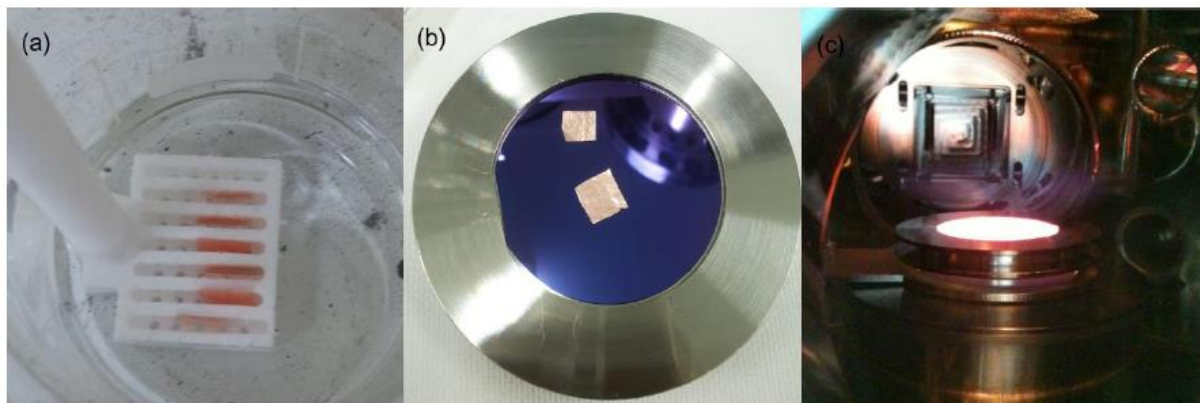


Figure 3.1. Annealing of Cu foils. (a) The 1- μm -thick Cu foils immersed in acetic acid using a Teflon zig, (b) the Cu foils on a 2-inch SiO₂/Si substrate, (c) annealing process of Cu/ SiO₂/Si on a susceptor at about 790 $^{\circ}\text{C}$ in an UHV chamber.

3.2 Experimental Procedure

Experimental procedure of synthesis of monolithic GO sheets via DAS. The annealed Cu foils were taken out from the UHV chamber below about 100°C. The DAS process is schematically described below as shown Figure 3.2. The annealed Cu foils were placed on a SiO₂/Si substrate in a molybdenum holding stage and solid C was supplied from graphite powder (Aldrich, product 496596) that fully covers the foil surface. The C-Cu-SiO₂/Si substrate diffusion couple was clamped at about 1 MPa pressure in a molybdenum holding stage. Finally, the completed diffusion couple with a Mo holding stage is shown in Figure 3.3.

The furnace was heated to the desired growth temperature up to 260 °C before loading the completed diffusion couple. (i) The furnace pressure was initially evacuated to a pressure of $\sim 10^{-3}$ Torr to repel the residual oxygen, (ii) a 4-inch quartz tube was filled with argon gas up to atmospheric pressure, (iii) the furnace was heated to the desired growth temperature. Next, the completed diffusion couple was rapidly transferred into a 4-inch quartz tube to maintain growth temperature under a flow of argon gas (1 L/min) and heated for 5 to 120 minutes. Following graphene framework growth, the completed diffusion couple was removed from the furnace and was then rapidly cooled from the growth temperature to room temperature, as shown in Figure 3.4.

After the cooling process, the Mo holding stage was separated and graphite powder was almost removed from the Cu foil surface by carefully shaking out the assembled Cu-SiO₂/Si couple with a tweezer, as shown in Figure 3.5. The inset image shows the cleaned sample, but some graphite flakes still remained at the top surface of the Cu foil. In order to make a perfectly clean surface, we used the hydrophobic characteristic of graphite by dipping it into D.I water. The assembled Cu-SiO₂/Si couple was immediately taken out from the D.I water and then it was dried by heating the assembled Cu-SiO₂/Si couple on a hot plate ($\sim 80^\circ\text{C}$) as shown in Figure 2.x.x

Transfer of DAS-graphene framework, We transferred the graphene frameworks grown on the reverse side of the Cu foil onto other substrates for further investigation using a poly(methyl methacrylate) (PMMA)-assisted method. Before spin coating of PMMA on the surface of graphene framework, the graphene/Cu foil assembly was carefully put on a wafer film (SM technology, dn-280) pasted on a spin head (Figure 3.7 (a)). The wafer film contained small holes at the four corners of a square ($\sim 1 \text{ cm}^2$) to disperse vacuum pressure ($< \sim 750 \text{ mmHg}$) throughout the assembly and so it was sustained without crumbling or wrinkling before spin coating (Figure 3.7 (b)). PMMA (M = 950,000, 4% in chlorobenzene) solution was deposited on the surface of graphene/Cu assembly by spin coating at 4000 rpm for 20 sec (Figure 3.8 (c)) and the PMMA/graphene/Cu assembly was then cured on a hot

plate at 180°C for 1 min. The PMMA/graphene/Cu assembly was etched in separated $(\text{NH}_3)_3\text{S}_2\text{O}_8$ (0.1M) solutions for 2, 5, 10 and 30 min in sequence, as shown in figure 3.7 (e-h). After etching the Cu foils over 60 min, the PMMA/graphene assembly was rinsed in DI water for 30 min. Subsequently, the assembly was transferred onto a SiO_2/Si substrate and dried on a hot plate. The PMMA/graphene/ SiO_2/Si assembly was exposed to acetone to remove the top PMMA layer, and then it was rinsed with IPA. Finally, graphene frameworks were blown with an N_2 gun.

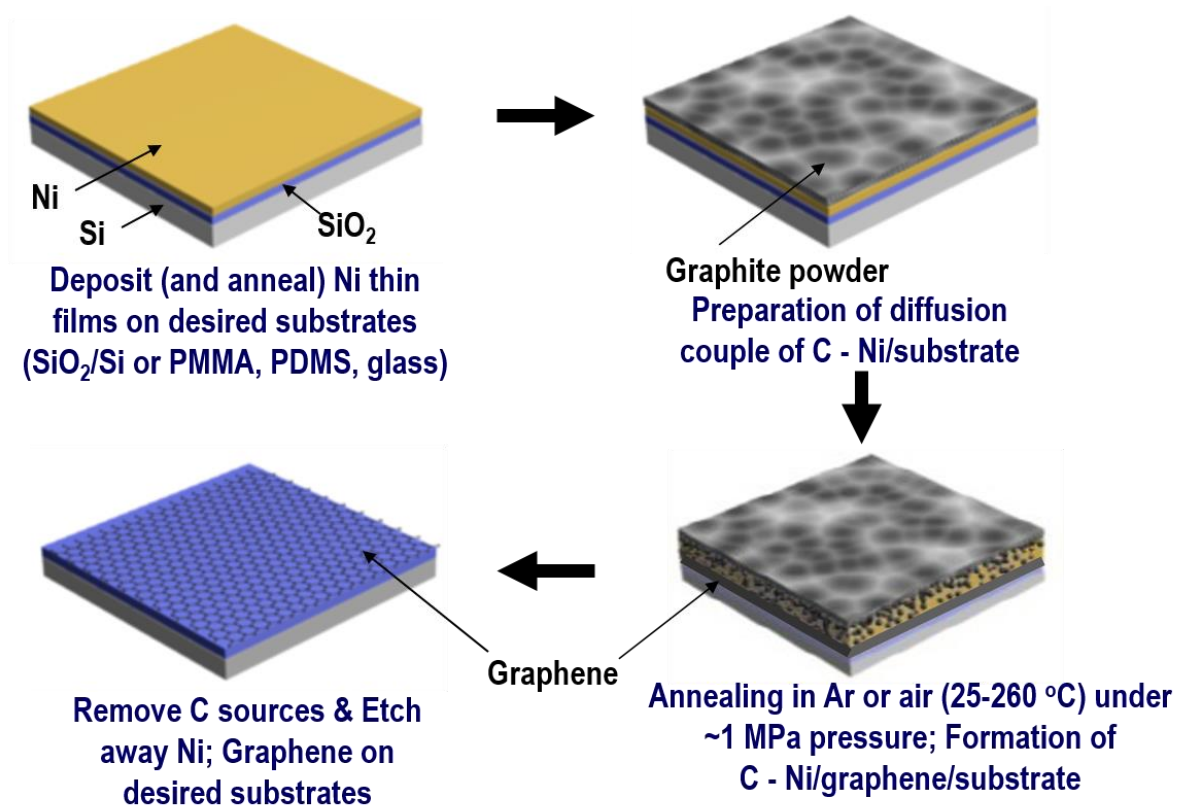


Figure 3.2. Schematic illustration of DAS process.⁶⁶

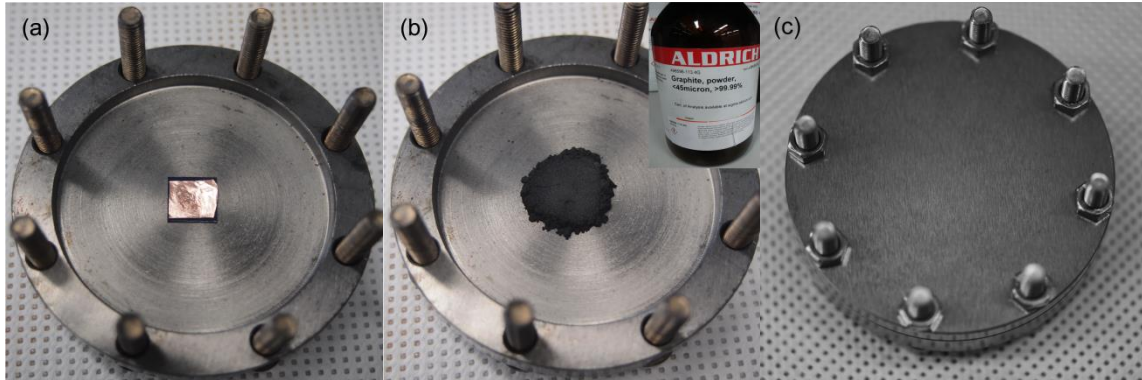


Figure 3.3. Preparation of C-Cu-SiO₂/Si substrate diffusion couple with a Mo holding stage. (a) The annealed Cu foil was prepared on a SiO₂/Si substrate (~1 cm²). (b) The annealed Cu foil was covered with graphite powder to fully cover the foil surface. (c) The C-Cu-SiO₂/Si substrate diffusion couple was clamped at a pressure of ~1MPa in a molybdenum holding stage to uniformly apply the pressure. The inset in (b) shows the product information of the graphite powder used in the DAS process.

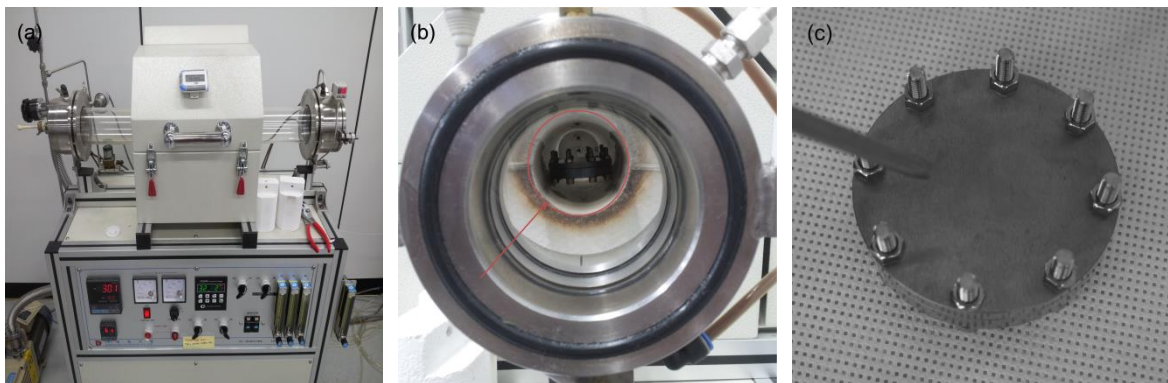


Figure 3.4. Photographs of the furnace-based DAS process of graphene frameworks. (a-b) The images show the stage in which the completed diffusion couple is loaded in a quartz tube. (c) The completed diffusion couple was rapidly cooled to room temperature with an N₂ gun.

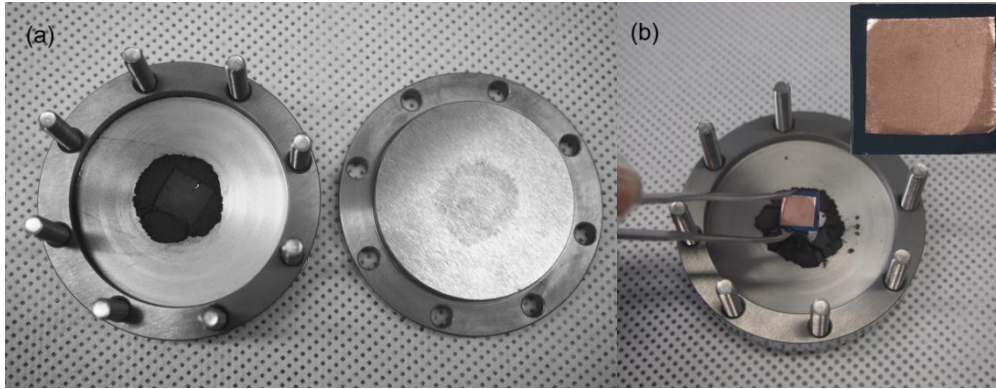


Figure 3.5. Removal of graphite powder from the Cu-SiO₂/Si substrate. (a) After the cooling process, the Mo holding stage was separated and (b) graphite powder was almost removed from the Cu foil surface by carefully shaking out the assembled Cu-SiO₂/Si couple with a tweezer. The inset shows the photograph of the cleaned Cu surface.

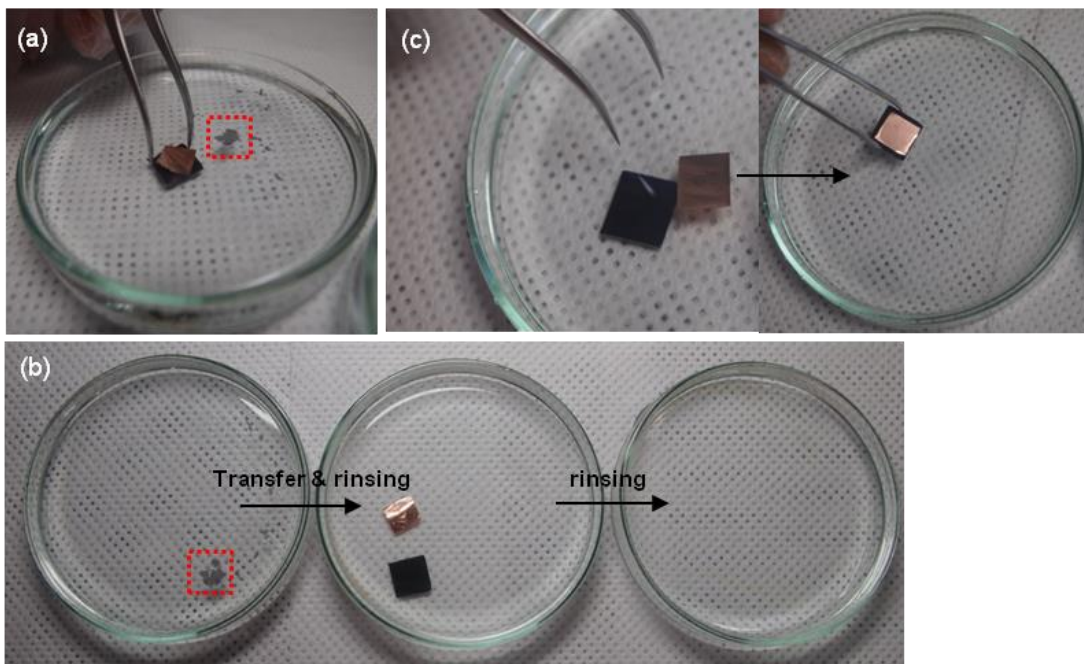


Figure 3.6. Photographs of the cleaning process of the Cu foil surface in D.I water after DAS process. (a) Removal of residual graphite powder by shaking out the assembled Cu-SiO₂/Si couple with a tweezer in D.I. water. The red dotted rectangle indicates the removed graphite powder from the Cu surface, (b) the cleaning process of the Cu foil is shown step by step and the D.I. water was put in separated petri-dishes, (c) introduction of a new a SiO₂/Si substrate in D.I. water to scoop up the cleaned Cu foil from the D.I. water.

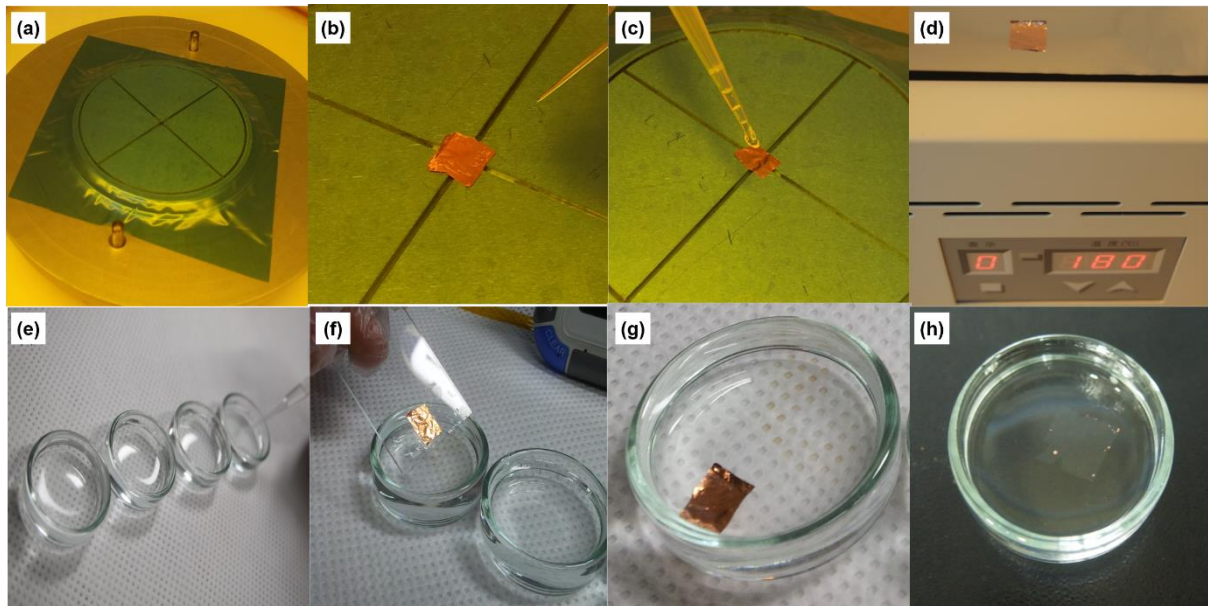


Figure 3.7. (a-d), The new design was devised for transferring DAS-graphene framework grown on the Cu foil onto other substrates. The 1- μm -thick Cu foil can be supported against vacuum pressure without crumbling or wrinkling. The PMMA/graphene/Cu assembly was made for transfer. (e-h), The process of etching DAS-graphene framework grown on a Cu foil is shown step by step. $(\text{NH}_3)_3\text{S}_2\text{O}_8$ (0.1M) solution was put in separated petri-dishes. The Cu foils were moved to other etchant by glass and etched away for (e) 2, (f) 5, (g) 10 and (h) 30 min. After etching the Cu foils over 60 min, we obtained Cu-free graphene framework.

3.3 Characterization

Atomic force microscopy. The surface morphologies of the as-received, annealed and GO-covered Cu foils were observed using an AFM (Veeco Multimode V) operating in tapping mode. The surface root-mean-square roughness of the samples was estimated from over 20 different regions per sample, with a scan size of 5 μm x 5 μm .

Raman spectroscopy and mapping. The presence of a highly ordered graphene framework was confirmed by Raman spectroscopy. Both the Raman spectra and maps were collected from a graphene framework that had been transferred onto a 300-nm-thick SiO_2 layer on Si. The Raman spectroscopy and mapping were carried out on a WiTec alpha 300R M-Raman system with a 532nm excitation wavelength (2.33 eV); the laser spot had a dimension of ~ 640 nm for a x 50 objective lens with numerical aperture of 0.5 and the laser power was $\sim 2\text{mW}$. The Raman spectra were analysed and Raman images were constructed using a computer-controlled x-y translation stage with a raster scan. A spectroscopic image was created by measuring the Raman spectrum of each individual pixel with a 70 μm x 70 μm step size using WiTec Project software. The Raman data presented in this thesis, such as IG/I2D and the FWHM values of the G and 2D bands, are arithmetical averages of values that were measured at more than 30 different points per sample.

UV-vis spectroscopy. The optical transmittance of a graphene framework that was transferred onto a quartz plate was measured using UV-Vis spectroscopy (Varian, Cary 5000 model) between 200 and 800 nm in dual-beam mode. The optical band gap, as determined from the plot of $\sqrt{\varepsilon} / \lambda$ versus $1/\lambda$ following Tauc's equation⁷², is an arithmetic average of values that were measured for five different samples grown under the same condition.

X-ray photoelectron spectroscopy (XPS). The presence and chemical states of atomic impurities in the graphene framework were investigated using XPS. The XPS studies were conducted on a K-alpha spectrometer (Thermo Fisher) using aluminum $K\alpha$ non-monochromatic X-ray excitation at a power of 72 W, with an analysis area diameter of ~ 0.4 mm and a pass energy of 50 eV for the electron analysis. The base pressure of the analysis chamber was below $\sim 1 \times 10^{-9}$ mbar. The O/C compositions in the graphene frameworks were determined by dividing the individual peak areas in an XPS wide-scan survey spectrum, after appropriate background subtraction, by their respective atomic sensitivity factor.

Fourier transform infrared spectroscopy (FT-IR). To appreciate the special oxygen configuration in the graphene framework, the reflectance FT-IR spectrum of a six-layer stacked graphene framework that was transferred onto atomically-flat, clean surface of Au film deposited on SiO_2/Si was measured using the Agilent Cary 670 FTIR spectrometer interfaced to a SeagullTM accessory set for reflection

analysis (with an incidence angle of 84°), a mercury cadmium telluride (MCT) detector and a Ge on KBr beam splitter. To overcome the low throughput in incidence angle mode, six different samples grown under the same condition were mechanically stacked onto Au surface.

Time-of-flight secondary ion mass spectroscopy (TOF-SIMS). To compare the elemental compositions of C and O atoms in the as-received and annealed Cu foils before and after the DAS process, TOF-SIMS measurements were carried out on an ION-TOF (Münster, Germany) instrument. A pulsed 25 keV Bi^+ primary ion source (average current: 1.0 pA; pulse width: 12.1 ns; repetition rate 100 μHz) was employed over a $500 \mu\text{m} \times 500 \mu\text{m}$ area at an operating pressure of $\sim 1 \times 10^{-9}$ mbar. Negative-ion profiles were recorded and analyzed; this technique is ideally suited to searching for possible correlations related to the ejected secondary ion polarity of C and O atoms.

Cross-sectional TEM of Cu foils and GO/Cu-foils; elemental C maps on Cu foils. The TEM samples were prepared as follows: The two surfaces of Cu foil were glued together with a Si substrate to support the flexible 1- μm -thick Cu foils. This Si-sandwiched Cu foil was sliced into 2-mm-thick pieces by using a low-speed diamond saw. After being polished to a residual thickness of $\sim 10 \mu\text{m}$, the sample was finally milled by an Ar^+ ion-beam (PIPS, Gatan Inc.). Substantial heating of the TEM foils and, consequently, the introduction of artifacts were avoided by means of double-sided ion-beam etching at small angles (less than 6°) and low etching energies (acceleration voltage 2.5 kV; beam current less than 8 μA) with liquid-nitrogen cooling ($\sim 150 \text{K}$). For energy-filtering TEM imaging, a Tecnai F20 microscope (installed at Seoul National University) that was operating at 200 kV and equipped with a Gatan image filter (GIF) system was used. The Digital Micrograph software (Gatan Inc.) was employed for the image processing and analysis.

High resolution, plan-view TEM of the GO sheets. Using a direct transfer method⁷³, the GO sheets were transferred onto Quantifoil TEM grids. However, after the transfer process onto a TEM grid, we frequently observed the formation of ~ 10 - 100 -nm-sized holes in the GO sheets. High-resolution TEM images and the corresponding FFT patterns of the GO sheets were obtained on an FEI Titan cube G2 60-300 at UNIST, which was equipped with an image-aberration corrector and monochromator. The microscope was operated at an accelerating voltage of 80 kV to decrease beam damage to the GO sheets.

FET device fabrication and electrical characterizations of the GO sheets. Bottom-gated FET devices were fabricated by transferring the GO sheets onto p-Si substrates with 300 nm thermal oxide. p-Si was used as the gate electrode. FET devices with a channel length of 5 μm and channel widths of 200 μm (O/C ~ 0.8) and 20 μm (O/C ~ 0.3) were fabricated by conventional photolithography and O_2 plasma etching process. We employed a larger channel width in the sample with O/C composition of 0.80 to make a clear distinction between source-drain current values owing to a lower conductivity of the sample. Source-drain electrodes (Cr/Au: 10 nm/60 nm) were deposited by using an e-beam

evaporator. The transport characteristics measurements were conducted with a cryogenic probe station (Lake Shore, CRX-4K) at temperatures from 20 to 300 K. Before measurements, we put the samples into the vacuum chamber of $\sim 1 \times 10^{-6}$ Torr for 24 hours to reduce the adsorbed impurity molecules, such as water vapors, on the GO sheets and then cooled down the sample temperature. From the plot of the source-drain current as a function of gate voltage from -80 V to 80 V, we extracted carrier mobility values from the slope. At each temperature, the conductivity values were calculated by using the average thickness of 1 nm in our GO sheets, which was obtained from our AFM studies.

Chapter 4. Physically Synthesized GO Sheets

4.1 Introduction

Graphene oxide (GO) is a material of great interest for its potential applications in nanoelectronics⁷⁴⁻⁷⁵, sensors⁷⁶, energy storage devices⁷⁷ and light-emitting devices⁷⁸⁻⁷⁹. GO is an atomically thin sheet consisting of graphite oxide that is consisted with oxygen (O)-containing functional groups and it contains a mixture of sp²- and sp³-hybridized carbon (C) atoms bearing hydroxyl (C-OH) and epoxide (C-O-C) functional groups on the basal plane and carbonyl (C=O) and carboxyl (COOH) groups at the sheet edges⁷⁸. Graphene in itself does not have a native oxide and harsh chemical treatments with the use of strong acid are necessary to produce GO films⁸⁰. GO is typically synthesized by solution-based chemical treatments from micrometre-scale graphite flakes and properties of GO-based devices depend on the preparation process used, which can yield a range of network morphologies of GO flakes⁸¹⁻⁸⁴. Chemically-derived GO exhibit electrically insulating and should be reduced using chemical and/or thermal treatment to make it electrically active^{85,86}. Although the chemical routes might be preferred for mass-production manufacturing, they can be less effective to offer paths towards precise device assembly, owing to the enormous interlayer van der Waals forces and hydrophilic property of GO⁸⁴. To date, the synthesis of monolithic GO sheets has not been achieved on any surface over a large area with continuous films, which limits their usefulness in device applications based on graphene and its derivatives.

In this thesis, we successfully demonstrate that a monolithic form of GO sheets can be physically synthesized on a copper (Cu) surface at low temperatures ($\leq 260^\circ\text{C}$), with controllable oxygen-to-carbon (O/C) composition. In our method, we synthesized a graphene framework on the reverse side of a Cu foil at a Cu/substrate interface by exploiting the solid-state diffusion of C atoms across a diffusion couple composed of a C-Cu/substrate. A combined theoretical and experimental study shows that the Cu foil provides an effective pathway for C diffusion, trapping the O species dissolved in Cu and enabling the formation of monolithic GO sheets on its surface after an incubation time. In contrast to chemically-derived GO sheets⁸¹⁻⁸⁴, the as-synthesized GO sheets exhibited electrically active and the O/C composition in GO can be tuned during synthesis process by controlling the resolved O content in the Cu foil prior to the solid-state diffusion process. The resulting GO sheets exhibited controllable bandgap energy by varying the O/C composition, making them potentially useful for flexible and transparent semiconducting applications. The GO films exhibited the ambipolar transfer characteristics in bottom-gate field-effect transistor (FET) architectures and the electronic properties were found to correlate closely with the bandgap energy. These results suggest that monolithic, two-dimensional

chemically-modified C sheets with controllable composition can be prepared at low temperatures, which is highly desirable for graphene-based device production.

4.2 Synthesis of monolithic GO sheets on Cu foil via DAS.

We successfully demonstrated a solution-free, physical synthesis method of monolithic chemically derived C sheets on reverse side of Cu surfaces that relied on a DAS approach⁸⁷. The DAS process is described as shown Figure 4.1. Initially, 1- μm -thick polycrystalline Cu foils were used; these Cu foils contained strong rolling features with irregular grain structures that were produced during the manufacturing Process. In the annealing step, the Cu foils were annealed at ~ 790 °C in ambient hydrogen to yield a strong (111) texture with aligned grain boundaries (GBs) normal to the foil surface and induced 30–50- μm -sized grains with smooth surfaces. Variations in the annealing time allowed the O content in the Cu foil to be tuned. The morphology, crystallinity and distribution of atomic impurities in the Cu foils before and after the annealing process are presented in Figure 4.2. The annealed Cu foils were physically attached onto a SiO_2/Si substrate and were covered with graphite powder that used as a solid C source. The C–Cu–substrate assembly, which was clamped at a pressure of ~ 1 MPa, was then placed in a quartz tube under a flow of argon gas at atmospheric pressure and heated up to 260 °C for 5–120 min. At that temperature, dissociated carbon atoms began to diffuse along the GBs of the foil through the Cu while trapping the O species dissolved in the Cu. The substrate temperature was estimated using a k-type thermocouple that was directly connected to the molybdenum sample holder; accuracy was ± 10 °C. As the diffusing C and O atoms reached the reverse side of the Cu foil, they created a thin film of GO over the incubation time. The pressure promotes the movement of C through the Cu foil. After the solid C source was removed, the samples were cleaned and the Cu foils were detached from the substrate. It is worth noting that we always observed the formation of a monolithic graphene framework on the reverse side of the Cu foils, rather than on the surface of the SiO_2/Si substrate. We note that 1- μm -thick Cu foil provides the optimum efficiency process for the DAS process among commercially available Cu foils with thicknesses ranging from 0.5 to 50 μm . Foils that are thinner than 1 μm exhibit shorter durations with easier control over the DAS process, although there is a trade-off in the ease of sample handling. Further experimental details are given in below.

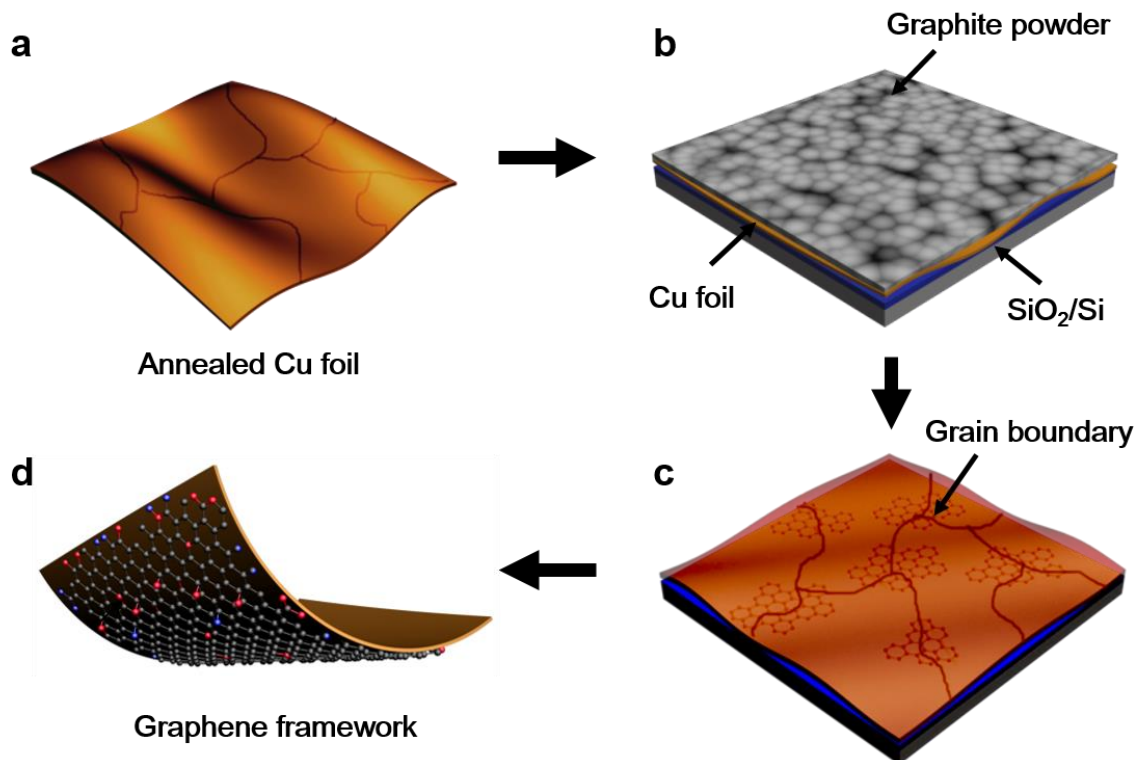


Figure 4.1. Schematic illustration of the modified DAS process for synthesizing monolithic GO sheets on the reverse side of a Cu foil. This process includes the elementary step in the DAS process: the annealing of the Cu foil; the physical attachment of the Cu foil onto the substrate and preparation of the C-Cu-substrate diffusion couple; heating of the assembly in ambient argon (below 260 °C) and the formation of monolithic GO sheets at the Cu/substrate interface, and the detachment of the Cu foils after removal of the solid C sources from the foil surface.

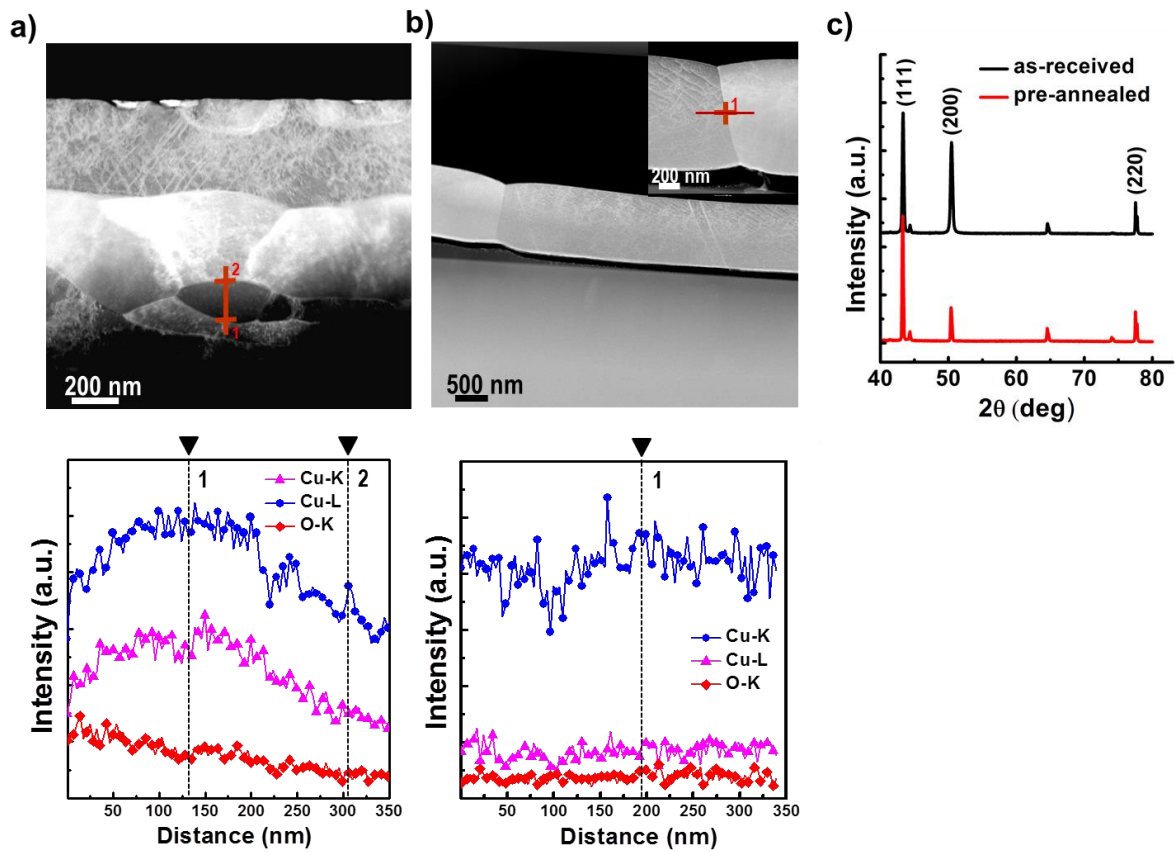


Figure 4.2. Cross-sectional STEM images and corresponding energy-dispersive spectroscopy (EDS) line profiles of (a) an as-received and (b) an annealed 1- μm -thick Cu foil at about 790°C in ambient hydrogen, respectively. Note that the O distribution within an annealed Cu foil is quite uniform from EDS after the annealing process. (c) XRD patterns of 1- μm -thick Cu foil before and after the annealing process.

4.3 Formation of a Graphene Framework on Cu foil

We observed the formation of a monolithic graphene framework on the reverse side of the Cu foil via DAS method. Figure 4.3. exhibits typical optical microscopy images of the annealed, bare Cu foils and the as-synthesized graphene frameworks on the reverse side of the Cu foils before and after oxidation in air at 200 °C for 120 min. The resulting graphene framework was indicated highly resistant property to oxidation, thus indicating the presence of a monolithic form of C sheets on the Cu foil⁸⁸. The hexagonal configuration of the graphene framework in the samples was evidenced by plan-view transmission electron microscopy.

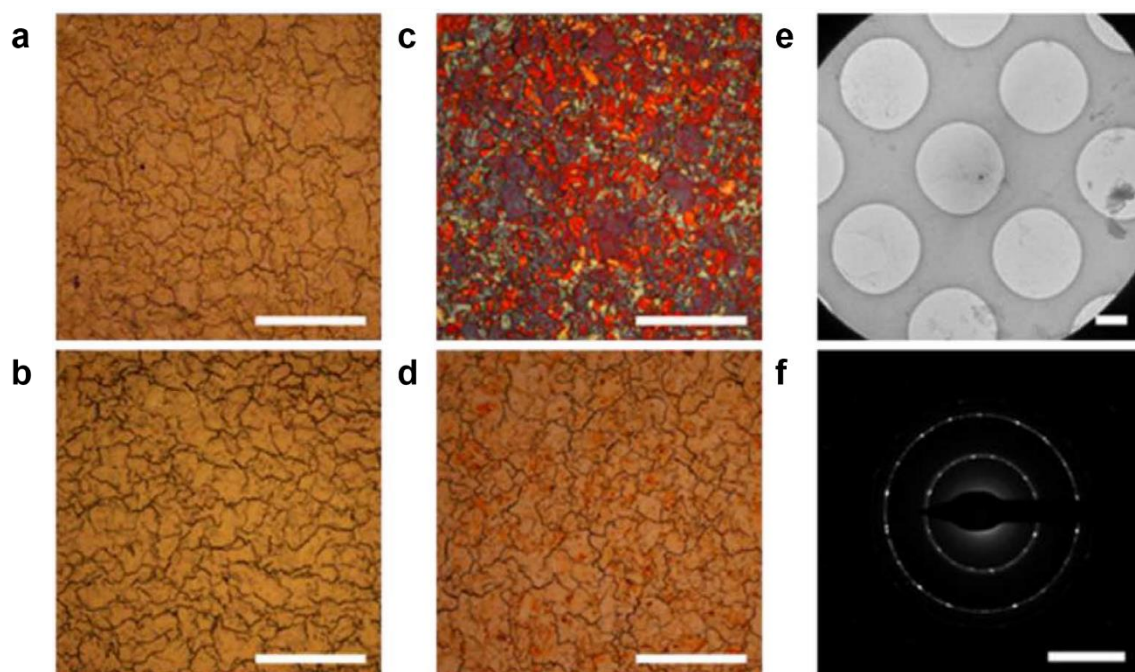


Figure 4.3. Optical images of annealed Cu foils (a,c) and GO-covered Cu foils (b,d) before (a,c) and after (b,e) oxidation in air at 200 °C for 120 min (scale bars, 150 μm). (e,f) A bright-field TEM image of the GO sheet (scale bar, 1 μm) (e) and its corresponding selected area electron diffraction pattern (scale bar, 5 nm^{-1}). (f) Most micro-crystallites were polycrystalline.

4.4 Presence of oxygen groups on the graphene framework.

Figure 4.4. exhibits representative Raman spectra of samples that were obtained at a temperature of 240°C for 60 to 120 minutes and then transferred onto SiO₂/Si(100). These spectra indicate the significant presence of foreign species in the graphene framework. The spectra for all of the samples exhibit three primary features: a D band at ~1,348 cm⁻¹, a G band at ~1,592 cm⁻¹ and a 2D band at ~2,687 cm⁻¹, which are all typical peak positions for graphene^{66,88-93}. The hexagonal configuration of the graphene framework in the samples was also evidenced by plan-view transmission electron microscopy (TEM, Figure 4.3). However, the Raman spectra of the samples consistently show an intense D band ($I_D/I_G \geq 1.0$), related to domain boundaries, impurities, and growth-nucleation sites⁹⁴⁻⁹⁷. The associated G/2D band and the full-width at half-maximum (FWHM) of the 2D band maps, as shown in Figure 4.4d, represent the uniformity of the samples over a large area (70 μm × 70 μm). The samples primarily consisted of a single-layer graphene framework (as identified by $I_G/I_{2D} \leq 0.4$ and a FWHM of the 2D band of ~38 cm⁻¹) and bi- and multi-layered regions that resembled ridge structures⁶⁶ resemble to GBs in the annealed Cu foils. The graphene framework seems to be predominantly composed of a single-layer when analyzed using Raman spectra and maps. Interestingly, the formation of a graphene framework on Cu appears to have been self-limited; growth that proceeded for 120 minutes yielded a single-layer structure similar to that obtained following 60-minute growth, based on the Raman structure. The optical transmittance of the samples that were grown for 120 minutes decreased by 2.3~2.5 % as shown in Figure 4.5. Thus implying that the average thickness of these samples corresponded approximately to that of a monolayer⁹⁸.

The following Tauc's equation⁹⁹ which was normally used to determine the optical band gap E_g .⁴⁵⁻⁴⁸

$$\omega^2 \epsilon = (h\omega - E_g)^2 \quad (4.1)$$

Where, ϵ is the optical absorbance, $\omega = 2\pi/\lambda$ is the angular frequency of the incident radiation (λ is the wavelength). Therefore, the plot of $\sqrt{\epsilon/\lambda}$ versus $1/\lambda$ is a straight line. The intersection point with the x-axis is $1/\lambda_g$ (λ_g is the gap wavelength). The optical band gap can be calculated based on $E_g = hc/\lambda_g$.

Interestingly, In contrast to pristine graphene that has no bandgap⁸⁹⁻⁹¹, however, the optical bandgaps of the graphene frameworks that were transferred onto quartz were measured to be ~2.21 (±0.07) eV from the plot of $\sqrt{\epsilon/\lambda}$ versus $1/\lambda$ of the data acquired from monolithic graphene framework that were grown for 120 minutes, based on UV-Vis spectroscopy as shown in Figure 4.5, indicating the presence of foreign species in the graphene framework^{91,92}.

Furthermore, Figure 4.6 shows atomic force microscopy measurement results that the surface RMS roughness of the graphene frameworks that were transferred onto SiO₂/Si(100) was 2- to 3-times larger than that of the pristine graphene on SiO₂/Si(100), which could be attributed to the random covalent attachment of foreign species onto the surface of the graphene framework¹⁰⁰.

Therefore we further investigated the presence and chemical states of foreign species in the samples using X-ray photoelectron spectroscopy (XPS) and Fourier transform-infrared (FT-IR) spectroscopy. Typical XPS wide-scan survey spectrum of the samples shows substantial C 1s and O 1s peaks at ~ 284.4 and 530.4 eV, respectively as shown in Figure 4.7.

A high-resolution (HR) C1s line-scan spectrum represents a dominant peak at ~ 284.4 eV, which corresponds to the graphite-like sp²- hybridized C, thus indicating that most of the C atoms formed a 2D honeycomb backbone structure. Two additional peaks are located at ~ 285.3 and 288.0 eV, which could be attributed to oxygen functional groups such as C-O-C (epoxide) or C-OH (hydroxyl) groups, and C=O (carbonyl) species⁸⁰⁻⁸³. The detailed chemical states of the oxygen functionalities on the samples can be witnessed by a HR O1s line-scan spectrum as shown in Figure 4.8. Consequently, Grazing-angle reflectance FT-IR spectra of the samples further support the XPS results that there exist various oxygen functionalities in the graphene framework including the vibration modes of hydroxyl, epoxide, carboxyl, carbonyl groups and sp²-hybridized C=C (in-plane vibrations) (Figure 4.8c). On the basis of structural and optical characterizations, we concluded that the as-synthesized graphene frameworks were highly-ordered, predominantly monolayer GO sheets.

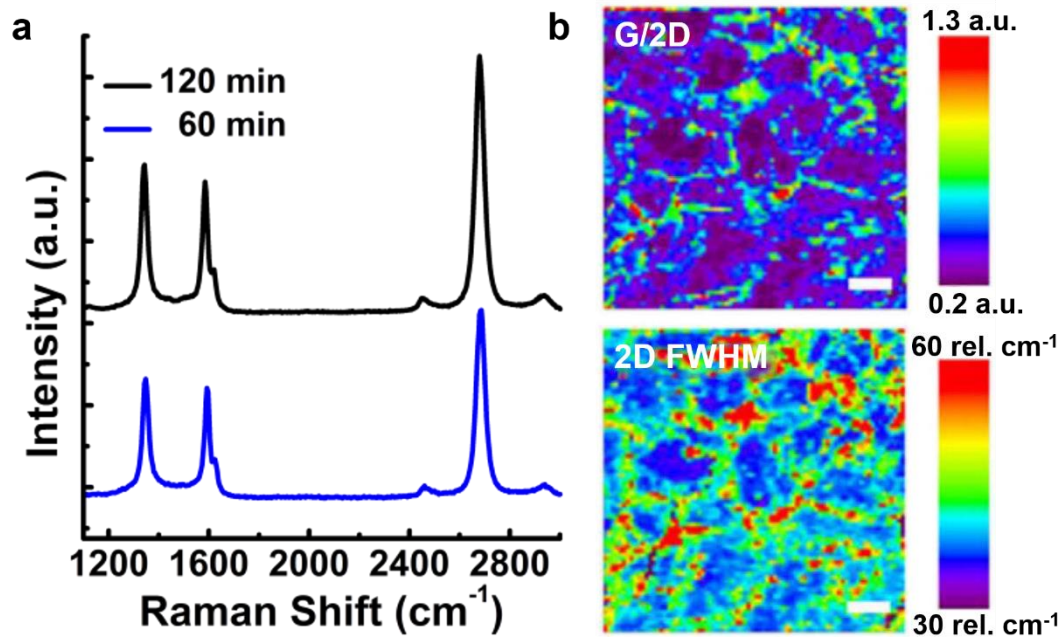


Figure 4.4. (a) Representative Raman spectra of GO that was grown on a Cu surface at 240 °C for 60 min (bottom) and 120 min (top), and then transferred onto SiO₂ (300 nm)/Si. (b) Raman map of the G/2D bands (top) and the FWHM of the 2D band (bottom) of GO that was grown on Cu at 240 °C for 60 min and then transferred onto SiO₂ (300 nm)/Si (scale bars, 10 μm).

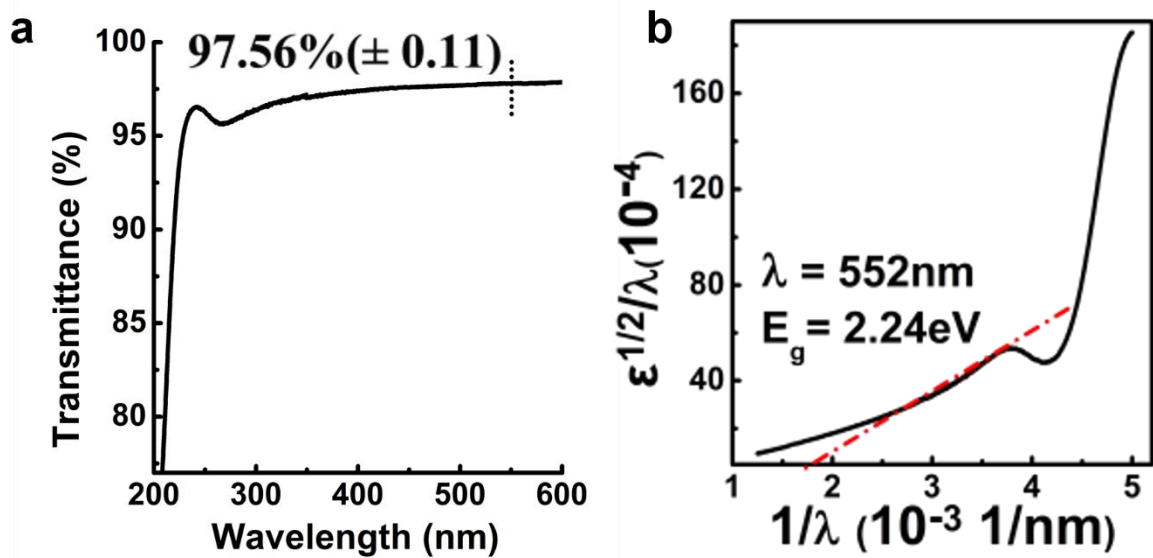


Figure 4.5. (a) Optical transmittance of GO that was grown on Cu at 240 °C for 60 min and then transferred onto SiO₂ (300 nm)/Si (scale bars, 10 μm). (b) a plot of $\sqrt{\epsilon} / \lambda$ versus $1/\lambda$ to determine the optical bandgap of the GO sheet.

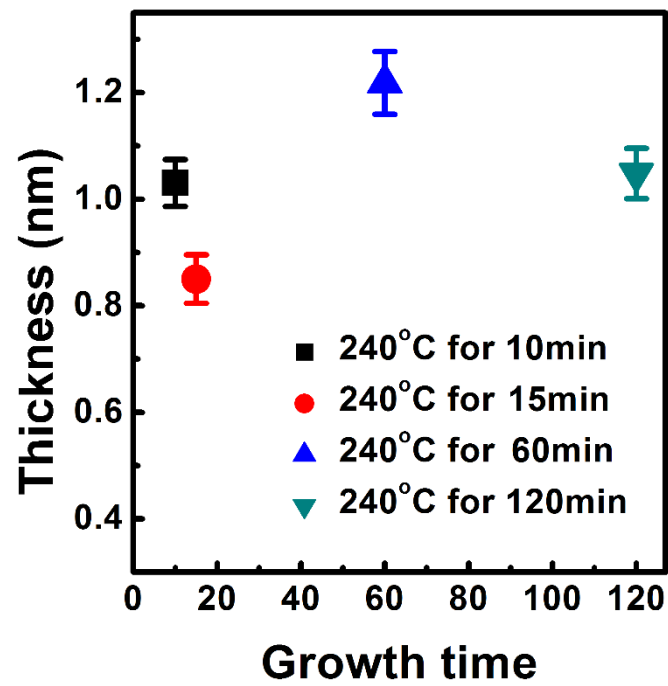


Figure 4.6. The thickness of GO framework according to growth time from atomic force microscopy (AFM) measurements.

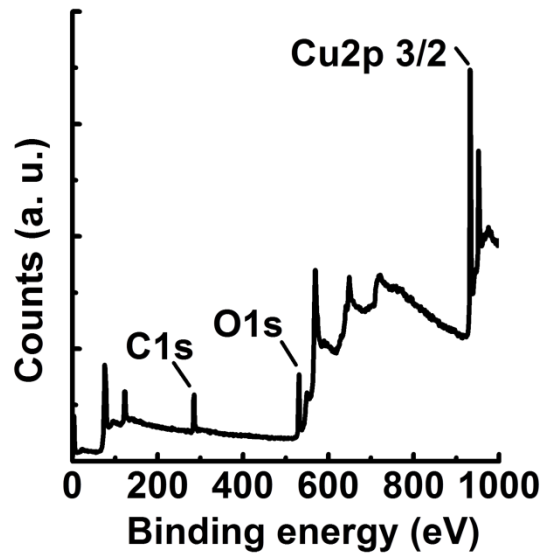


Figure 4.7. XPS wide-scan survey spectrum of the GO sample grown at $T = 240\text{ }^{\circ}\text{C}$ for $t = 120\text{ min}$. XPS spectra show the presence of significant numbers of oxygens in the resulting graphene framework.

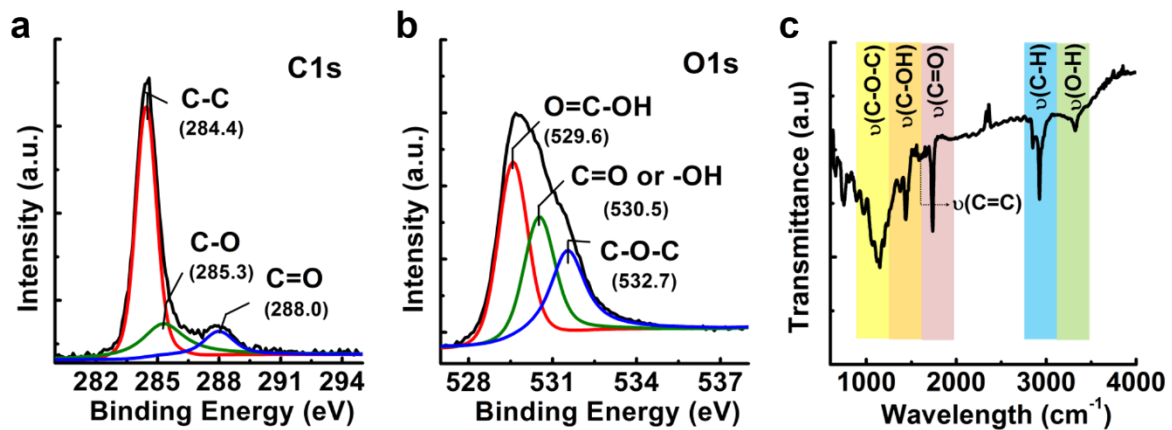


Figure 4.8. High resolution XPS C 1s (a) and O 1s (b) line scans of GO that was grown on Cu at $240\text{ }^{\circ}\text{C}$ for 120 min. (c) Grazing-angle FT-IR spectrum of a six-layer-stacked GO that was grown on Cu at $240\text{ }^{\circ}\text{C}$ for 120 min and then transferred onto an atomically flat, clean surface of Au film deposited on SiO_2/Si substrate.

4.5 Atomic Structure of The GO Sheets.

We investigated a closer examination of the structure of the GO sheets. Figure 4.9 exhibits a typical high-resolution TEM (HR-TEM) image that was obtained using aberration-corrected instruments; the highly graphitic nature of our GO samples was in striking contrast to the structure of chemically-synthesized GO^{81,101}. The structure of our GO sheets consisted of a highly-ordered honeycomb lattice with a grain size of about 10 nm, consistent with the value predicted from the Tuinstra and Koenign (TK) relation below¹⁰².

$$\frac{I(D)}{I(G)} = \frac{C(\lambda)}{L_a} \quad (4.2)$$

Where $C(\lambda)$ is the constant related to the excitation wavelength used in Raman, and L_a is the crystallite size in graphite. We note that the TK relation is only valid when the six-fold member rings are already present.

The graphitic grain boundaries were mis-tilted along the azimuthal direction with respect to each other, and the interiors of the graphitic grains were found to be highly crystalline and significantly combined with oxygen functionalities. Four typical fast Fourier transforms (FFTs) of the HR-TEM image are illustrated in Figure 4.9., which together confirm the graphitic nature of the discrete grains. The presence of a significant amount of oxygen in our samples was further confirmed by electron energy loss spectroscopy in TEM (EELS) (Figure 4.9c). The large graphitic area in the GO surface clearly supports our hypothesis that the parent GO consists of a honeycomb lattice that is decorated with oxygenated functionalities, as confirmed by XPS and FT-IR measurements. Bi- and multi-layer (≤ 4 layers) regions, which could be attributed to the ridge structures⁶⁶, were frequently detected by HR-TEM. Both regions displayed distinct Moiré patterns that were caused by the stacking of individual hexagonal graphitic layers with different orientations¹⁰³.

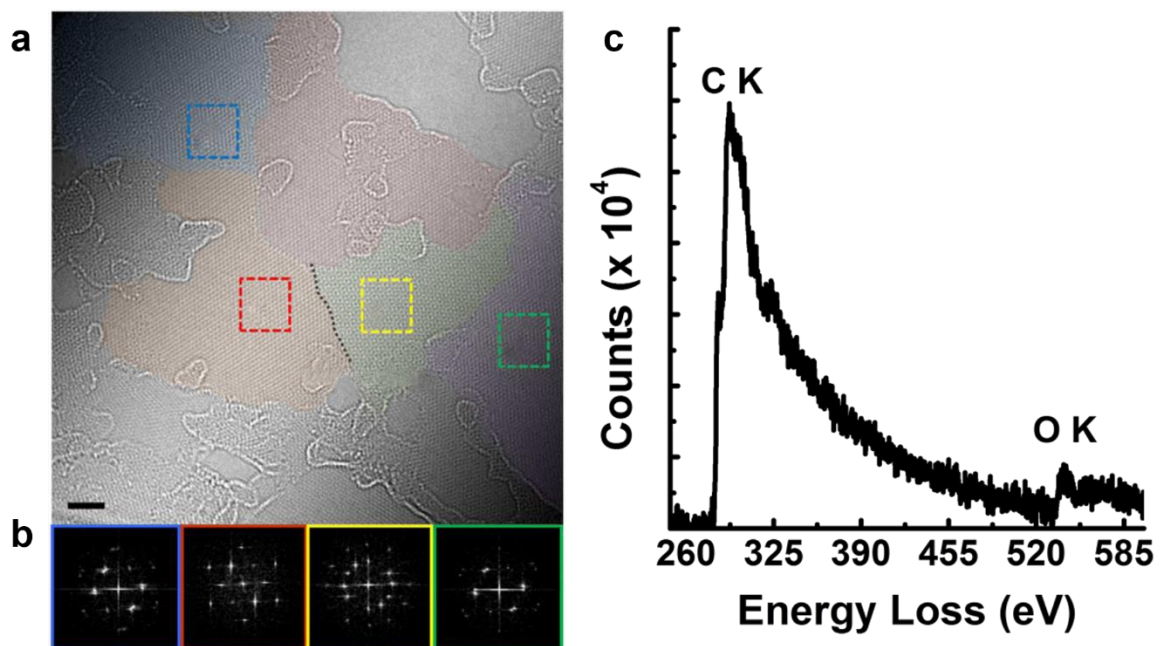


Figure 4.9. Investigation of atomic structure of a GO sheet. (a) Atomic resolution, plan-view TEM image of a GO sheet that was grown on a Cu surface at 240 °C for 120 min and then transferred onto a TEM grid. The colour scheme in discrete grains in TEM images represent the different crystalline structures of the GO grains. Holes are observed after the transfer process of the GO sheet onto a TEM grid (scale bar, 2 nm). (b) FFT patterns of the regions specified in (a). (c) electron energy loss spectroscopy of the GO sample grown at T = 240 °C for t = 120 min, showing the presence of significant number of oxygens in the resulting graphene framework.

Chapter 5. Growth Mechanism

5.1 Existence an Incubation Time in GO Synthesis

We are able to grow GO sheets for various periods under isothermal conditions. For growth times of less than 60 minutes at 240 °C, the Raman spectra indicate that the as-synthesized films contained a mixture of disordered and graphitic C areas, and that the relative surface coverage between disordered and graphitic C showed a critical dependence on the growth time, as shown in Figure 5.1. The resulting GO sheets were predominantly a disordered C layer with more than 95% surface coverage after 5 minutes of growth (Figure 5.1b). However, the surface coverage of the graphitic C layer increased linearly from about 30 to 100 % as growth time increased from 5 to 60 minutes, thus revealing the existence of an incubation time for graphitic C growth on Cu at low temperatures.

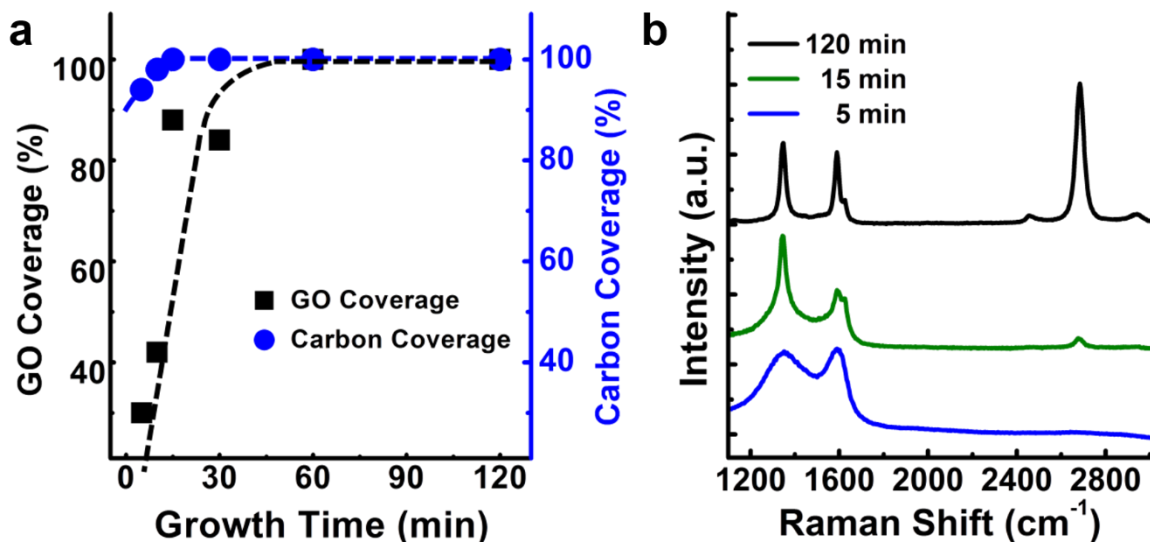


Figure 5.1. Growth tendency of a monolithic GO sheet on a Cu surface with various incubation times. (a) Plot of GO coverage (black squares) and C-segment coverage (blue circles) on a Cu surface as a function of growth time at 240 °C based on the Raman structure. (b) Comparison of the Raman spectra of GO sheets that were grown on Cu at 240 °C for 5 min (blue), 15 min (green) and 120 min (black), and then transferred onto a SiO₂ (300 nm)/Si substrate.

5.2 DFT Calculation of Transition State Energy of Carbon and Oxygen adatoms on Cu Foils.

We investigated the spin-polarized density functional theory (DFT)^{70,71} calculations to investigate growth mechanism and origin of the C- and O- atoms during diffusion processes that are contributed to the formation of GO on the reverse side of Cu foils. We calculated the transitional state (TS) energy of a monomer, dimer and trimer diffusion of C- and O- adatoms on both Cu (111) and Cu (100) surfaces. The framework of TS energy calculation for atomic and molecular diffusion was based on [66] and [104]. The calculations were conducted by using the CASTEP module in Materials Studio 6.1 which provides various modeling and simulation environment for atomic and molecular structure determination, property prediction, or simulation method in material science and chemistry. The CASTEP is a full-featured materials modeling code based on a first-principles quantum mechanical description of electrons and nuclei of atoms and molecules. It uses the robust methods of a plan wave basis set and pseudopotentials. The ultrasoft pseudopotentials¹⁰⁵ and the generalized gradient approximation were used with the exchange-correlation functional of Perdew-Burke-Emzerhof¹⁰⁶. Monkhost-Pack¹⁰⁷ a k-point mesh was $3 \times 3 \times 1$, which was used to test the Brillouine zone in the reciprocal space and the fine accuracy option was adapted for all calculations. Five layers of atomic plane filled with Cu atoms were used to simulate the Cu (111) and Cu (100) surfaces.

Figure 5.2 exhibits the typical atomic structure model which was constructed for atomic and molecular diffusion on Cu consisted of 32 atoms with periodic boundary conditions along the in-plane directions. The lattice constant of atomic structure is 3.61 \AA in both Cu (111) and Cu (100). To obtain TS energy diagram, we ran the calculation by CASTEP with a single linear synchronous transit, followed by repeated conjugate gradient minimizations and quadratic synchronous transit maximization until a transition state had been located. Prior to the TS search calculation, all models had relaxation to have most stable state.

Figure 5.3 shows the diagram of calculated TS energy of atomic or molecular diffusion on Cu (111) surface: C monomer, C dimer, O monomer, O dimer, and C-O molecules. From Figure 5.3 (a), it is seen that the calculated barrier energy of C monomer diffusion on the Cu (111) surface is 0.223 eV, while that of C dimer is 0.454 eV. For O diffusion, the barrier energies of minimum diffusion pathway for an O monomer as well as O dimer on Cu (111) are 0.295 eV and 0.485 eV, respectively, as shown in Figure 5.3 (b). In case of both CO and C₂O molecular diffusion on Cu (111) surface, the calculated barrier energies are 0.105 eV and 0.633 eV, respectively, as represented in Figure 5.3 (c).

Same calculation was repeated for Cu (100) surface, and Figure 5.4 represents the diagram of calculated TS energy of atomic or molecular diffusion on Cu(100) surface. As shown in Figure 5.4, the calculated barrier energies of diffusion are 2.118 eV and 0.883 eV for C monomer and C dimer,

respectively. From Figure 5.4 (b), it is known that the calculated barrier energy of an O monomer diffusion on Cu (100) surface is 0.940 eV, while that of O dimer is 1.121 eV. As indicated in Figure 5.4, the calculated barrier energies of a CO and a C₂O molecule diffusion on Cu (100) surface are 0.188 eV and 0.595 eV, respectively.

All results of calculation are summarized in Table 5.1. The result of calculation performed in this study shows the different diffusion behavior of between C and O on the Cu (111) as well as Cu (100) surfaces. Comparing the diffusion behavior of C and O on Cu (111) surface, the barrier energy of C diffusion increases as the diffusional species changes from monomer (0.223 eV) to dimer (0.454 eV), also O shows the increase in the barrier energy of diffusion when it changes from monomer (0.295 eV) to dimer (0.485 eV).

In case of diffusion on Cu (100), the results of C show the trend to oppose to that of Cu (111). That is, the barrier energy of C diffusion decreases as the diffusional species changes from monomer (2.118 eV) to dimer (0.883 eV). But O shows increase in the barrier energy of diffusion when it changes from monomer (0.940 eV) to dimer (1.121 eV) as same with that of Cu (111).

In all cases, however, the lowest barrier energy of diffusion can be achieved when the C-O molecule diffuses on Cu surface irrespective of crystallographic plane, compared to those of C and O, i.e., the barrier energies of diffusion of C-O molecule are 0.105 eV on the Cu (111), and 0.188 eV on the Cu(100), respectively.

To examine the diffusion of C-containing precursors reaching the reverse side of the Cu foil, we have calculated the tracer diffusion coefficients (D_t) of both C monomer and C-O molecule along the Cu (111) surface. The hopping rates of C monomer and C-O molecule can be found by the Arrhenius equation $\Gamma = \Gamma_0 \exp(-E_b/kT)$, which results in room-temperature hopping rates of about 1.70×10^9 and $1.68 \times 10^{11} \text{ s}^{-1}$, respectively with an attempt frequency of $\Gamma_0 = 1.0 \times 10^{13} \text{ Hz}$. In addition, the tracer diffusion coefficients of C monomer and C-O molecule can be expressed in terms of the hopping rate Γ and the mean square jump length $\langle l^2 \rangle$: $D_t = \Gamma \langle l^2 \rangle / (2d)$, and are found to be about 18.5 and 1,830 $\mu\text{m}^2\text{s}^{-1}$ at room temperature using the lattice constant of Cu 3.615 Å, respectively. At $T = 240 \text{ }^\circ\text{C}$, the tracer diffusion coefficients of C monomer and C-O molecule are expected to be about 703 and 10,100 $\mu\text{m}^2\text{s}^{-1}$ from our calculations, respectively.

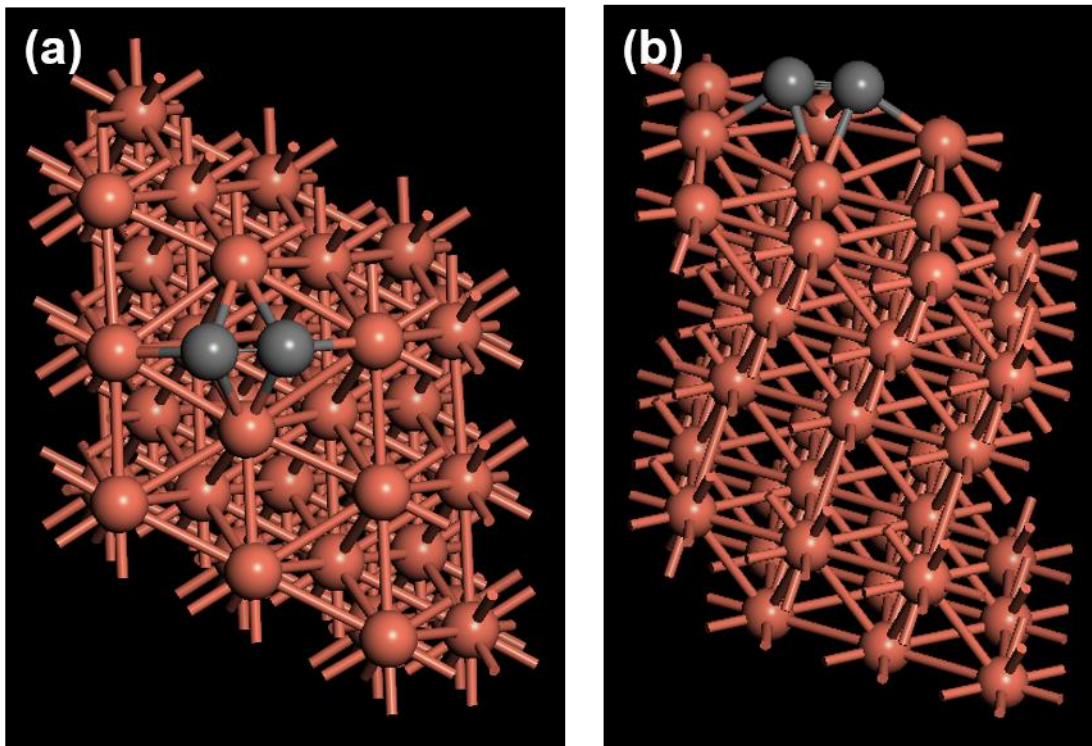


Figure 5.2. Illustration of typical atomic structure model for dimer molecule diffusion on Cu (111) in this study. (a) top view and (b) bird-eye view (all spheres in brown color indicate Cu atoms except two spheres in gray color which indicate the dimer of C or O).

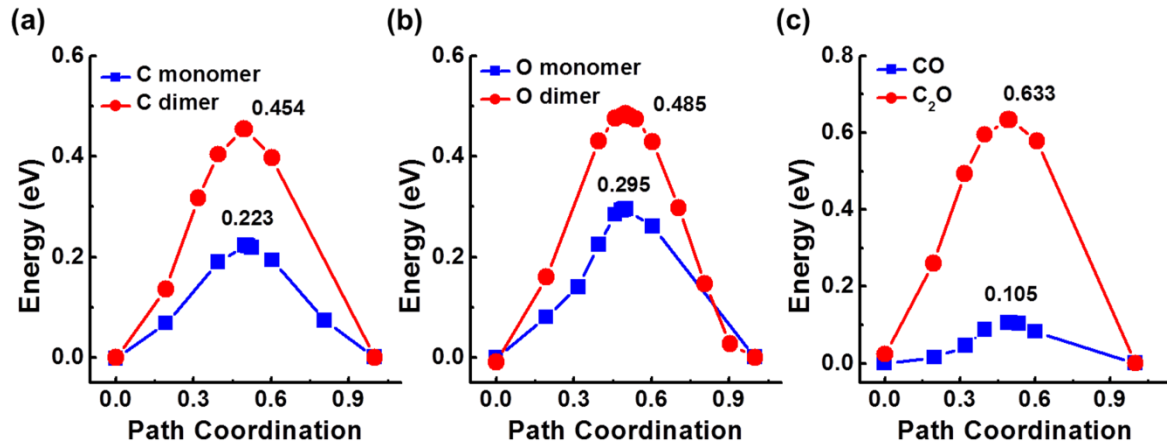


Figure 5.3. Diagram of calculated transitional state energy of atomic or molecular diffusion on Cu (111) surface. (a) C monomer and dimer, (b) O monomer and dimer, (c) C-O and C₂O molecules.

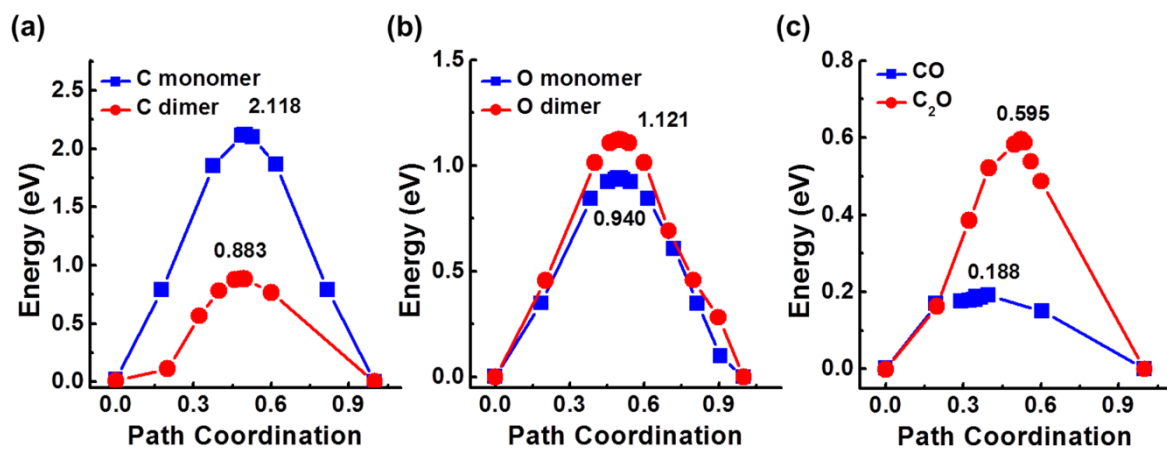


Figure 5.4. Diagram of calculated transitional state energy of atomic or molecular diffusion on Cu (100) surface. (a) C monomer and dimer, (b) O monomer and dimer, (c) C-O and C₂O molecules

Table 5.1. Calculated activation energy barriers (in eV) of the correlated diffusion of monomers, dimers, and trimers, including C and O atoms on Cu (111) and Cu (100) surfaces.

Surface		Monomer	Dimer
Cu(111)	C	0.223	0.454
	O	0.295	0.485
	C-O	0.105	
	C ₂ O	0.633	
Cu(100)	C	2.118	0.883
	O	0.940	1.121
	C-O	0.188	
	C ₂ O	0.595	

5.3 Mechanism for The Formation of GO Sheets.

There is a key question why the GO sheets form through the DAS process using solid C at low temperatures. Central to this issue are the origin of O atoms in the resulting graphene framework and the diffusion of C and O atoms through the Cu foil, followed by the formation of the GO sheets on a Cu surface after an incubation period. Figure 5.5 represents a representative zero-loss energy-filtered bright-field TEM image and a corresponding elemental map of C (based on the three-window technique¹⁰⁸) of the Cu foil after DAS process at 240°C for 120 minutes. The predominant presence of C atoms along the GBs in the Cu is clearly visible from the elemental map; therefore it can be found out that the GBs are the dominant diffusion pathway for C atoms during the DAS process. After the C atoms diffuse to the reverse side of the Cu foil, nucleation results from competition between the surface-diffusion processes, followed by capture of the supercritical nucleus and the evaporation of C-adatoms from the Cu surface. Considering the high activation energy (about 6 eV)¹⁰⁹ for the desorption of C-adatoms and the very low activation energy (DFT calculation results, Table 5.1) of C-adatom diffusion on Cu, we suggest that the formation of the graphene framework on Cu can be described by C attachment/detachment to the edges of the nuclei as the rate-limiting step at low temperatures, thus resulting in the occurrence of two growth regimes as shown in Figure 5.5.

We investigated time-of-flight secondary ion mass spectroscopy (ToF-SIMS) on three different samples to elucidate the origin of the O atoms. Figure 5.6 shows the relative change in the intensities of C⁻ and O⁻ containing species that were ejected from a) an as-received Cu surface, b) a Cu surface annealed at about 790 °C in ambient hydrogen, and c) a GO-covered Cu surface following DAS process at 240 °C for 120 minutes. The levels of oxygen and oxidizing elements on the Cu surface increased as a result of the DAS process and there was also an increased level of C-containing compounds, owing to C-adatom diffusion along the GBs in the Cu. Considering that we found the O distribution with an annealed Cu foil to be quite uniform (based on energy-dispersive spectroscopy (Figure 5.5) in TEM), and given that DAS was conducted in an inert ambient, we suggest that there was no driving force for spontaneous O diffusion through the Cu lattices or along the GBs. In addition, the residual O atoms on the Cu surface cannot have diffused into the graphitic lattice during the DAS process, because O atoms have a higher affinity for the Cu surface than C atoms and our synthesis was conducted at low temperatures. Therefore, we inferred that the O atoms in the resulting GO sheets have diffused from the interior of the Cu crystals during the DAS process.

Spin-polarized density functional theory (DFT) calculations^{70,71} can also support the growth mechanism of the C- and O- diffusion processes that are consistent with the formation of GO sheets on the reverse side of the Cu foils and The DFT calculation results are summarized in Table 1. The diffusion

behavior of monomers, dimers, and trimmers, including C- and O-adatoms, were regarded to on Cu (111) and Cu (100) surfaces, because the activation energy barrier of the correlated diffusion of multi-adatoms on metal surfaces generally increases with the number of adparticles¹¹⁰. We note that the lowest energy barriers for the diffusion of C- and O-adatoms were achieved when C-O dimers diffused over Cu, regardless of the orientation of the crystallographic plane. The energy barriers of C-O dimers on Cu (111) and Cu (100) surfaces were 0.105 and 0.188 eV, respectively. This finding indicates that the O atoms at the GBs in Cu preferentially combined with the diffusing C atoms with a dangling bond, followed by the diffusion of C-O molecules over Cu as well as through GBs as shown in Figure 5.6. Considering very high tracer diffusion coefficients (D_t), C-containing precursors reaching the reverse side of the Cu foil, diffuse laterally along the Cu (111) surface for a short period and lead to the growth of graphene framework over large areas after an incubation time, driven by the strong affinity of C atoms to self-assemble and expand the sp^2 lattice¹¹¹. Considering that C-C and C-O bonds tend to segregate and that O atoms are almost insoluble in C clusters at low temperatures^{83,112}, the resulting films become highly graphitic sheets that are decorated with oxygenated functionalities.

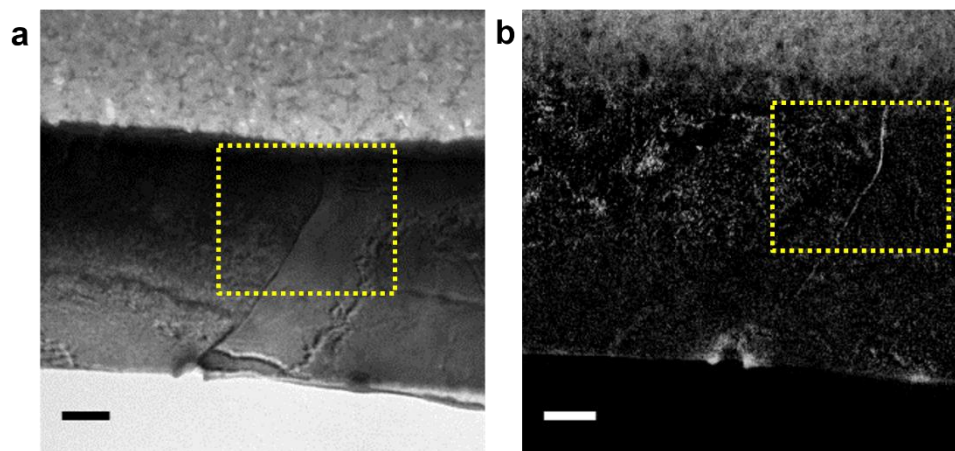


Figure 5.5. Growth mechanism of GO sheets and origin of The C and O atoms in the GO sheets. (a) Zero-loss filtered bright-field cross-sectional TEM image of the Cu foil after DAS at 240 °C for 120 min (using an energy slit width of 10 eV to select the zero-loss peak) and (b) the corresponding C map. The yellow rectangles denote the same location in the TEM images (scale bars, 0.2 μm).

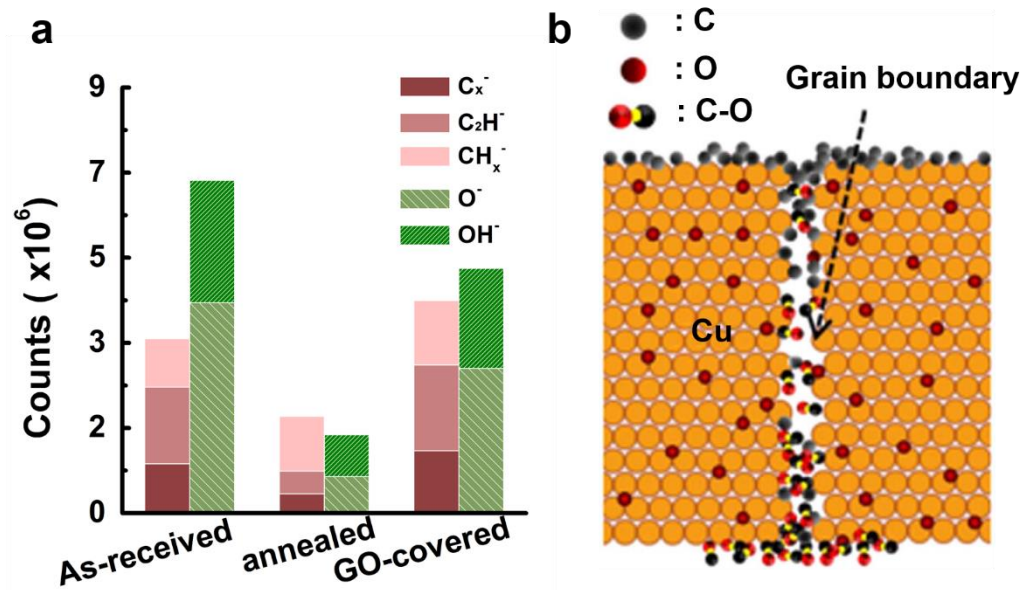


Figure 5.6. Origin of the C and O atoms and growth mechanism in the GO sheets. (a) Changes in the elemental composition of C⁻ and O⁻ containing species, based on TOF-SIMS analysis of the surfaces of an as-received Cu foil, an annealed Cu foil at 790 °C in ambient hydrogen, and a GO-covered Cu foil that was grown at 240 °C for 120 min. (b) Schematic diagram of GO growth mechanism during DAS process using solid C; C atoms began to diffuse through the Cu along the GBs of the foil while trapping the O species dissolved in the Cu, leading to the predominant diffusion of C-O molecules over Cu as well as through GBs.

Chapter 6. Tunable Chemical Composition and Electrical Properties

6.1 Control of O/C Composition and Tunable Bandgap Energy.

The O composition in the GO sheets directly correlates with the heating profile of the Cu foil during the annealing step (Figure 6.1 (a)). The GO sheets were synthesized at 240 °C for 60 min with the Cu foil annealed at 790 °C for 120min (type I); at 240 °C for 120 min with the Cu foil annealed at 790 °C for 20 min (type II); and at 240 °C for 120 min with the Cu foil annealed at 790 °C for 260 min (type III). Modifying the heating profile enables the residual O concentration in Cu to be controlled. Therefore it is easy to control the composition of O atoms in the resulting GO sheets. GO becomes less oxygenated as the extended heating proceeds. The detailed chemical states of the carbon and oxygen functionalites under different condition (Type I to Type III) can be found in Figure 6.2. Thus, Figure 6.3 represents XPS depth profile of C and O atoms in the Cu foils used after the DAS was accomplished at three different annealing conditions that the O/C composition in GO was decreased from 0.80 to 0.32 as the annealing time increased from 20 to 260 minutes at about 790 °C as shown in Figure 6.2 (b) and This result is notable because the precise control of O content in GO during the synthesis has not yet been reported for any chemical synthesis processes⁸¹⁻⁸⁴.

Importantly, the bandgap energy of GO can be tuned by varying the O/C composition in GO sheets. UV-Vis measurements show that the bandgap of GO decreases from about 2.1 eV to 1.6 eV as the O/C composition decreases from 0.80 to 0.32 (Figure 6.1 (b)). This result demonstrates the ability to control the bandgap of GO by simply annealing the Cu foil prior to solid-state diffusion process. It is worthwhile to note that the average sizes of graphitic grains in the GO sheets were all about 10 nm using HR-TEM measurements, regardless of O/C composition. However, we found out the systematic variations of the bandgap values of the GO sheets by varying the O/C composition, indicating that the oxygen functionalities existing on the graphitic grains in GO are the cause of bandgap controllability. In principle, the bandgap can be further reduced by long-period thermal annealing of the Cu foil.

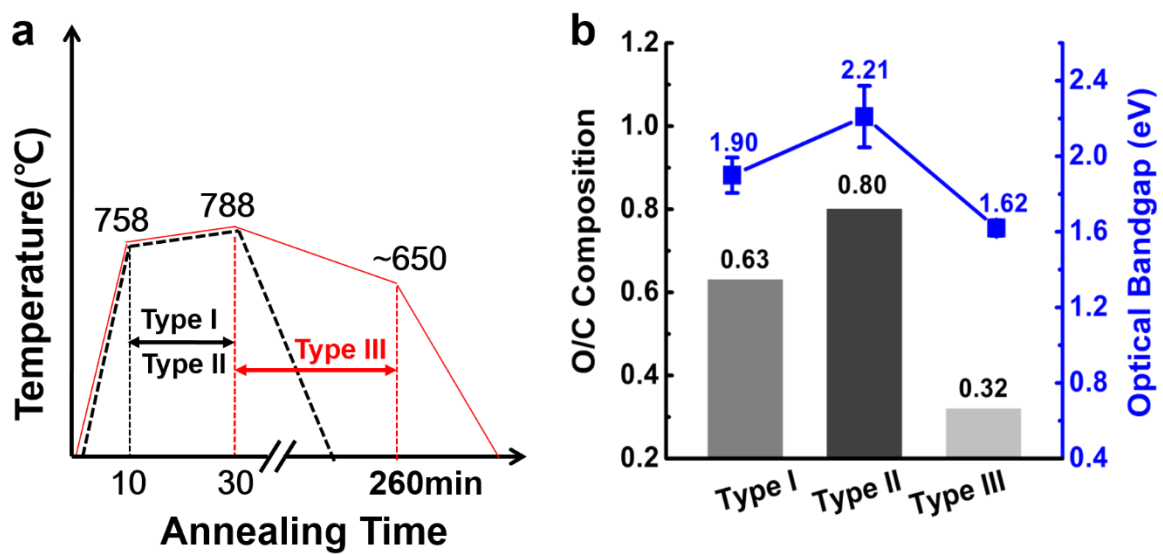
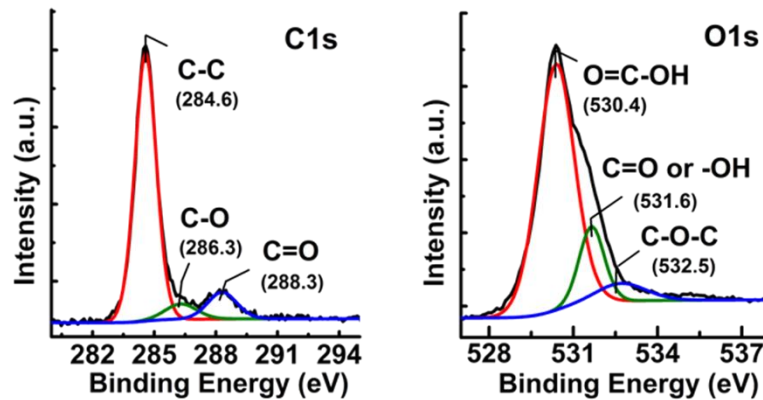
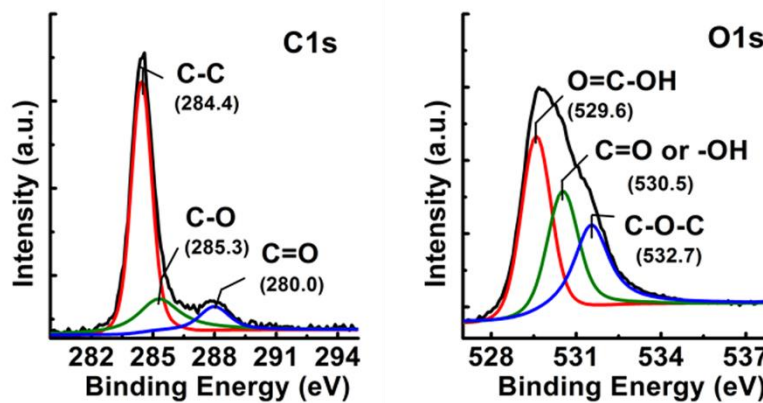


Figure 6.1. (a) The heating profile of the Cu foil during annealing step. Modifying the heating profile method enable the residual O concentration in Cu. (b) Changes in the O/C composition and the calculated bandgap energy in the GO sheets that were formed on a Cu surface under three conditions. Error bars are the standard deviation of the band gap energy measured in five different samples grown under the same condition.

1) Type I



2) Type II



3) Type III

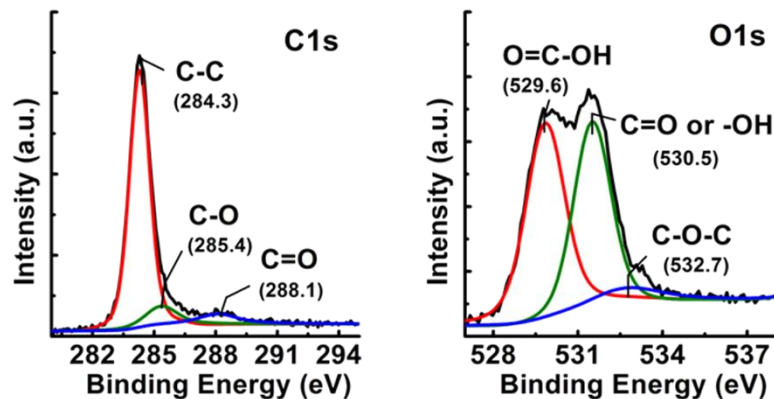


Figure 6.2. High resolution XPS C 1s and O 1s line scans of the GO sheets that were formed on a Cu surface under three different conditions. The GO sheets were synthesized at 240 °C for 60 minutes with the Cu foil annealed at 790 °C for 20 minutes (type I); at 240 °C for 120 minutes with the Cu foil annealed at 790 °C for 20 minutes (type II); and at 240 °C for 120 minutes with the Cu foil annealed at 790 °C for 260 minutes (type III).

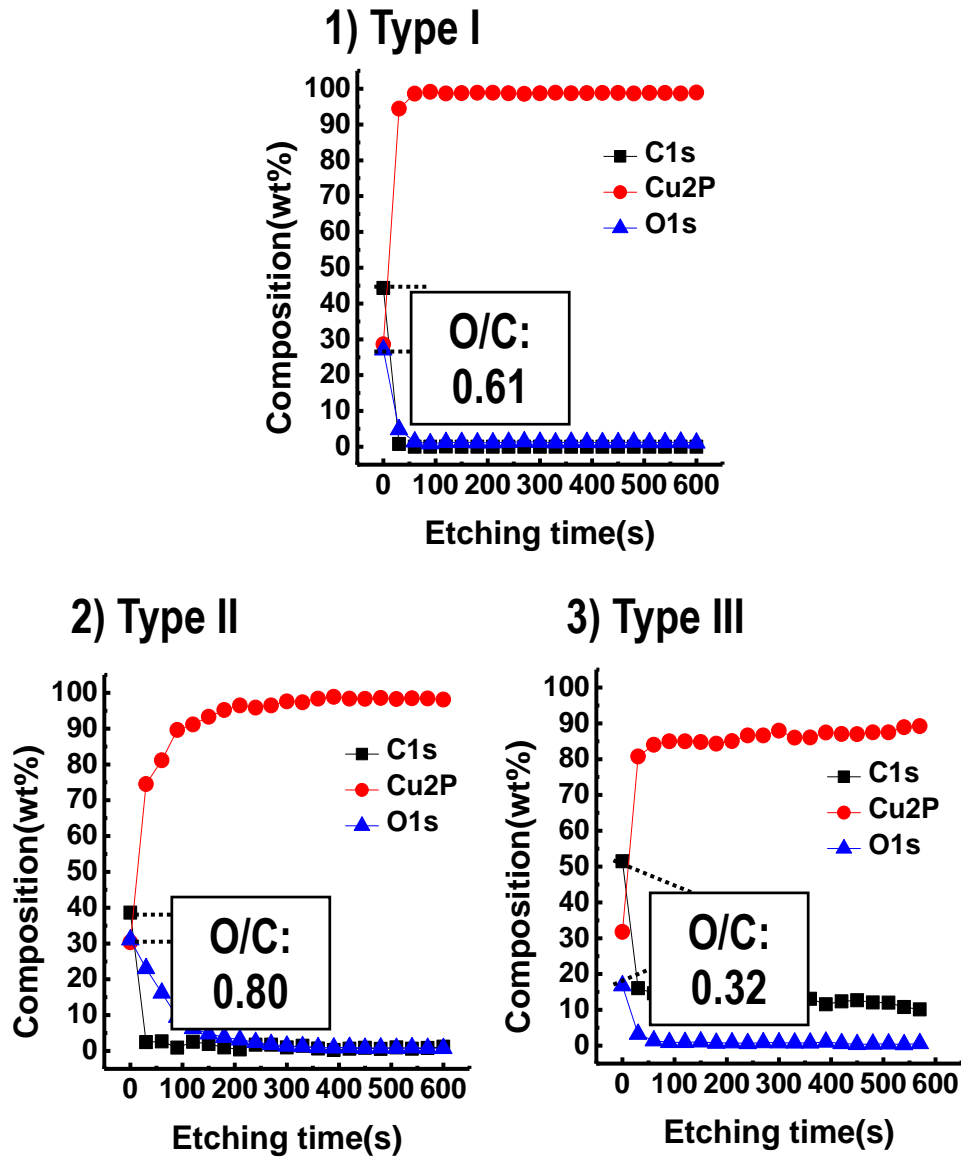


Figure 6.3. XPS depth profiles of C and O atoms in the Cu foils used after the DAS was accomplished at three different conditions. The etching processes were conducted from the GO-covered Cu surfaces and the average etch rate was about 1.9 Å/s.

6.2 Tunable Electrical Properties of The GO Sheets

To investigate the electronic properties of the individual GO sheets with the different O/C compositions, back-gated GO-based FET devices were measured as shown in Figure 6.4. FET devices with a channel length of 5 μm and channel widths of 200 μm (O/C~0.8) and 20 μm (O/C~0.3) atop 300 nm SiO_2 with a p-Si back gate were fabricated by the conventional photolithography. All of the reported electrical measurements were taken under vacuum at temperatures ranging from 20 to 300 K.

The carrier mobilities can be estimated by using

$$\mu = \frac{\Delta I_{DS}}{C_{ox} W / L V_{DS} \Delta V_{GS}} \quad (6.1)$$

where μ is the carrier mobility, W and L are FET width and length, respectively, $C_{ox} = \epsilon_{ox} \epsilon_0 / t_{ox}$ is the gate oxide capacitance ($\epsilon_{ox} = 3.9$ is silicon dioxide permittivity and t_{ox} is the gate oxide thickness), and ΔI_{DS} is induced by ΔV_{GS} . Using the FET parameters given above, the hole and electron mobilities were extracted as shown in Figure 6.5.

As shown in Figure 6.5 (a,b), regardless of the O content in the GO sheets, the 'V' shape of the ambipolar transfer characteristics and the shift of minimum conduction point to positive gate voltage are observed for both samples, which are characteristics normally observed in both pristine graphene⁴ and chemically-reduced GO⁸¹⁻⁸⁴. The principal similarity between the gate dependence of the GO sheet and graphene is a direct indication of the presence of intact graphitic grains in the GO sheets⁹⁴, as observed in HR-TEM and Raman results of the GO. It was found that achieving lower O/C composition yields significantly improved electrical performance and the GO sheets exhibited tunable field effect mobilities from 19.7 ± 4.1 to $82.6 \pm 10.2 \text{ cm}^2\text{V}^{-1}\text{s}^{-1}$ at room temperature as the O/C composition decreases from 0.80 to 0.32 O/C composition. We note that the as-synthesized GO sheets were electrically active without any further chemical and/or thermal treatment, in contrast to chemically-derived GO⁸¹⁻⁸⁴, and the measured carrier (hole) mobility of the GO sheet with O/C composition of 0.32 is superior to the previously reported mobility values of chemically-reduced GO-based FETs^{74,49-51}. The higher mobilities in our GO sheet with FET devices compared to those achieved in chemically-reduced GO flakes, could be attributed to the morphological nature of the monolithic GO sheets without any junction/overlapping regions between graphitic grains(individual graphitic sheets) since the weak coupling between adjacent GO flakes (i.e. the high internanosheet resistance) may cause the device performance to be much less than that of single nanosheets¹¹³. In addition, the conductivity of both samples at all gate voltages from -80 to $+80$ V increased with temperature, indicating that both types samples exhibit semiconducting behavior, in contrast to the semimetallic pristine graphene⁴.

To further investigate the conduction mechanism in our monolithic GO sheets, we examined the variation of the conductivity at minimum conduction point (σ_{\min}) as a function of $T^{-1/3}$ for three different values of bias voltage (V_{ds}), as shown in Figure 6.5, Figure 6.6 and Figure 6.7.

In the VRH model, the temperature dependence of the conductivity σ can be described by the from

$$\sigma = A \exp\left(-\frac{B}{T^{1/3}}\right) \quad (6.2)$$

The parameters A and B are expressed as

$$A = \frac{eR_0^2 v_{ph}}{k_B} \quad (6.3)$$

$$B = \left(\frac{3\alpha^2}{N(E_F)k_B}\right)^{1/3} \quad (6.4)$$

Where e is the electronic charge, R_0 is the optimum hopping distance, v_{ph} is the frequency of the phonons associated with the hopping process, k_B is the Boltzmann constant, α is the wave function decay constant, and $N(E_F)$ is the density of states near the Fermi level. VRH involves consecutive inelastic tunneling processes between two localized states and has been frequently observed in disordered systems, including GO and amorphous carbon structures. The following general temperature dependence VRH model simply described $I = I_0 e^{-(T_0/T)^{1/n}}$, where $(n-1)$ is the dimensionality of the sample¹¹⁴⁻¹¹⁶. The two-dimensional (2D) character reflected by the observed $T^{1/3}$ dependence is consistent with 2D structure of the sheets.

In the case of the GO sheet with a higher O/C composition of 0.80, the best linear fits of the temperature-dependent data were obtained at all examined V_{ds} by plotting $\ln(\sigma_{\min})$ versus $T^{-1/3}$, pointing toward two-dimensional variable-range hopping (2D-VRH) as a plausible charge transport mechanism^{49,117}, whereas deviation from the 2D-VRH model was observed at the lower temperature regime for the highest value of bias voltage ($V_{ds} = 1$ V). As shown in Figure 6.5, Figure 6.6 and Figure 6.7 respectively. In view of the above-described structural measurements, i.e. HR-TEM and Raman results of the GO, hopping presumably occurs between the intact graphitic grains, which are separated by clusters of atomic defects. The deviation from linear fit at the lower temperature regime can be explained by the contribution of the field-driven conduction without thermal activation¹¹⁷⁻¹¹⁹. However, the GO sheet with a lower O/C composition of 0.32 showed a deviation from the linear fit (i.e. 2D-VRH model) at all observed V_{ds} and the temperature dependence of the σ_{\min} at the higher temperature regime can be fitted reasonably well with the Arrhenius model, suggesting that thermally excited carriers begin to dominate electrical conduction¹¹⁴. Based on the electrical transport properties of the GO sheets, we can conjecture that the bandgap energy of GO was narrowed down as the O/C composition decreased from 0.80 to 0.32, which is in agreement with the UV-Vis measurement.

Overall, a consequent results is clearly observed between variations in the O/C composition and the optoelectronic properties of the resulting GO sheets. By monitoring opoelectronic properties, we have found that the electrical transport mechanism in our physically-synthesized, monolithic GO sheets is, despite the significantly higher conductivity, more similar to chemically-reduced GO than to as-synthesized, chemically-derived GO. Our results suggests that highly tunable GO sheets may enable the design of monolithic semiconducting and optoelectronic devices, in combination with our solution-free, physical synthesis approach.

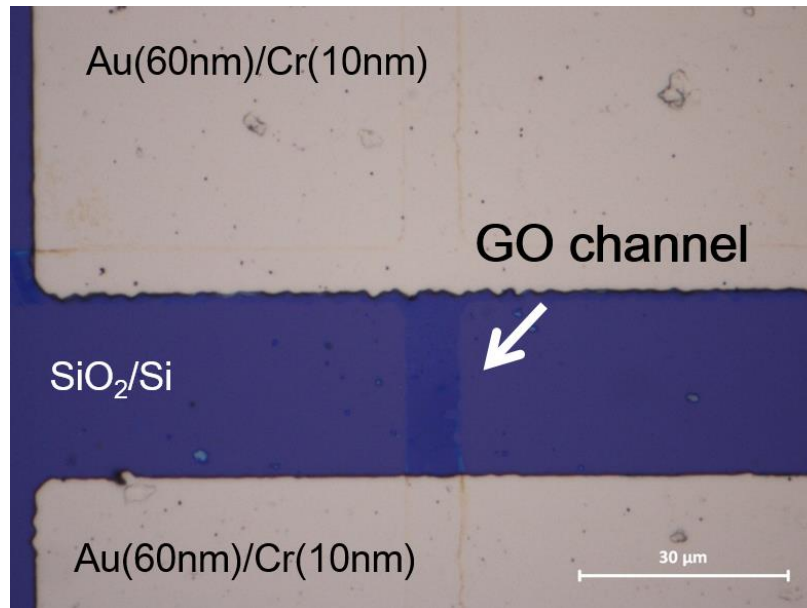


Figure. 6.4. Optical microscope image of back-gated GO based FET devices. FET devices with a channel length of 5 μm and channel widths of 200 μm (O/C~0.8) and 20 μm (O/C~0.3) atop 300 nm SiO₂ with a p-Si back gate were fabricated by the conventional photolithography.

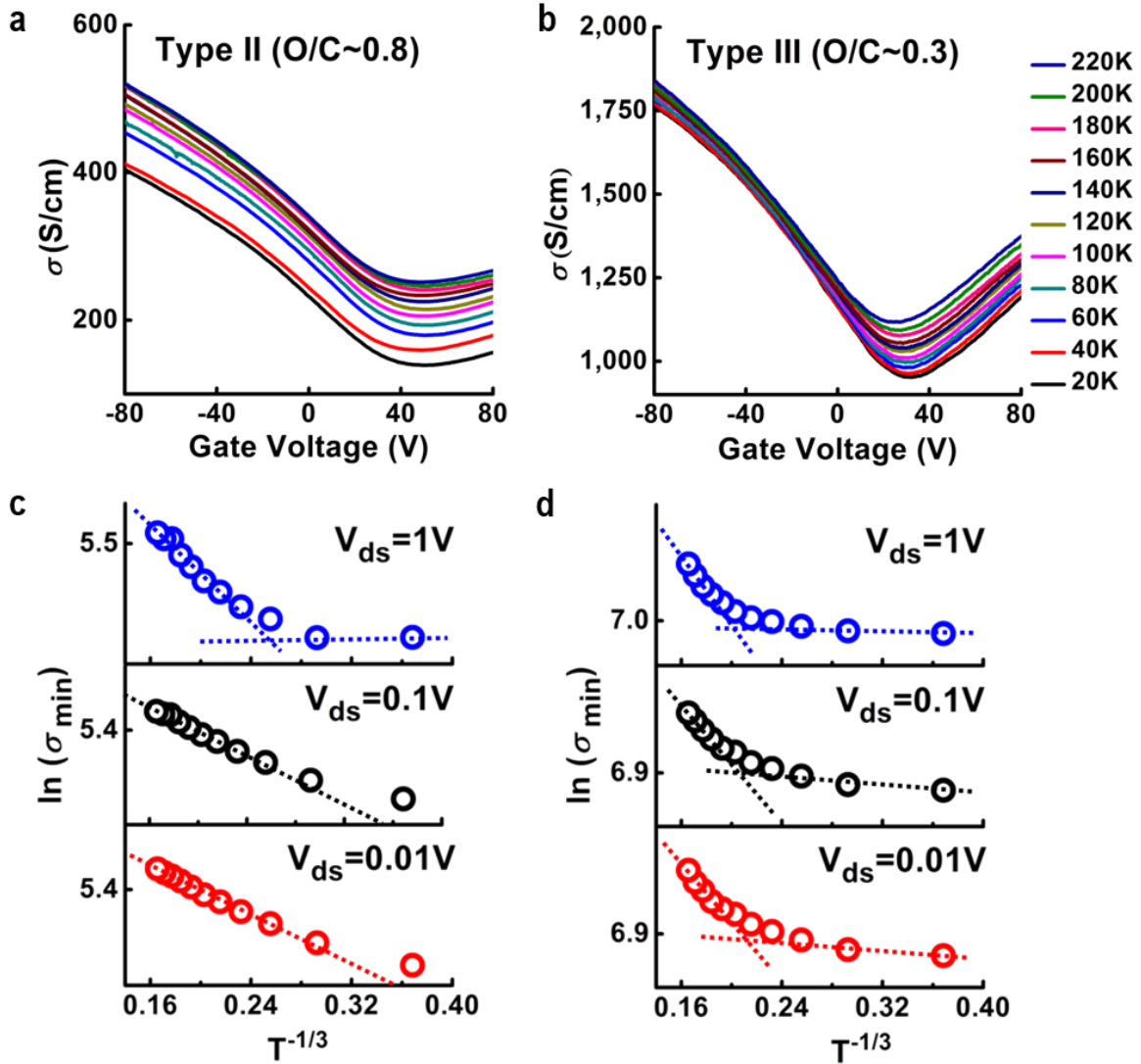


Figure 6.5. Controllable electrical properties of the GO sheets with varying the O/C composition. (a) Transfer characteristics of the GO sheets of 0.80 (type II, (a)) and 0.32 (type III, (b)) with different O/C compositions measured at temperatures ranging from 20 K to 300 K ($V_{ds} = 0.01$ V). (c,d) Minimum conductivity σ_{\min} of the GO sheets with different O/C compositions of 0.80 (type II, (c)) and 0.32 (type III, (d)) at three different values of bias voltage (V_{ds}) ranging from 0.01 to 1 V as a function of $T^{-1/3}$.

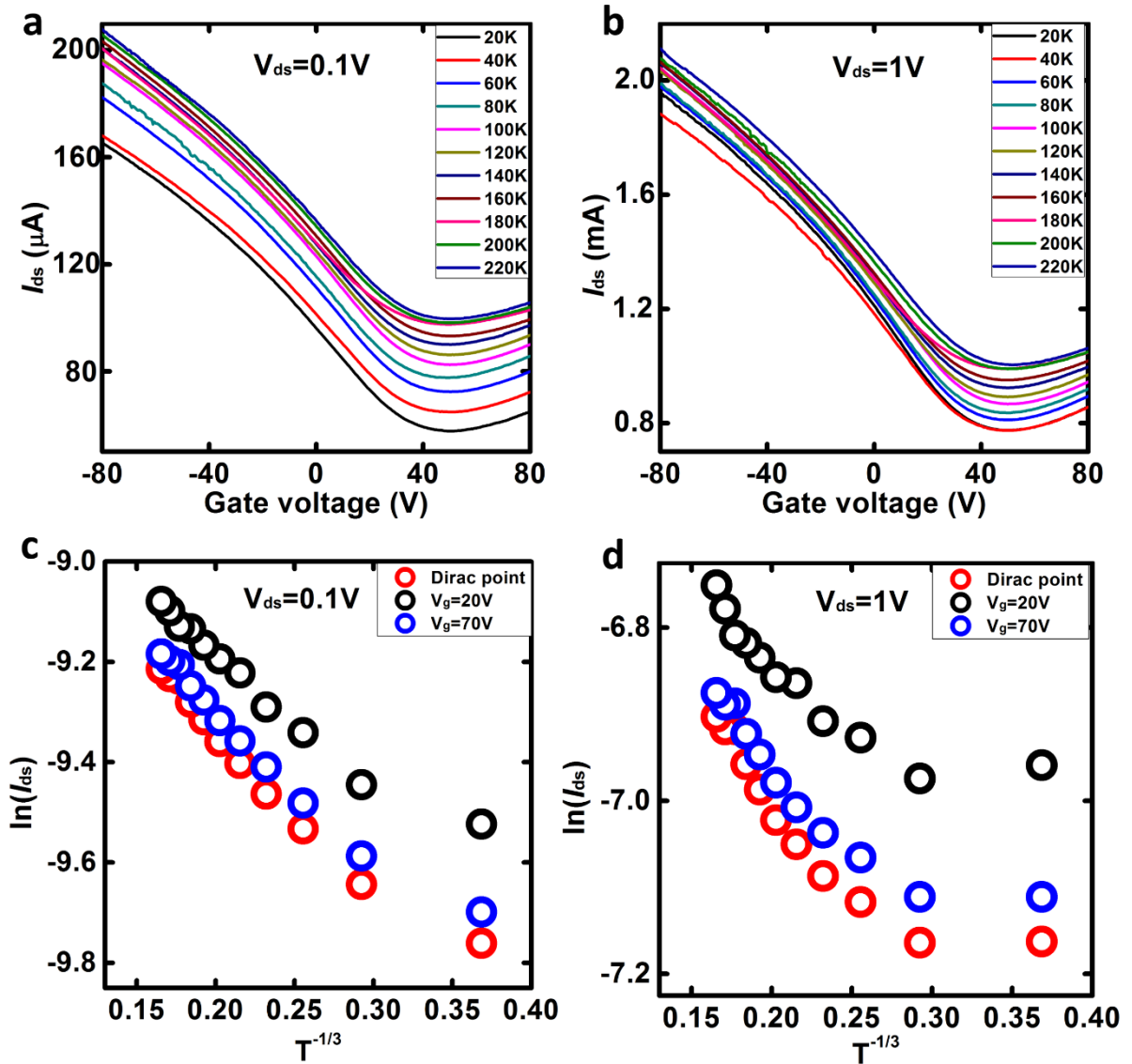


Figure 6.6. Tunable electrical properties of the GO sheets with varying the O/C composition of 0.80 (type II) from 20 K to 220 K. (a,b) Transfer characteristics of the GO sheets $V_{ds} = 0.1$ V and $V_{ds} = 1$ V. (c,d) Minimum conductivity σ_{\min} as a Dirac point of the GO sheets with different O/C composition of 0.80 (type II) at bias voltage (V_{ds}) ranging from 0.1 to 1 V and gate voltage ($V_g = 20$ V and $V_g = 70$ V) as a function of $T^{-1/3}$.

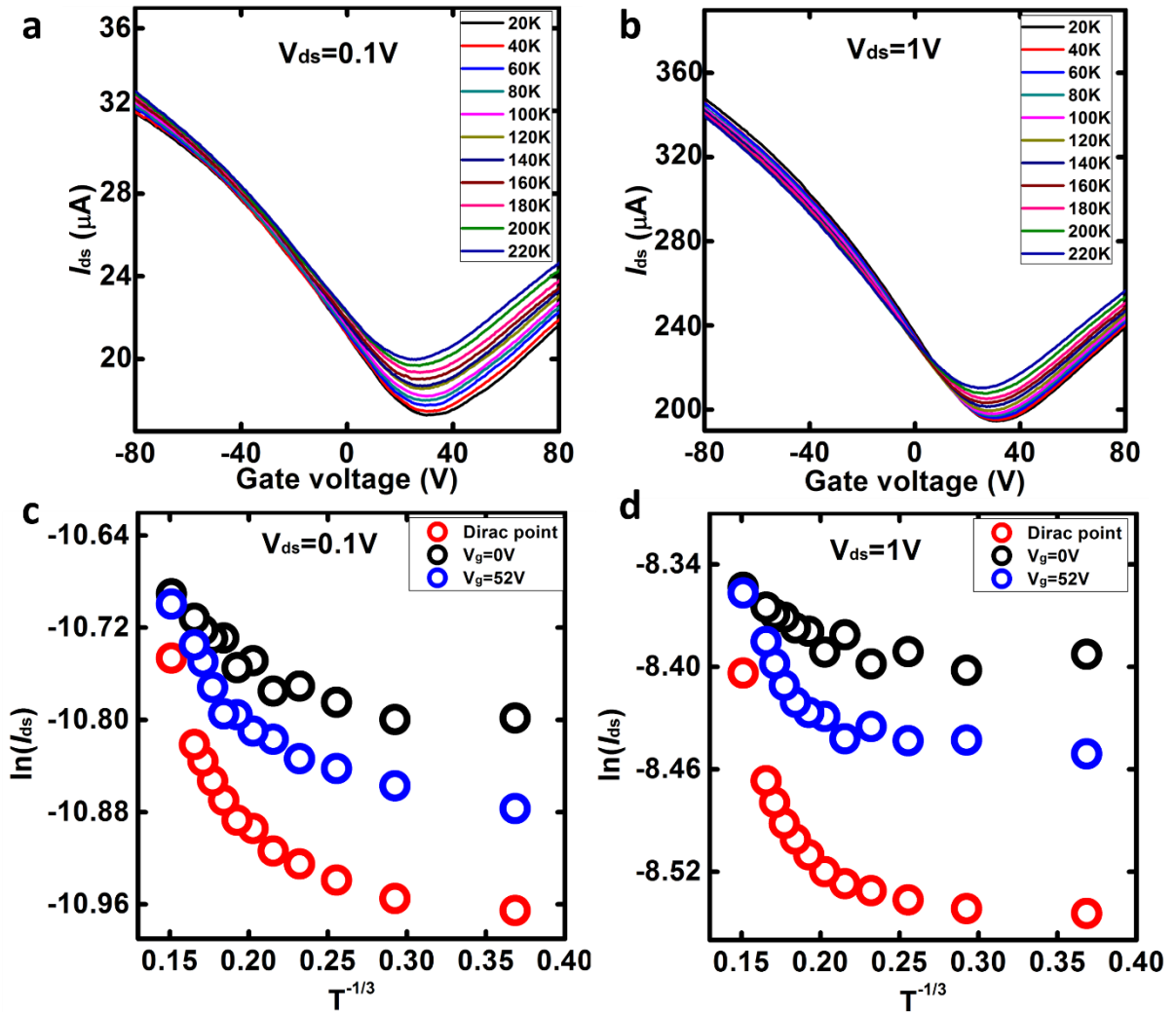


Figure 6.7. Tunable electrical properties of the GO sheets with varying the O/C composition of 0.32 (type III) from 20 K to 220 K. (a,b) Transfer characteristics of the GO sheets $V_{ds} = 0.1$ V and $V_{ds} = 1$ V. (c,d) Minimum conductivity σ_{\min} as a Dirac point of the GO sheets with different O/C composition of 0.80 (type II) at bias voltage (V_{ds}) ranging from 0.1 to 1 V and gate voltage ($V_g = 20$ V and $V_g = 70$ V) as a function of $T^{-1/3}$.

Chapter 7. Conclusion

We have successfully demonstrated a new physical method for the controllable growth of monolithic GO sheets on Cu surfaces at low temperatures. This method offers a more promising approach to the precision assembly of graphene-based devices than established chemically derived synthesis method and could complement existing production techniques. The simplicity of solution-free, physical synthesis of the GO sheets in combination with controllable electronic and optoelectronic properties with different O/C composition may provide the shortest path to precision device assembly based on graphene and its derivatives. Furthermore, our physical method can pave the way for the realization of monolithic, two-dimensional chemically-modified C sheets with controllable composition, which are produced by pre-treating the metallic foils under various conditions (ambient, temperature, doping *etc.*) prior to solid-state diffusion media as the DAS process. Considering the inherent potential of two-dimensional C sheets with high flexibility, transparency and mechanical strength, one could anticipate the use of stacked heterostructure based on two-dimensional sheet designs for the next generation of flexible nano-devices. In conclusion, advances in the development of ultra-high-purity metallic diffusion media with a controlled doping concentration can open the door to the realization of graphene sheets with a defined substitutional doping concentration.

References

1. Peierls, R. In *Quelques propriétés typiques des corps solides*, Annales de l'institut Henri Poincaré, 1935; pp 177-222.
2. Landau, L., Zur Theorie der phasenumwandlungen II. *Phys. Z. Sowjetunion* **1937**, *11*, 26-35.
3. Mermin, N. D., Crystalline order in two dimensions. *Physical Review* **1968**, *176* (1), 250.
4. Novoselov, K. S.; Geim, A. K.; Morozov, S.; Jiang, D.; Zhang, Y.; Dubonos, S. a.; Grigorieva, I.; Firsov, A., Electric field effect in atomically thin carbon films. *Science* 2004, *306* (5696), 666-669.
5. Kuila, T.; Bose, S.; Mishra, A. K.; Khanra, P.; Kim, N. H.; Lee, J. H., Chemical functionalization of graphene and its applications. *Progress in Materials Science* 2012, *57* (7), 1061-1105.
6. Geim, A. K.; Novoselov, K. S., The rise of graphene. *Nature materials* 2007, *6* (3), 183-191.
7. Schultz, H. P., Topological organic chemistry. polyhedranes and prismanes. *The Journal of Organic Chemistry* 1965, *30* (5), 1361-1364.
8. Osawa, E., Superaromaticity. *Kagaku* 1970, *25* (9), 854-863.
9. Halford, B., The world according to Rick. *Chemical & Engineering News* 2006, *84* (41), 13-19.
10. Wang, X.; Li, Q.; Xie, J.; Jin, Z.; Wang, J.; Li, Y.; Jiang, K.; Fan, S., Fabrication of ultralong and electrically uniform single-walled carbon nanotubes on clean substrates. *Nano letters* 2009, *9* (9), 3137-3141.
11. Inman, M., Legendary Swords' Sharpness, Strength From Nanotubes, Study Says. *National Geographic News* 2006.
12. Gullapalli, S.; Wong, M. S., Nanotechnology: a guide to nano-objects. *Chemical Engineering Progress* 2011, *107* (5), 28-32.
13. "Scientific Background on the Nobel Prize in Physics 2010, GRAPHENE" (PDF). *The Royal Swedish Academy Of Science*.
14. Novoselov, K.; Geim, A. K.; Morozov, S.; Jiang, D.; Katsnelson, M.; Grigorieva, I.; Dubonos, S.; Firsov, A., Two-dimensional gas of massless Dirac fermions in graphene. *Nature* 2005, *438* (7065), 197-200.
15. Mayorov, A. S.; Gorbachev, R. V.; Morozov, S. V.; Britnell, L.; Jalil, R.; Ponomarenko, L. A.; Blake, P.; Novoselov, K. S.; Watanabe, K.; Taniguchi, T., Micrometer-scale ballistic transport in encapsulated graphene at room temperature. *Nano letters* 2011, *11* (6), 2396-2399.

16. Balandin, A. A.; Ghosh, S.; Bao, W.; Calizo, I.; Teweldebrhan, D.; Miao, F.; Lau, C. N., Superior thermal conductivity of single-layer graphene. *Nano letters* 2008, 8 (3), 902-907.
17. Lee, C.; Wei, X.; Kysar, J. W.; Hone, J., Measurement of the elastic properties and intrinsic strength of monolayer graphene. *Science* 2008, 321 (5887), 385-388.
18. Bunch, J. S.; Verbridge, S. S.; Alden, J. S.; van der Zande, A. M.; Parpia, J. M.; Craighead, H. G.; McEuen, P. L., Impermeable atomic membranes from graphene sheets. *Nano letters* 2008, 8 (8), 2458-2462.
19. Zhu, Y.; Murali, S.; Cai, W.; Li, X.; Suk, J. W.; Potts, J. R.; Ruoff, R. S., Graphene and graphene oxide: synthesis, properties, and applications. *Advanced Materials* 2010, 22 (35), 3906-3924.
20. Moser, J.; Barreiro, A.; Bachtold, A., Current-induced cleaning of graphene. *Applied Physics Letters* 2007, 91 (16), 163513.
21. Lin, Y.-M.; Dimitrakopoulos, C.; Jenkins, K. A.; Farmer, D. B.; Chiu, H.-Y.; Grill, A.; Avouris, P., 100-GHz transistors from wafer-scale epitaxial graphene. *Science* 2010, 327 (5966), 662-662.
22. Ishibashi, T.; Furuta, T.; Fushimi, H.; Kodama, S.; NAGATSUMA, T.; SHIMIZU, N.; MIYAMOTO, Y., InP/InGaAs uni-traveling-carrier photodiodes. *IEICE transactions on electronics* 2000, 83 (6), 938-949.
23. Reed, G. T.; Mashanovich, G.; Gardes, F.; Thomson, D., Silicon optical modulators. *Nature photonics* 2010, 4 (8), 518-526.
24. Yang, S.; Feng, X.; Ivanovici, S.; Müllen, K., Fabrication of graphene-encapsulated oxide nanoparticles: towards high-performance anode materials for lithium storage. *Angewandte Chemie International Edition* 2010, 49 (45), 8408-8411.
25. Shao, Y.; Wang, J.; Wu, H.; Liu, J.; Aksay, I. A.; Lin, Y., Graphene based electrochemical sensors and biosensors: a review. *Electroanalysis* 2010, 22 (10), 1027-1036.
26. Novoselov, K. S.; Geim, A. K.; Morozov, S.; Jiang, D.; Zhang, Y.; Dubonos, S. a.; Grigorieva, I.; Firsov, A., Electric field effect in atomically thin carbon films. *Science* **2004**, 306 (5696), 666-669.
27. Emtsev, K. V.; Bostwick, A.; Horn, K.; Jobst, J.; Kellogg, G. L.; Ley, L.; McChesney, J. L.; Ohta, T.; Reshanov, S. A.; Röhrl, J., Towards wafer-size graphene layers by atmospheric pressure graphitization of silicon carbide. *Nature materials* **2009**, 8 (3), 203-207.
28. Sun, Z.; Yan, Z.; Yao, J.; Beitler, E.; Zhu, Y.; Tour, J. M., Growth of graphene from solid carbon sources. *Nature* 2010, 468 (7323), 549-552.
29. Losurdo, M.; Giangregorio, M. M.; Capezzuto, P.; Bruno, G., Graphene CVD growth on

- copper and nickel: role of hydrogen in kinetics and structure. *Physical Chemistry Chemical Physics* 2011, 13 (46), 20836-20843.
30. Wei, D.; Liu, Y.; Wang, Y.; Zhang, H.; Huang, L.; Yu, G., Synthesis of N-doped graphene by chemical vapor deposition and its electrical properties. *Nano letters* 2009, 9 (5), 1752-1758.
 31. Dean, C.; Young, A., MericI; LeeC; WangL; SorgenfreiS; WatanabeK; TaniguchiT; KimP; Shepard, KL; HoneJ. *Nat Nano* 2010, 5 (10), 722-726.
 32. Wallace, P. R., The band theory of graphite. *Physical Review* 1947, 71 (9), 622.
 33. Saito, R.; Dresselhaus, G.; Dresselhaus, M. S., Physical properties of carbon nanotubes. *World Scientific*: 1998; Vol. 35.
 34. Neto, A. C.; Guinea, F.; Peres, N.; Novoselov, K. S.; Geim, A. K., The electronic properties of graphene. *Reviews of modern physics* 2009, 81 (1), 109.
 35. Wallace, P. R., The band theory of graphite. *Physical Review* **1947**, 71 (9), 622.
 36. Brodie, B., Sur le poids atomique du graphite. *Ann. Chim. Phys* 1860, 59 (466), e472.
 37. Schafhaeutl, C., LXXXVI. On the combinations of carbon with silicon and iron, and other metals, forming the different species of cast iron, steel, and malleable iron. *The London and Edinburgh Philosophical Magazine and Journal of Science* 1840, 16 (106), 570-590.
 38. William, S.; Hummers, J.; Offeman, R. E., Preparation of graphitic oxide. *J Am Chem Soc* 1958, 80 (6), 1339.
 39. He, H.; Klinowski, J.; Forster, M.; Lerf, A., A new structural model for graphite oxide. *Chemical Physics Letters* 1998, 287 (1), 53-56.
 40. Pianet, I.; André, Y.; Ducasse, M.-A. s.; Tarascou, I.; Lartigue, J.-C.; Pinaud, N. I.; Fouquet, E.; Dufourc, E. J.; Laguerre, M., Modeling procyanidin self-association processes and understanding their micellar organization: a study by diffusion NMR and molecular mechanics. *Langmuir* 2008, 24 (19), 11027-11035.
 41. Stankovich, S.; Piner, R. D.; Chen, X.; Wu, N.; Nguyen, S. T.; Ruoff, R. S., Stable aqueous dispersions of graphitic nanoplatelets via the reduction of exfoliated graphite oxide in the presence of poly (sodium 4-styrenesulfonate). *Journal of Materials Chemistry* 2006, 16 (2), 155-158.
 42. Kotov, N. A.; Dékány, I.; Fendler, J. H., Ultrathin graphite oxide–polyelectrolyte composites prepared by self-assembly: Transition between conductive and non-conductive states. *Advanced Materials* 1996, 8 (8), 637-641.
 43. Du, X.; Xiao, M.; Meng, Y.; Hay, A., Novel synthesis of conductive poly (arylene disulfide)/graphite nanocomposite. *Synthetic metals* **2004**, 143 (1), 129-132.
 44. Liu, P.; Gong, K., Synthesis of polyaniline-intercalated graphite oxide by anin situ

- oxidative polymerization reaction. *Carbon* 1999, 4 (37), 706-707.
45. Stankovich, S. et al. Synthesis of graphene-based nanosheets via chemical reduction of exfoliated graphite oxide. *Carbon* 45, 1558–1565 (2007).
 46. Stankovich, S.; Dikin, D. A.; Dommett, G. H.; Kohlhaas, K. M.; Zimney, E. J.; Stach, E. A.; Piner, R. D.; Nguyen, S. T.; Ruoff, R. S., Graphene-based composite materials. *Nature* **2006**, 442 (7100), 282-286.
 47. Wang, G.; Yang, J.; Park, J.; Gou, X.; Wang, B.; Liu, H.; Yao, J., Facile synthesis and characterization of graphene nanosheets. *The Journal of Physical Chemistry C* **2008**, 112 (22), 8192-8195.
 48. Schniepp, H. C.; Li, J.-L.; McAllister, M. J.; Sai, H.; Herrera-Alonso, M.; Adamson, D. H.; Prud'homme, R. K.; Car, R.; Saville, D. A.; Aksay, I. A., Functionalized single graphene sheets derived from splitting graphite oxide. *The Journal of Physical Chemistry B* **2006**, 110 (17), 8535-8539.
 49. Gómez-Navarro, C.; Weitz, R. T.; Bittner, A. M.; Scolari, M.; Mews, A.; Burghard, M.; Kern, K., Electronic transport properties of individual chemically reduced graphene oxide sheets. *Nano letters* 2007, 7 (11), 3499-3503.
 50. Sarkar, S.; Raul, K.; Pradhan, S.; Basu, S.; Nayak, A., Magnetic properties of graphite oxide and reduced graphene oxide. *Physica E: Low-dimensional Systems and Nanostructures* 2014, 64, 78-82.
 51. Boukhvalov, D. W.; Katsnelson, M. I., Modeling of graphite oxide. *Journal of the American Chemical Society* **2008**, 130 (32), 10697-10701.
 52. Chang, H.; Sun, Z.; Yuan, Q.; Ding, F.; Tao, X.; Yan, F.; Zheng, Z., Thin Film Field-Effect Phototransistors from Bandgap-Tunable, Solution-Processed, Few-Layer Reduced Graphene Oxide Films. *Advanced Materials* 2010, 22 (43), 4872-4876.
 53. Mathkar, A.; Tozier, D.; Cox, P.; Ong, P.; Galande, C.; Balakrishnan, K.; Leela Mohana Reddy, A.; Ajayan, P. M., Controlled, stepwise reduction and band gap manipulation of graphene oxide. *The Journal of Physical Chemistry Letters* 2012, 3 (8), 986-991.
 54. Bagri, A.; Mattevi, C.; Acik, M.; Chabal, Y. J.; Chhowalla, M.; Shenoy, V. B., Structural evolution during the reduction of chemically derived graphene oxide. *Nature chemistry* 2010, 2 (7), 581-587.
 55. Gómez-Navarro, C.; Meyer, J. C.; Sundaram, R. S.; Chuvilin, A.; Kurasch, S.; Burghard, M.; Kern, K.; Kaiser, U., Atomic structure of reduced graphene oxide. *Nano letters* 2010, 10 (4), 1144-1148.
 56. Geim, A. K.; Novoselov, K. S., The rise of graphene. *Nature materials* 2007, 6 (3), 183-191.

57. First, P. N.; de Heer, W. A.; Seyller, T.; Berger, C.; Stroschio, J. A.; Moon, J.-S., Epitaxial graphenes on silicon carbide. *MRS bulletin* **2010**, *35* (04), 296-305.
58. Moreau, E.; Ferrer, F.; Vignaud, D.; Godey, S.; Wallart, X., Graphene growth by molecular beam epitaxy using a solid carbon source. *physica status solidi (a)* **2010**, *207* (2), 300-303.
59. Li, X.; Cai, W.; An, J.; Kim, S.; Nah, J.; Yang, D.; Piner, R.; Velamakanni, A.; Jung, I.; Tutuc, E., Large-area synthesis of high-quality and uniform graphene films on copper foils. *Science* **2009**, *324* (5932), 1312-1314.
60. Kim, K. S.; Zhao, Y.; Jang, H.; Lee, S. Y.; Kim, J. M.; Kim, K. S.; Ahn, J.-H.; Kim, P.; Choi, J.-Y.; Hong, B. H., Large-scale pattern growth of graphene films for stretchable transparent electrodes. *Nature* **2009**, *457* (7230), 706-710.
61. Yazyev, O. V.; Chen, Y. P., Polycrystalline graphene and other two-dimensional materials. *Nature nanotechnology* 2014.
62. Chu, J. H.; Kwak, J.; Kwon, T.-Y.; Park, S.-D.; Go, H.; Kim, S. Y.; Park, K.; Kang, S.; Kwon, S.-Y., Facile synthesis of few-layer graphene with a controllable thickness using rapid thermal annealing. *ACS applied materials & interfaces* 2012, *4* (3), 1777-1782.
63. Kwak, J.; Kwon, T.-Y.; Chu, J. H.; Choi, J.-K.; Lee, M.-S.; Kim, S. Y.; Shin, H.-J.; Park, K.; Park, J.-U.; Kwon, S.-Y., In situ observations of gas phase dynamics during graphene growth using solid-state carbon sources. *Physical Chemistry Chemical Physics* 2013, *15* (25), 10446-10452.
64. Marcano, D. C.; Kosynkin, D. V.; Berlin, J. M.; Sinitskii, A.; Sun, Z.; Slesarev, A.; Alemany, L. B.; Lu, W.; Tour, J. M., Improved synthesis of graphene oxide. *ACS nano* 2010, *4* (8), 4806-4814.
65. Shahriary, L.; Athawale, A. A., Graphene oxide synthesized by using modified hummers approach. *IJREEE* 2014, *2*, 58-63.
66. Kwak, J.; Chu, J. H.; Choi, J.-K.; Park, S.-D.; Go, H.; Kim, S. Y.; Park, K.; Kim, S.-D.; Kim, Y.-W.; Yoon, E.; Kodambaka, S.; Kwon, S.-Y., Near room-temperature synthesis of transfer-free graphene films. *Nat Commun* **2012**, *3*, 645.
67. Fisher, J. C., Calculation of Diffusion Penetration Curves for Surface and Grain Boundary Diffusion. *Journal of Applied Physics* 1951, *22* (1), 74-77.
68. Balluffi, R.; Bkakey, J., Special aspects of diffusion in thin films. *Thin Solid Films* **1975**, *25* (2), 363-392.
69. Harrison, L., Influence of dislocations on diffusion kinetics in solids with particular reference to the alkali halides. *Transactions of the Faraday Society* 1961, *57*, 1191-1199.
70. Kresse, G.; Furthmüller, J., Efficiency of ab-initio total energy calculations for metals and semiconductors using a plane-wave basis set. *Computational Materials Science* 1996, *6* (1),

- 15-50.
71. Kresse, G.; Furthmüller, J., Efficient iterative schemes for ab initio total-energy calculations using a plane-wave basis set. *Physical Review B* 1996, 54 (16), 11169.
 72. Tauc, J.; Grigorovici, R.; Vancu, A., Optical properties and electronic structure of amorphous germanium. *physica status solidi (b)* 1966, 15 (2), 627-637.
 73. Regan, W.; Alem, N.; Alemán, B.; Geng, B.; Girit, Ç.; Maserati, L.; Wang, F.; Crommie, M.; Zettl, A., A direct transfer of layer-area graphene. *Applied Physics Letters* **2010**, 96 (11), 113102.
 74. Eda, G.; Fanchini, G.; Chhowalla, M., Large-area ultrathin films of reduced graphene oxide as a transparent and flexible electronic material. *Nature nanotechnology* **2008**, 3 (5), 270-274.
 75. Wu, X.; Sprinkle, M.; Li, X.; Ming, F.; Berger, C.; de Heer, W. A., Epitaxial-graphene/graphene-oxide junction: an essential step towards epitaxial graphene electronics. *Physical review letters* **2008**, 101 (2), 026801.
 76. Robinson, J. T.; Perkins, F. K.; Snow, E. S.; Wei, Z.; Sheehan, P. E., Reduced graphene oxide molecular sensors. *Nano letters* **2008**, 8 (10), 3137-3140.
 77. Gao, W.; Singh, N.; Song, L.; Liu, Z.; Reddy, A. L. M.; Ci, L.; Vajtai, R.; Zhang, Q.; Wei, B.; Ajayan, P. M., Direct laser writing of micro-supercapacitors on hydrated graphite oxide films. *Nature nanotechnology* **2011**, 6 (8), 496-500.
 78. Loh, K. P.; Bao, Q.; Eda, G.; Chhowalla, M., Graphene oxide as a chemically tunable platform for optical applications. *Nature chemistry* **2010**, 2 (12), 1015-1024.
 79. Han, N.; Cuong, T. V.; Han, M.; Ryu, B. D.; Chandramohan, S.; Park, J. B.; Kang, J. H.; Park, Y.-J.; Ko, K. B.; Kim, H. Y., Improved heat dissipation in gallium nitride light-emitting diodes with embedded graphene oxide pattern. *Nature communications* **2013**, 4, 1452.
 80. Kim, S.; Zhou, S.; Hu, Y.; Acik, M.; Chabal, Y. J.; Berger, C.; de Heer, W.; Bongiorno, A.; Riedo, E., Room-temperature metastability of multilayer graphene oxide films. *Nature materials* **2012**, 11 (6), 544-549.
 81. Gao, W.; Alemany, L. B.; Ci, L.; Ajayan, P. M., New insights into the structure and reduction of graphite oxide. *Nature chemistry* **2009**, 1 (5), 403-408.
 82. Mkhoyan, K. A.; Contryman, A. W.; Silcox, J.; Stewart, D. A.; Eda, G.; Mattevi, C.; Miller, S.; Chhowalla, M., Atomic and electronic structure of graphene-oxide. *Nano letters* **2009**, 9 (3), 1058-1063.
 83. Bagri, A.; Mattevi, C.; Acik, M.; Chabal, Y. J.; Chhowalla, M.; Shenoy, V. B., Structural evolution during the reduction of chemically derived graphene oxide. *Nature chemistry*

- 2010**, 2 (7), 581-587.
84. Marcano, D. C.; Kosynkin, D. V.; Berlin, J. M.; Sinitskii, A.; Sun, Z.; Slesarev, A.; Alemany, L. B.; Lu, W.; Tour, J. M., Improved synthesis of graphene oxide. *ACS nano* **2010**, 4 (8), 4806-4814.
 85. Stankovich, S.; Dikin, D. A.; Dommett, G. H.; Kohlhaas, K. M.; Zimney, E. J.; Stach, E. A.; Piner, R. D.; Nguyen, S. T.; Ruoff, R. S., Graphene-based composite materials. *Nature* **2006**, 442 (7100), 282-286.
 86. Mattevi, C.; Eda, G.; Agnoli, S.; Miller, S.; Mkhoyan, K. A.; Celik, O.; Mastrogiovanni, D.; Granozzi, G.; Garfunkel, E.; Chhowalla, M., Evolution of electrical, chemical, and structural properties of transparent and conducting chemically derived graphene thin films. *Advanced Functional Materials* **2009**, 19 (16), 2577.
 87. Chu, J. H.; Kwak, J.; Kim, S.-D.; Lee, M. J.; Kim, J. J.; Park, S.-D.; Choi, J.-K.; Ryu, G. H.; Park, K.; Kim, S. Y., Monolithic graphene oxide sheets with controllable composition. *Nature communications* **2014**, 5.
 88. Chen, S.; Brown, L.; Levendorf, M.; Cai, W.; Ju, S.-Y.; Edgeworth, J.; Li, X.; Magnuson, C. W.; Velamakanni, A.; Piner, R. D., Oxidation resistance of graphene-coated Cu and Cu/Ni alloy. *ACS nano* **2011**, 5 (2), 1321-1327.
 89. Li, X.; Cai, W.; An, J.; Kim, S.; Nah, J.; Yang, D.; Piner, R.; Velamakanni, A.; Jung, I.; Tutuc, E., Large-area synthesis of high-quality and uniform graphene films on copper foils. *Science* **2009**, 324 (5932), 1312-1314.
 90. eina, A.; Jia, X.; Ho, J.; Nezich, D.; Son, H.; Bulovic, V.; Dresselhaus, M. S.; Kong, J., Large area, few-layer graphene films on arbitrary substrates by chemical vapor deposition. *Nano letters* **2008**, 9 (1), 30-35.
 91. Sun, Z.; Yan, Z.; Yao, J.; Beitler, E.; Zhu, Y.; Tour, J. M., Growth of graphene from solid carbon sources. *Nature* **2010**, 468 (7323), 549-552.
 92. Yan, K.; Wu, D.; Peng, H.; Jin, L.; Fu, Q.; Bao, X.; Liu, Z., Modulation-doped growth of mosaic graphene with single-crystalline p-n junctions for efficient photocurrent generation. *Nature communications* **2012**, 3, 1280.
 93. Chu, J. H.; Kwak, J.; Kwon, T.-Y.; Park, S.-D.; Go, H.; Kim, S. Y.; Park, K.; Kang, S.; Kwon, S.-Y., Facile synthesis of few-layer graphene with a controllable thickness using rapid thermal annealing. *ACS applied materials & interfaces* **2012**, 4 (3), 1777-1782.
 94. Yu, Q.; Jauregui, L. A.; Wu, W.; Colby, R.; Tian, J.; Su, Z.; Cao, H.; Liu, Z.; Pandey, D.; Wei, D., Control and characterization of individual grains and grain boundaries in graphene grown by chemical vapour deposition. *Nature materials* **2011**, 10 (6), 443-449.
 95. Yan, Z.; Liu, G.; Khan, J. M.; Balandin, A. A., Graphene quilts for thermal management of

- high-power GaN transistors. *Nature communications* **2012**, 3, 827.
96. Lv, R.; Li, Q.; Botello-Méndez, A. R.; Hayashi, T.; Wang, B.; Berkdemir, A.; Hao, Q.; Elías, A. L.; Cruz-Silva, R.; Gutiérrez, H. R., Nitrogen-doped graphene: beyond single substitution and enhanced molecular sensing. *Scientific reports* **2012**, 2.
 97. Choi, J.-K.; Huh, J.-H.; Kim, S.-D.; Moon, D.; Yoon, D.; Joo, K.; Kwak, J.; Chu, J. H.; Kim, S. Y.; Park, K., One-step graphene coating of heteroepitaxial GaN films. *Nanotechnology* **2012**, 23 (43), 435603.
 98. Nair, R.; Blake, P.; Grigorenko, A.; Novoselov, K.; Booth, T.; Stauber, T.; Peres, N.; Geim, A., Fine structure constant defines visual transparency of graphene. *Science* **2008**, 320 (5881), 1308-1308.
 99. Tauc, J.; Grigorovici, R.; Vancu, A., Optical properties and electronic structure of amorphous germanium. *physica status solidi (b)* **1966**, 15 (2), 627-637.
 100. Mkhoyan, K. A.; Contryman, A. W.; Silcox, J.; Stewart, D. A.; Eda, G.; Mattevi, C.; Miller, S.; Chhowalla, M., Atomic and electronic structure of graphene-oxide. *Nano letters* **2009**, 9 (3), 1058-1063.
 101. Erickson, K.; Erni, R.; Lee, Z.; Alem, N.; Gannett, W.; Zettl, A., Determination of the local chemical structure of graphene oxide and reduced graphene oxide. *Advanced Materials* **2010**, 22 (40), 4467-4472.
 102. Tuinstra, F.; Koenig, J. L., Raman spectrum of graphite. *The Journal of Chemical Physics* **1970**, 53 (3), 1126-1130.
 103. Kwon, S.-Y.; Ciobanu, C. V.; Petrova, V.; Shenoy, V. B.; Barenó, J.; Gambin, V.; Petrov, I.; Kodambaka, S., Growth of semiconducting graphene on palladium. *Nano letters* **2009**, 9 (12), 3985-3990.
 104. Kim, J. J.; Shin, S. H.; Jung, J. A.; Choi, K. J.; Kim, J. H., First-principles study of interstitial diffusion of oxygen in nickel chromium binary alloy. *Applied Physics Letters* **2012**, 100 (13), 131904.
 105. Kresse, G.; Joubert, D., From ultrasoft pseudopotentials to the projector augmented-wave method. *Physical Review B* **1999**, 59 (3), 1758.
 106. Perdew, J. P.; Burke, K.; Ernzerhof, M., Generalized gradient approximation made simple. *Physical review letters* **1996**, 77 (18), 3865.
 107. Monkhorst, H. J.; Pack, J. D., Special points for Brillouin-zone integrations. *Physical Review B* **1976**, 13 (12), 5188.
 108. Jäger, W.; Mayer, J., Energy-filtered transmission electron microscopy of Si_mGe_n superlattices and Si_mGe_n heterostructures I. Experimental results. *Ultramicroscopy* **1995**, 59 (1), 33-45.

109. Luo, Z.; Lu, Y.; Singer, D. W.; Berck, M. E.; Somers, L. A.; Goldsmith, B. R.; Johnson, A. C., Effect of substrate roughness and feedstock concentration on growth of wafer-scale graphene at atmospheric pressure. *Chemistry of Materials* **2011**, *23* (6), 1441-1447.
110. Kim, S. Y.; Lee, I.-H.; Jun, S., Transition-pathway models of atomic diffusion on fcc metal surfaces. I. Flat surfaces. *Physical Review B* **2007**, *76* (24), 245407.
111. Ajayan, P. M.; Yakobson, B. I., Graphene: Pushing the boundaries. *Nature materials* **2011**, *10* (6), 415-417.
112. Boukhvalov, D. W.; Katsnelson, M. I., Modeling of graphite oxide. *Journal of the American Chemical Society* **2008**, *130* (32), 10697-10701.
113. Kobayashi, T.; Kimura, N.; Chi, J.; Hirata, S.; Hobara, D., Channel-Length-Dependent Field-Effect Mobility and Carrier Concentration of Reduced Graphene Oxide Thin-Film Transistors. *Small* **2010**, *6* (11), 1210-1215.
114. Eda, G.; Mattevi, C.; Yamaguchi, H.; Kim, H.; Chhowalla, M., Insulator to semimetal transition in graphene oxide. *The Journal of Physical Chemistry C* **2009**, *113* (35), 15768-15771.
115. Nardes, A.; Kemerink, M.; Janssen, R., Anisotropic hopping conduction in spin-coated PEDOT: PSS thin films. *Physical Review B* **2007**, *76* (8), 085208.
116. Joo, J.; Long, S.; Pouget, J.; Oh, E.; MacDiarmid, A.; Epstein, A., Charge transport of the mesoscopic metallic state in partially crystalline polyanilines. *Physical Review B* **1998**, *57* (16), 9567.
117. Mott, N. F.; Davis, E. A., *Electronic processes in non-crystalline materials*. Oxford University Press: 2012.
118. Pollak, M.; Riess, I., A percolation treatment of high-field hopping transport. *Journal of Physics C: Solid State Physics* **1976**, *9* (12), 2339.
119. Eda, G.; Mattevi, C.; Yamaguchi, H.; Kim, H.; Chhowalla, M., Insulator to semimetal transition in graphene oxide. *The Journal of Physical Chemistry C* **2009**, *113* (35), 15768-15771.

Curriculum Vitae

Jae Hwan Chu, Ph.D

School of Materials Science and Engineering
Ulsan National Institute of Science and Technology (UNIST)
Republic of Korea
Cell Phone: +1-323-772-7924; E-mail: chu3195@unist.ac.kr
www.researchgate.net/profile/Jae_Chu



Personal Data:

Date of Birth: February 24, 1985
Nationality: Republic of Korea
Marital Status: Not married
Gender: Male

Education:

- 2010.3. ~ 2016.2** Combined Master & Ph.D. degree
School of Materials Science Engineering, Ulsan National Institute of Science and
Technology (UNIST), Ulsan, Korea
Research advisor: Prof. Soon-Yong, Kwon
- 2003.3. ~ 2010.2.** B.S. degree
School of Advanced Materials Science Engineering, Chonbuk National
University, Chonju, Korea (Military service from 2005 to 2007)

Research Theme:

- (1) Near-room temperature synthesis of transfer-free graphene films by Diffusion Assisted Synthesis (DAS) method.
- (2) Physically synthesized monolithic graphene oxide sheet with tunable composition and band gap energies by DAS method.

- (3) Facile synthesis of graphene film by Rapid Thermal Annealing (RTA) method.
- (4) Fabrication of graphene-based electronics.
- (5) Highly conductive and environmentally stable organic transparent electrodes laminated with graphene for transparent optoelectronic devices (OLED).
- (6) Synthesis of Transition Metal Dichalcogenides (TMDs) & characterizations.

Research Experience:

2015.6 ~ present

Visiting scholar

Department of Physics at University of Washington, Seattle.
(Xiaodong Xu's group)

- Synthesis of high quality WSe₂ and MoSe₂ monolayers.
- Characterization of quality by optical spectroscopy techniques.

2010.2 ~ 2015.5

Member of support technical staff, UNIST Nano Fabrication

Ultra-High Vacuum Chemical Vapor Deposition (UHV-CVD) systems equipped with Low Energy Electron Diffraction (LEED).

Thin film deposition technique: UHV E-beam Evaporator, DC & RF Sputter.

Nanofabrication technique: Photolithography (MA-6, SUSS MicroTec, Germany), Metal RIE & Dielectric RIE (Lab Star, TTL, Korea), PR Asher (V15-G, KAMI, Germany), Deep Si Etcher (Tegal 200, Tegal, France), Surface Profiler (P-6, KLA_Tencor, USA).

Chemical Vapor Deposition (CVD) technique: LP-CVD (Low Pressure Chemical Vapor Deposition), Growth of graphene and TMDs materials.

Film characterization techniques: Raman spectroscopy (alpha300R, WITec), Atomic Force Microscope (Multimode V & D3100, Veeco, USA).

Electron Microscopy characterization techniques:

Field Emission Scanning Electron Microscope (Nano230& Quata200, FEI, USA), Cold FE-SEM (S-4800, Hitachi), Normal SEM (S-3400N, Hitachi).

Spectroscopic analysis techniques: UV-Vis-NIR(Cary 5000, Agilent, USA), FT-IR (670-IR, Agilent, USA), Spectrofluorometer (FP-8500, Jasco, Japan).

Thermal analysis techniques: Thermogravimetric Analyzer (Q500, TA Instruments, USA).

X-Ray analysis: High Resolution X-Ray Diffractometer (D8 Advance, Bruker, Germany), Normal XRD (D8 Advance, Bruker).

Electrical property measurement: Transmission line method (TLM), FET measurement, van der pauw measurement.

Fabrication of Polymer Lighting Emitting Diodes (PLED)

2009.3 ~ 2010.2. Project: Preparation of ceramic porous honeycomb
Undergraduate student internship program
School of Advanced Materials Science Engineering, Chonbuk National
University, Chonju, Korea

Teaching Assistant:

2010.3 – 2010.7 MATERIAL SCIENCE AND ENGINEERING: AN INTRODUCTION
(WILLIAM D. CALLISTER)
Ulsan National Institute of Science and Technology (UNIST)

2011.8 – 2011.12 MATERIALS SCIENCE OF THIN FILMS (MILTON OHRING)
Ulsan National Institute of Science and Technology (UNIST)

2014.8 – 2014.12 LIGHT – EMITTING DIODES (E. FRED SCHUBERT)
Ulsan National Institute of Science and Technology (UNIST)

Publications:

- (1) **J.H. Chu**, D.H. Lee, J. Jo, S.Y. Kim, J.-W. Yoo, S.-Y. Kwon, "*Highly Conductive and Environmentally Stable Organic Transparent Electrodes Laminated with Graphene*", (submitted in Nature Communications)
- (2) S. Kang, A. Mandal, J.-H. Park, D.-Y. Um, **J.H. Chu**, S.-Y. Kwon, C.-R. Lee, "*Effects of growth temperatures on the characteristics of n-GaN nanorods-graphene hybrid structures*", **Journal of Alloys and Compounds**, 644, 808-813 (2015).
- (3) S.-Y. Kim, J. Kwak, **J.H. Chu**, J.B. Kim, S.Y. Kim, K. Park, S.-Y. Kwon, "*Controllable Synthesis of Graphene-Encapsulated Low-Dimensional Nanocomposites*", **Advanced Materials Interfaces**, 2, 1500112 (2015).
- (4) J.C. Yu, D.B. Kim, G. Baek, B.R. Lee, E.D. Jung, S. Lee, **J.H. Chu**, D.-K. Lee, K.J. Choi, S. Cho, M.H. Song, "*High-Performance Planar Perovskite Optoelectronic Devices: A Morphological and Interfacial Control by Polar Solvent Treatment*", **Advanced Materials**, 27, 3492-3500 (2015).
- (5) S. Kang, A. Mandal, **J.H. Chu**, J.-H. Park, S.-Y. Kwon, C.-R. Lee, "*Ultraviolet photoconductive devices with an n-GaN nanorod-graphene hybrid structure synthesized by metal-organic chemical vapor deposition*", **Scientific reports**, 5, 10808 (2015).
- (6) S.H. **J.H. Chu**, S.-Y. Kwon, I. C. Bang, "*Pool boiling CHF of reduced graphene oxide graphene, and SiC-coated surfaces under highly wettable FC-72*", **International Journal of Heat and Mass Transfer** 82, 490 (2015).
- (7) **J.H. Chu***, J. Kwak*, S.-D. Kim, M. J. Lee, J. J. Kim, S.-D. Park, J.-K. Choi, G. H. Ryu, K. Park, S. Y. Kim, J. H. Kim, Z. Lee, Y.-W. Kim, S.-Y. Kwon, "*Monolithic graphene oxide sheets with controllable composition*", **Nature Communications** 5, 3383 (2014). (*authors contributed equally)
- (8) J.-H. Huh, S. H. Kim, **J.H. Chu**, S. Y. Kim, J. H. Kim, S.-Y. Kwon, "*Enhancement of seawater corrosion resistance in copper using acetone-derived graphene coating*", **Nanoscale**, 6, 4379-4386 (2014).

- (9) J. Kwak, T.-Y. Kwon, **J.H. Chu**, J.-K. Choi, M.-S. Lee, S. Y. Kim, H.-J. Shin, K. Park, J.-U. Park, S.-Y. Kwon, "*In situ observations of gas phase dynamics during graphene growth using solid-state carbon sources*", **Physical Chemistry Chemical Physics**, 15, 10446-10452 (2013).
- (10) J.-K. Choi, J.-H. Hur, S.-D. Kim, D. Moon, D. Yoon, K.S. Joo, J. Kwak, **J.H. Chu**, S.Y. Kim, K. Park, Y.-W. Kim, E. Yoon, H. Cheong, S.-Y. Kwon, "*One-step graphene coating of heteroepitaxial GaN films*", **Nanotechnology** 23, 435603 (2012)
-featured in **Semiconductor Today** News (http://www.semiconductor-today.com/news_items/2012/NOV/UNIST_011112.html).
- (11) **J.H. Chu**, J. Kwak, T.-Y. Kwon, S.-D. Park, H. Go, S.Y. Kim, K. Park, S. Kang, S.-Y. Kwon*, "*Facile synthesis of few layer graphene with a controllable thickness using rapid thermal annealing*", **ACS Applied Materials & Interfaces** 4, 1777-1782 (2012).
- (12) J. Kwak, **J.H. Chu**, J.-K. Choi, S.-D. Park, H. Go, S.Y. Kim, K. Park, S.-D. Kim, Y.-W. Kim, E. Yoon, S. Kodambaka, S.-Y. Kwon*, "*Near room-temperature synthesis of transfer-free graphene films*", **Nature Communications** 3, 645 (2012).
- featured in Nature 483, S32-S33 (2012), **Materials Research Society** News (<http://www.mrs.org/article.aspx?id=2147489646>) etc.

Patents:

- (1) S.-Y. Kwon, S.Y. Kim, K. Park, J. Kwak, **J.H. Chu**, J.-K. Choi, "Graphene sheet, transparent electrode, active layer including the same, display, electronic device, optoelectronic device, battery, solar cell and dye-sensitized solar cell including the electrode or active layer", Korean Patent application number: 10-2011-0073117.
- (2) S.-Y. Kwon, S.Y. Kim, K. Park, J. Kwak, **J.H. Chu**, J.-K. Choi, "Wrinkle-free graphene sheet, transparent electrode, active layer including the same, display, electronic device, optoelectronic device, battery, solar cell and dye-sensitized solar cell including the electrode or active layer", PCT/KR2011/005438.
- (3) S.-Y. Kwon, K. Park, J.-K. Choi, J. Kwak, **J.H. Chu**, "Graphene transparent electrode and method of manufacturing the same and optoelectronic device and electronic device

including the graphene transparent electrode”, Korean Patent application number: 10-2011-0081770.

- (4) S.-Y. Kwon, **J.H. Chu**, J. Kwak, S.Y. Kim, J.H. Kim, K. Park, Z. Lee, “Graphene oxide, and method for manufacturing the same”, Korean Patent application number: 10-2014-0102603.

Conference Proceeding:

International

- (1) “Synthesis of Monolithic Graphene Oxide Sheets with Controllable Composition”
J.H. Chu, J. Kwak, S.-D. Kim, M. J. Lee, J. J. Kim, S.-D. Park, J.-K. Choi, G. H. Ryu, K. Park, S. Y. Kim, J. H. Kim, Z. Lee, Y.-W. Kim, S.-Y. Kwon, *E-MRS 2014 FALL MEETING* (Warsaw University of Technology, Poland, September, 2014)
- (2) “Low-Temperature Synthesis of Graphene Nanoshells Empolying Crsyttallization Catalyst”
S.-Y. Kim, J. Kwak, **J.H. Chu**, S. Y. Kim and S.-Y. Kwon, *E-MRS 2014 FALL MEETING* (Warsaw University of Technology, Poland, September, 2014)
- (3) “Large-Area Synthesis of High-Quality and Controllable Thickness Graphene Film by Rapid Thermal Annealing ”
J.H. Chu, J. Kwak, T.-Y. Kwon, S.-D. Park, H. Go, S.Y. Kim, K. Park, S. Kang, and S.-Y. Kwon, *10th U.S-Korea Forum on Nanotechnology* (Northeastern University, Boston, MA, October, 2013)
- (4) “In-situ observations of gas Phase dynamics during graphene growth using solid-state carbon sources”
J. Kwak, T.-Y. Kwon, **J.H. Chu**, M.-S, Lee, S.Y. Kim, H.-J. Shin, K. Park, J.-U. Park, and S.-Y. Kwon, *2013 MRS Spring Meeting & Exhibit* (San Francisco, California, April, 2013)
- (5) “One-step graphene coating of heteroepitaxial GaN films”
J.-K. Choi, J.-H. Hur, S.-D. Kim, D. Moon, D. Yoon, K.S. Joo, J. Kwak, **J.H. Chu**, S.Y. Kim, K. Park, Y.-W. Kim, E. Yoon, H. Cheong, and S.-Y. Kwon, *7th Singapore International Chemistry Conference* (National University of Singapore, Singapore, December, 2012)

(6) “Near room-temperature synthesis of transfer-free graphene films”

J. Kwak, **J.H. Chu**, J.-K. Choi, S.-D. Park, H. Go, S.Y. Kim, K. Park, S.-D. Kim, Y.-W. Kim,
E. Yoon, S. Kodambaka, and S.-Y. Kwon, *1st International Conference on Emerging
Advanced Nanomaterials* (Brisbane, Australia, October, 2012)

References:

Name: Professor **Soon-Yong Kwon**
Institution: Materials Science and Engineering, UNIST
Telephone: +82-52-217-2312 (O)
E-mail: sykwon@unist.ac.kr

Name: Professor **Kibok Park**
Institution: Electrical and Computer Engineering, UNIST
Telephone: +82-52-217-2111 (O)
E-mail: kibogpark@unist.ac.kr

Name: Professor **Sung Youb Kim**
Institution: Mechanical and Nuclear Engineering, UNIST
Telephone: +82-52-217-2321 (O)
E-mail: sykim@unist.ac.kr